Robust high fidelity microwave near-field entangling quantum logic gate

Von der QUEST-Leibniz-Forschungsschule
der Gottfried Wilhelm Leibniz Universität Hannover

zur Erlangung des akademischen Grades

Doktor der Naturwissenschaften
- Dr. rer. nat. -

genehmigte Dissertation von

M.Sc. Giorgio Zarantonello

2020

Referent:	Prof. Dr. Christian Ospelkaus
Korreferent:	Prof. Dr. Piet Oliver Schmidt
Korreferent:	Prof. Nikolay Vitanov
Tag der Promotion:	16.06.2020

Abstract

Trapped ions, together with superconducting qubits, are one of the two leading hardware platforms for scalable quantum information processing. The development of quantum computers represents a major technological breakthrough comparable to the introduction of classical computing. The benefits of this technology are currently limited by the technical capability to perform high fidelity entangling operations on the qubits. When gate fidelities surpass the fault-tolerance threshold it becomes possible, through error correction, to increase the system size to an arbitrary number of qubits. In this cumulative thesis we address some of the issues in the scalability of the trapped-ion quantum computer based on microwave near-fields. In this approach, gate operations on one or multiple ions are driven by an oscillating magnetic field generated by a current flowing through a conductor.

In the first part of this work we discuss the design of traps toward the implementation of large scale systems. We introduce the basic design of a surface-electrode ion trap with embedded microwave conductors. The oscillating magnetic field required to perform the operations is generated by a single optimized conductor. We discuss the simulation and characterization of the magnetic field pattern, which is fixed by the microwave conductor design. In addition, we demonstrate the capability to simulate, fabricate and characterize a multilayer surface ion trap. Multilayer traps are a key aspect for scalability since they are necessary to achieve large system sizes, with many 'ion registers', where the registers are interconnected by physically transporting ions between them.

In the second part of this thesis we demonstrate the implementation of a two-qubit entangling gate and we explore the possibilities offered by quantum control methods to improve its fidelity. We perform an entangling gate on two $^9Be^+$ ions and measure a Bell state fidelity of 98.2(1.2)%. Error characterization shows that the gate result is limited by technical issues connected to the ions' motional states. To reduce these errors we apply amplitude modulation of the gate microwave drive. After stabilization of the ions' radial modes, we obtain an amplitude modulated gate with infidelity in the 10^{-3} range. The result is confirmed by analyzing the data using three different methods.

Using additional dynamic decoupling techniques, these results could bring microwave near-field gates past the fault-tolerance threshold.

Keywords: trapped ions, quantum computing, quantum information processing, hyperfine qubits, microwaves near-field, two-qubit gates, quantum control, amplitude modulation.

Contents

Chapter 1

Introduction

1.1 Quantum computing system requirements

The most well-known application which attracted attention on digital quantum computing [Deu85] is the algorithm for the factorization of large numbers into primes [Sho94]. Given enough resources the quantum algorithm would be able to achieve its goal for numbers so large any classical computer would fail. The most obvious application for this specific algorithm would be to factorize quickly the large numbers which are at the basis of the public RSA cryptography protocol. Other relevant applications of digital quantum computers are the search of large databases [Gro97] or simulating quantum systems too complex for a classical computer [Fey82].

The basic criteria to perform digital quantum computing have been listed by DiVincenzo [DiV00]. They consist of 5 points:

- A scalable physical system with well characterized qubits.
- The ability to initialize the state of the qubits to a simple fiducial state.
- Long relevant decoherence times, much longer than the gate operation time.
- A 'universal' set of quantum gates.
- A qubit-specific measurement capability.

Given these conditions multiple hardware platforms have been identified as capable of implementing quantum computing: superconducting qubits [DWM04, CW08, CGC+12], nitrogen-vacancy centers in diamond [Ser10, MB11], optical lattices [BCJD99, BPR+05], Rydberg atoms [SWM10, WS12], quantum dots [LD98], photonic-based [Bar15] and trapped ions [CZ95, Ste97, WMI+98b, BXN+17]. Each one has different advantages or disadvantages compared to the others. The two platforms, which currently show the highest degree of development and success, are superconducting qubits [AAB+19] and trapped ions [PDF+20]. The work presented in this thesis will focus on the tools required for large scale quantum computing with multiple qubits in a trapped ion system.

1.2 Quantum computing with trapped ions

Trapped atomic ions have characteristics which satisfy the DiVincenzo criteria. Each qubit, given by two electronic states, is perfectly reproducible because different ions of the same atomic species will always have the same behavior under the same experimental conditions. Trapped ion systems can be prepared in arbitrary states by optical pumping and additional coherent population transfer to reach target states that are not possible to prepare only with laser pumping. Trapped ions can exhibit long coherence times [LOJ+05, HAB+14], tens of seconds or more, that makes them ideal candidates for quantum computing since gate operation times are in the μs range allowing therefore ample time for the realization of the quantum algorithm. Specific times depend on the gate and the implemented operation and can vary based on the approach. To measure whether the ion is in a specific qubit state can be done with state-dependent fluorescence with high fidelity [MSW+08, BSWL10].

The requirement of a 'universal' set of quantum gates can be summarized by the ability to perform any single qubit operation and a two-qubit entangling gate [DiV95]. These operations cannot be performed experimentally with arbitrary precision. By assuming certain amounts of noise and error in the operations and by propagating it in systems of interesting sizes, it has been deduced that the threshold for fault-tolerant quantum computation is an error rate of about 10^{-4} [Pre98, Kni10]. The threshold requires error correcting codes [Ste96, Kni05] which make use of 'ancilla' qubits to perform correctly the operations and implement an effective 'logic' qubit [BXN+17]. Currently the

fidelity that can be reached with these operations is 10^{-6} for single qubit operations [HAB+14] and better than 10^{-3} for two-qubit entangling gates [GTL+16].

1.2.1 Scalability

For quantum computing purposes most implementations employ Paul traps [Pau90]. These traps make use of a combination of static and dynamic electric fields to generate a 3D confining potential where the ions are trapped. Another approach is to use a Penning trap which is based on a combination of static electric and magnetic fields [Pen36, JAGH19]; this approach will not be discussed in this work. To be able to implement quantum algorithms of a computationally relevant size more qubits will be needed than available in current systems. This means that, despite interesting research for few qubits [Pre18], there is a compelling need to expand the size of the systems currently available.

Many methods have been suggested to implement large scale quantum computing with trapped ions. The first one is the so-called quantum charged coupled device (QCCD) architecture [WMI+98a, KMW02], represented in Fig. 1.1. Based on interconnected registers and accumulators, the architecture is characterized by a large scale trapping array with multiple trapping zones connected by junctions [AUW+10] that allows to reorder the ions at will. Each zone, repeated multiple times along the trap array, would be highly specialized for purposes such as ion loading, memory register, state detection, single- and multi-qubit operation. A second method allows the scaling to sizes larger than the single trap, it is based on multiple modules and envisions multiple QCCD modules designed in an independent way. The modules are then interconnected between each other by physical ion transport to provide large scale connectivity. The mean of connectivity between different modules can vary between approaches, such as transport by matching of confining potentials [LWF+17] or by physical ejection and injection of the ions between different modules [KLS+20]. A third scaling method is the multi-node architecture [CZKM97, ICL+17, SNN+20] based on interconnection of traps through photons. In this configuration there are different ion traps, which by themselves could already be full QCCD arrays, which form spatially separated nodes connected to each other by photonic entanglement. The light emitted by the ions in these traps is collected and transmitted to another trap or to a photonic

entangler setup using optics or optical fibers. This approach allows to transfer information between the separated nodes without any need to physically transfer the ions, potentially enabling large spatial separations.

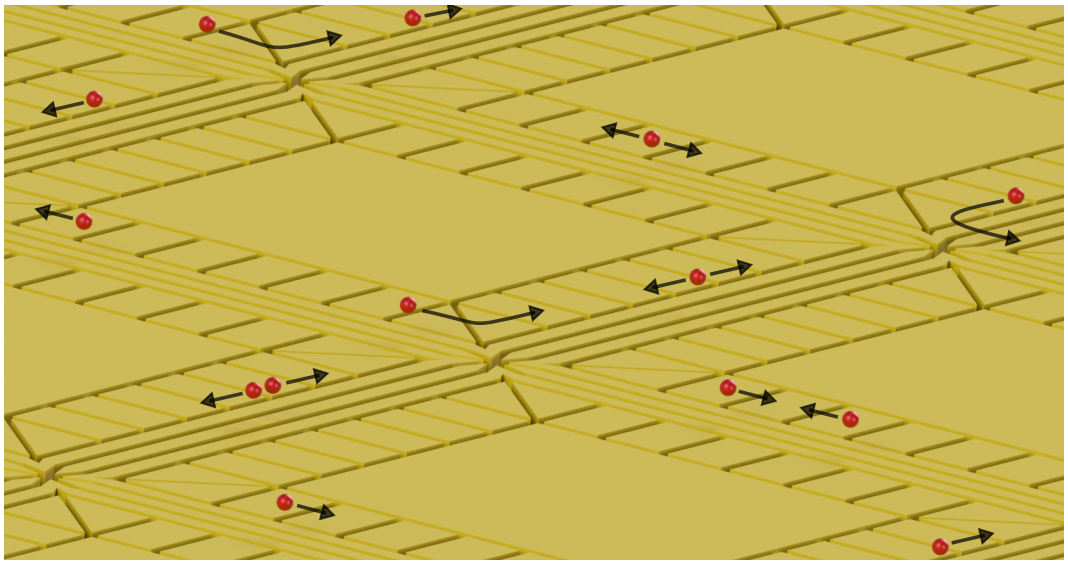

Figure 1.1: Artist impression of a QCCD architecture, figure from [Ung20]. The figure depicts multiple linear trapping arrays with junctions that allow the ions to move in two dimensions.

1.3 Outline

The cumulative thesis presented here discuss the steps which have been taken toward the implementation of a QCCD architecture in a surface-electrode ion trap with integrated microwave conductors for high fidelity quantum operations. The discussion is based on the peer-reviewed articles [WHZ+17, BSZH+19, HZBS+19, HZS+19, ZHM+19]. Details of the publications, including author contributions, and the published manuscripts are included at the end of each chapter. In Chapter 2 we discuss the basic surface-electrode trap design, the finite element simulations and the magnetic field model developed for microwave near-field operation using a specialized conductor. Chapter 3 presents the fabrication method for single and multi-layer traps, an analysis of the latter performance and the rationale of the importance of such structures for purposes of scalability. Chapter 4 addresses the theory for microwave operations and the results for experimental implementation of the Mølmer-Sørensen

entangling gate. In Chapter 5 we discuss various methods for quantum control and in more detail the amplitude modulation of the entangling gate drive as a means of reducing the main sources of errors previously discovered, all connected to the ion motion. The last, Chapter 6 contains conclusions and outlook on future research.

Chapter 2

Trap Design

The basic building block of the ion trap quantum computer is the trap itself. In this chapter, we provide a brief introduction to the design, simulation and testing of surface-electrode ion traps with embedded microwave conductors. When an alternating current is applied, the conductors generate a specific field pattern. In the case considered in this thesis, the oscillating magnetic field is effectively a quadrupole engineered to have a high gradient, B', and low amplitude, B. These features are required by the microwave near-field approach [OLA+08] to generate the spin-motional coupling necessary for the implementation of two-qubit entangling gates. The work discussed here has been published in the peer-reviewed article **P1** [WHZ+17] reported in Sec. 2.5 at the end of this chapter. Additional information to the one in this chapter can be found in [Wah16].

2.1 Trapping electrode design

The platform of choice in this thesis is the surface-electrode ion trap [CBB+05]. It differs from the common 'blade' trap in that all electrodes are arranged in a plane and that it can be fabricated with high precision on a planar substrate [SCR+06]. Surface-electrode ion traps present typically smaller ion-electrode distances d compared to other traps. In the specific case of the microwave near-field approach, this feature is an advantage because the ion is then located closer to the embedded microwave conductors. Let d be the dis-

tance of the ion from a current-carrying conductor embedded in the structure. Since the magnetic field increases with d^{-1} and the associated gradient with d^{-2}, the speed of the resulting near-field gates increases with shrinking trap dimensions.

In all linear Paul traps, two kinds of electrodes are necessary to provide the confinement: static (DC) electrodes and Radio Frequency (RF) electrodes [WMI+98b]. In a surface-electrode trap it is possible to calculate the electric field, and consequently the potential, generated by an electrode using different approaches. The one used for this work is the gapless plane approximation [OM01, Wes08]. This approach relies on using a Biot-Savart-like law to calculate the field generated by a finite-sized electrode where the gaps, the distance which separates different electrodes, are close to zero. Other methods can include corrections for finite gaps as well as fully numerical calculations, but have not been used in this work [SWL09, Sch10]. Figure 2.1 shows a schematic of the single-layer trap used in the peer-reviewed publication **P1**, where the electrodes are highlighted using different colors.

Axial confinement

The DC electrodes, when the voltage applied to each of them is appropriately engineered, provide harmonic confinement along the axial (y) direction. The minimum number of DC electrodes to produce a harmonic potential in the axial direction is four. This correspond to the number of degree of freedoms required to give the correct boundary conditions to the axial potential. The presence of more DC electrodes allows confining potentials modifications such as: ion transport [RBKD+02], multiple potential wells [BOC+11, HLB+11, WCB+14], ion crystals splitting or joining [HS06], ion swapping [KRS+16] and motional mode rotation [WOC+13].

Radial confinement

The RF electrode, when a radio frequency oscillating voltage is applied, generates an oscillating electric field quadrupole that can be approximated as a 2D harmonic potential in the so-called pseudopotential approximation and provides confinement in the radial (z-x) plane. The trapped ion is located at the minimum of the pseudopotential and is subject to the harmonic or secular motion and to a secondary kind of motion at the RF frequency called micromo-

tion [BMB+98]. The micromotion is due to the electric field oscillation which constantly accelerates and decelerates the ion. The micromotion amplitude is minimized when the force is minimized, i.e at the center of the RF quadrupole.

To change the dimensions of the system, from a 1D trapping array to 2D, as required by the QCCD architecture, the shape of the RF electrode needs to include junctions [HOS+06, BOV+09, AUW+10, WAF+13]. These are specially designed shapes of the RF electrode which allow crossings between different linear trapping arrays. An example of a junction is shown in Fig. 1.1. For symmetric rails of RF electrodes, many optimized designs are already available in the literature [MSW17]. All the works considered in this thesis make use of single-site linear Paul traps without any junction. The development and test of multilayer traps, detailed in Chapter 3, pave the way for implementing multi-site traps with junctions in the near future.

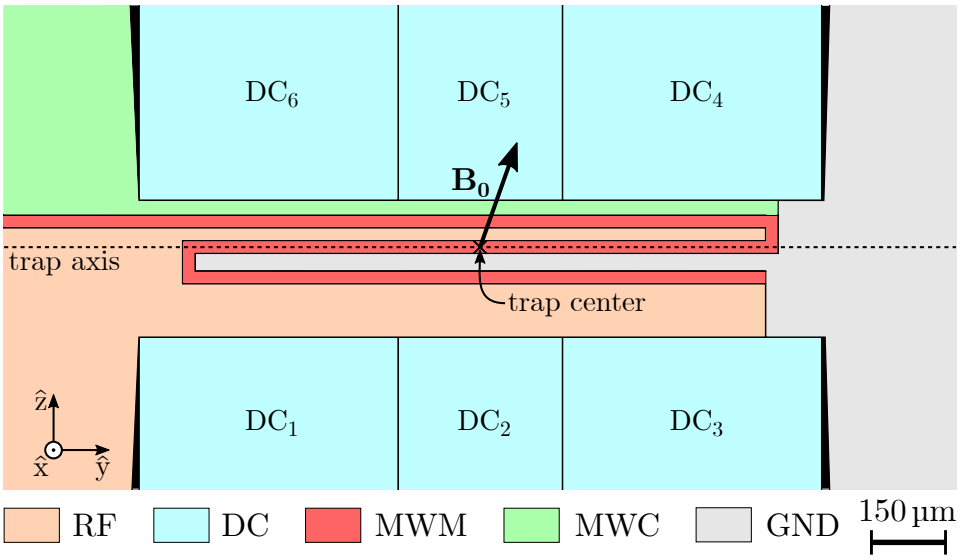

Figure 2.1: Schematic of the single-layer trap named 'SpyderTrap'. Electrodes are highlighted with different colors on the basis of their different functionality.

2.2 Microwave conductor design

To obtain the spin-motional coupling required for two-qubit entangling gates, it is necessary to produce a state-dependent force to displace the ion. This is generated by a field with an amplitude gradient. For laser-driven operations, the gradient is given by the spatial oscillation of the electric field at its optical wavelength, hundreds of nm. In the case of microwave-driven opera-

tions the natural oscillation of the magnetic field, due to its low frequency, provides wavelengths from a few centimeters to tens of centimeters. Such long wavelengths makes impossible to rely on the spatial oscillation of the field to produce high gradients. This is reflected in a simple picture where there is a single wire through which a microwave current is flowing. This conductor produces a gradient, B', which decays as d^{-2} where d is the distance of the ion from a conductor. Therefore strong *amplitude* gradients can be achieved in close proximity to the wire itself. However, the presence of a non-negligible magnetic field amplitude, B, that decays as d^{-1}, presents a problem. The residual field amplitude induces undesired effects such as AC Zeeman shifts and off-resonant carrier transitions. These effects can induce errors in the implementation of operations that require spin-motional coupling. These issues are discussed in Chapter 4 for both the resonant and off-resonant case. On the other hand, the field amplitude itself can be used to implement coherent population transfers for single-qubit gates. These operations are experimentally implemented by applying a microwave current at the qubit transition frequency on the conductor labeled MWC, MicroWave Carrier, see Fig. 2.1.

To produce a gradient without residual field amplitude, we rely on cancellation of fields generated by multiple conductors. One possibility is to use three separate conductors with a current oscillating at the desired frequency with specific relative amplitudes and phases, such as the trap used in [OWC+11, AHB+13]. One issue of such a design is that the three wires are independent, causing problems of phase and current amplitude stability which then affect the overall stability of the oscillating field gradient. This can be overcome with the use of a single conductor as reported in [CKDO14] or by other conductor geometries as proposed in [Mat16, Tar18]. By using a single conductor laid out in multiple segments, the current amplitude is fixed in all sections; meanwhile, the phase in each segment will be fixed by its length and the current flow direction. The approach used in this work is the one described in [CKDO14], where the single conductor is laid out in three segments connected in a meander shape, as shown in Fig. 2.1 where it is labeled MWM, MicroWave Meander. This choice of conductor generates a field which is an oscillating magnetic quadrupole.

A fixed single conductor design has the restriction of not being able to tune the position of the field minimum by changing the relative phase or current

amplitude of the different conductors. Therefore, the position of the minimum magnetic field is determined by the conductor geometry. Since in the radial plane the ion is located at the minimum of the pseudopotential generated by the RF electrode, it is necessary to accurately engineer the oscillating magnetic field produced by the conductor to overlap the magnetic field minimum with the pseudopotential minimum.

2.3 Microwave finite elements simulations

When applying microwave currents, phenomena such as the skin or proximity effect, which are not present for DC currents, need to be considered. The current flowing through the conductor induces eddy currents in nearby electrodes, generating a second oscillating magnetic field which is added to the original one, modifying its properties. In addition effects of capacitive and resistive coupling can lead to further currents. These effects are described in more detail in Sec. 3.3 where their influence on the magnetic field quadrupole is investigated. To accurately predict the field pattern generated by the single microwave conductor, we need to perform simulations that consider all these effects. The simulations were carried out with the commercial software Ansys HFSS[1] that performs finite element (FEM) simulations of the complete trap; all above-mentioned effects are accounted for by the software. The HFSS model includes: the trap structure, the neighboring filter board, wirebonds, the materials and input ports for the relevant signals. The filter board is a PCB made of Rogers 4350B. It supports feedlines which transport the DC, RF and microwave signals from the outside to the trap. Figure 2.2 shows a picture of the trap model. Wirebonds are used to connect the trap electrodes to the feedlines on the filter board. The complex magnetic and electric fields are then calculated inside small volumes and surface elements defined by a mesh. The dimensions of each mesh element must be chosen by carefully defined constraints in order to reach the required level of resolution in the result. For more information on the simulation conditions see [CKDO14, Wah16]. This procedure allows to extract the complex magnetic field in the region of interest, where the field from the three connected segments produces the desired oscillating quadrupole. In the same region, the complex electric field of the RF quadrupole is calculated to obtain a second estimation of the pseudopotential minimum that is compared with the gapless plane calculation; the results agree

[1]The version changed over the years and has been kept up-to-date with the latest release.

within uncertainty. A typical result of a simulated magnetic field can be seen in Fig. 1 b) of publication **P1**.

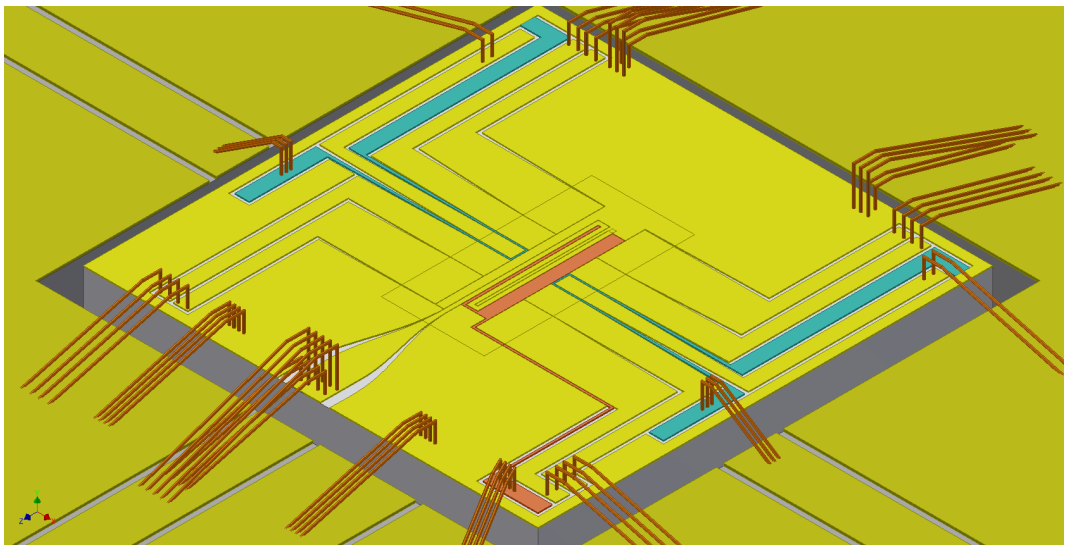

Figure 2.2: Example of FEM simulation model. It includes the trap chip, wirebonds and part of the filter board.

2.4 Microwave near-field model

The meander structure, electrode MWM shown in Fig. 2.1 and discussed in the previous section, generates an oscillating magnetic field quadrupole. Such a field pattern can be described by the simplified model reported in **P1**. The simplifications make the model depend on five parameters, excluding the position at which it is centered that provides two additional ones. As reported in [Wah16] the simplified model is:

$$\begin{aligned} \boldsymbol{B} &= \mathfrak{Re}\Big\{ e^{i\omega t}\Big[B\left(\mathbf{e}_\alpha \sin\psi - i\mathbf{e}_{\alpha-\pi/2}\cos\psi\right) + \\ &+ B'\left(\mathbf{Q}_\beta \cos\psi + i\mathbf{Q}_{\beta-\pi/2}\sin\psi\right)\mathbf{r}\Big]\Big\} \quad , \end{aligned} \tag{2.1}$$

where

$$\boldsymbol{r} = \begin{pmatrix} x \\ z \end{pmatrix}, \mathbf{e}_\alpha = \begin{pmatrix} \cos\alpha \\ \sin\alpha \end{pmatrix} \quad \text{and} \quad \mathbf{Q}_\beta = \begin{pmatrix} \cos\beta & \sin\beta \\ \sin\beta & -\cos\beta \end{pmatrix} \quad .$$

The angles α and β define the spatial orientation of the magnetic field amplitude and its gradient, respectively. The angle ψ characterizes the field polarization by controlling the relative amplitudes of the real and imaginary part. One would obviously like to verify that the field simulation obtained in HFSS matches the real field generated from the microfabricated trap. In order to determine the actual field the trapped ion can be used as a magnetic field sensor. An oscillating magnetic field induces energy shifts in the level of an atom through the AC Zeeman effect. This effect can be estimated using Eq. 3.22 from [Wah16] here reported:

$$\Delta E_i = \frac{1}{\hbar} \sum_j |\langle j| \boldsymbol{\mu} \cdot \boldsymbol{B} |i\rangle|^2 \left(\frac{1}{\omega - \omega_{ij}} + \frac{1}{\omega + \omega_{ij}} \right) \quad . \tag{2.2}$$

The equation gives the energy shift on level i for a magnetic field $\boldsymbol{B}$ oscillating at frequency ω. The shift depends on the interaction with other levels j and their frequency difference ω_{ij} from level i. The presence of the term $|\langle j| \boldsymbol{\mu} \cdot \boldsymbol{B} |i\rangle|^2$ can intuitively explain that the resulting shift depends on the transitions involved and the polarization of $\boldsymbol{B}$. To completely reconstruct the magnetic field quadrupole generated by the meander structure, it is necessary to probe two different transitions with different polarization dependence.

For our work with $^9Be^+$ the transitions chosen are $^2S_{1/2} |2, 1\rangle \leftrightarrow |1, 1\rangle$ and $^2S_{1/2} |2, 0\rangle \leftrightarrow |1, 0\rangle$ while probing with a magnetic field oscillating at about 1092 MHz. Here we used the $|F, m_F\rangle$ notation, where F is the ion's total angular momentum and m_F the projection on the quantization axis defined by an external magnetic field B_0. The experimental sequence is as described in [WOC+13]. The ion is moved in the radial (x-z) plane and the AC Zeeman shift is probed at different positions using a Ramsey experiment with spin echo where the magnetic field is active for different amounts of time always before the echo pulse. As a result, an oscillation of populations between the two states of the investigated transition is generated. The state detection is performed by resonance fluorescence [NSD86, SNBT86, BHIW86]. More details on the laser system and experimental conditions can be found in the appendix A.1. The resulting AC Zeeman shift is equal to $\hbar \cdot 2\pi/T$ where T is the period of the observed state oscillation. In this way it is possible to construct a two-dimensional AC Zeeman shift map for each transition, as shown in Fig. 3 of **P1**.

The two-dimensional maps are then fitted with the expected shifts from

Eq. 2.1 inserted into Eq. 2.2 to extract the magnetic field quadrupole parameters. In Table 2.1 the published measurement and a comparison with the simulation model are reported. The parameters B and B' are reported as a ratio since the actual absolute values depend on the amplitude of the current flowing in the conductor. These results prove the capability to accurately predict the magnetic field pattern necessary to produce spin-motion coupling in a trapped ion using the model developed in Ansys HFSS [Wah16].

	$B/B'\,[\mu\mathrm{m}]$	$\alpha\,[^\circ]$	$\beta\,[^\circ]$	$\psi\,[^\circ]$	$x_0\,[\mu\mathrm{m}]$	$z_0\,[\mu\mathrm{m}]$
Sim.	8.20(2)	25.15(2)	99.3(1)	6.5(1)	45.46(2)	−0.855(6)
Exp.	8.7(1.0)	31.1(3)	109.1(11.5)	4.3(1.2)	45.3(1)	−0.85(2)

Table 2.1: Parameters of the microwave near-fields according to Eq. 2.1, determined from simulations and from experimental measurements of the surface-electrode trap 'SpyderTrap' as reported in **P1**.

2.5 P1: Single-ion microwave near-field quantum sensor

Authors: M. Wahnschaffe, H. Hahn, **G. Zarantonello**, T. Dubielzig, S. Grondkowski , A. Bautista-Salvador, M. Kohnen, and C. Ospelkaus.

Journal: Applied Physics Letters

DOI: 10.1063/1.4974736

Author contribution: MW developed the microwave simulation model. MW, MK and CO developed the quadrupole model. HH and **GZ** performed the measurements reported. MW, HH, **GZ**, MK, ABS and CO analyzed the data. MW, MK, TD, SG and CO designed the experimental setup. CO devised the experiment plan. All authors participated in the realization of the manuscript.

Single-ion microwave near-field quantum sensor

M. Wahnschaffe,[1,2,3] H. Hahn,[1,2] G. Zarantonello,[1,2] T. Dubielzig,[2] S. Grondkowski,[2] A. Bautista-Salvador,[1,2,3] M. Kohnen,[1,2,3] and C. Ospelkaus[1,2,3]
[1]*Physikalisch-Technische Bundesanstalt, Bundesallee 100, 38116 Braunschweig, Germany*
[2]*Institute of Quantum Optics, Leibniz Universität Hannover, Welfengarten 1, 30167 Hannover, Germany*
[3]*Laboratory for Nano- and Quantum Engineering, Leibniz Universität Hannover, Schneiderberg 39, 30167 Hannover, Germany*

(Received 25 October 2016; accepted 10 January 2017; published online 20 January 2017)

We develop an intuitive model of 2D microwave near-fields in the unusual regime of centimeter waves localized to tens of microns. Close to an intensity minimum, a simple effective description emerges with five parameters that characterize the strength and spatial orientation of the zero and first order terms of the near-field, as well as the field polarization. Such a field configuration is realized in a microfabricated planar structure with an integrated microwave conductor operating near 1 GHz. We use a single $^9Be^+$ ion as a high-resolution quantum sensor to measure the field distribution through energy shifts in its hyperfine structure. We find agreement with simulations at the sub-micron and few-degree level. Our findings give a clear and general picture of the basic properties of oscillatory 2D near-fields with applications in quantum information processing, neutral atom trapping and manipulation, chip-scale atomic clocks, and integrated microwave circuits. *Published by AIP Publishing*. [http://dx.doi.org/10.1063/1.4974736]

Static or oscillatory electromagnetic fields have important applications in atomic and molecular physics for atom trapping and manipulation. Neutral atoms can be trapped in static magnetic fields in different types of magnetic traps.[1] Atomic ions can be trapped either in superpositions of static and oscillatory electric fields (Paul trap) or in superimposed static electromagnetic fields (Penning trap).[2] Atom and molecule decelerators rely on the distortion of atomic energy levels by spatially inhomogeneous fields.[3] Common to all of these field configurations is that their basic properties can be well described in terms of static solutions to the field equations and that the behavior of the field near its intensity minimum is often critical to the application. Prominent examples include Majorana losses in neutral atom magnetic traps[1] and micromotion in Paul traps.[4]

Recently, motivated by advances in microfabricated atom traps, interest has grown in microwave near-fields, which originate from microfabricated structures. Dimensions are typically small compared to the wavelength, but for the relatively high frequencies involved, eddy currents and phase effects become important, and the resulting field patterns are much richer than in the quasistatic case. Examples include rf potentials for neutral atoms[5] with applications in atom interferometry, quantum gates,[6,7] and chip-scale atomic clocks,[8] as well as microwave near-fields for trapped-ion quantum logic.[9–11] Also, neutral atomic clouds[12,13] and single ions[14] have been used to characterize near-fields at sub-mm length scales, to measure magnetic field gradients,[15] or for microwave magnetometry.[16] The behavior of these high-frequency oscillatory fields may also become relevant for coupling atomic and molecular quantum systems to microwave circuits in the quantum regime.[17,18] Of particular importance in this context are 2D field configurations, which can be realized, e.g., in integrated waveguides. Notwithstanding the strong experimental interest, there is a lack of intuitive understanding and the wide-spread notion that numerical simulation of microwave near-fields originating from such structures is difficult due to the many inductive and capacitive couplings between conductors.

Here, we develop a simple picture of 2D microwave fields around a local minimum of the field intensity and confirm this model through numerical simulations and experimental measurements involving a microfabricated ion trap with an integrated microwave conductor. We assume that the dimensions are small compared to the wavelength so that $\mathrm{div}\vec{B} = 0$ and $\mathrm{rot}\vec{B} = 0$ (near-field condition). Expansion of a 2D field up to first order would in principle result in a total of 6 complex or 12 real-valued expansion coefficients. However, taking into account the near-field condition, we can write the magnetic field in terms of eight parameters: $B_{r,i}$ and $\alpha_{r,i}$, characterizing the real and imaginary components of the complex field at the origin and their spatial orientations, and $B'_{r,i}$ and $\beta_{r,i}$, which describe the real and imaginary components of the complex field gradient and their spatial orientations

$$\vec{B} = \mathrm{Re}\left\{e^{i\omega t}\left[(B_r\vec{e}_{\alpha_r} + iB_i\vec{e}_{\alpha_i}) + (B'_rQ_{\beta_r} + iB'_iQ_{\beta_i})\vec{r} + \cdots\right]\right\},$$
$$\vec{e}_\alpha \equiv \begin{pmatrix}\cos\alpha\\ \sin\alpha\end{pmatrix} \quad \text{and} \quad Q_\beta \equiv \begin{pmatrix}\cos\beta & \sin\beta\\ \sin\beta & -\cos\beta\end{pmatrix}, \tag{1}$$

where Q_β is a traceless and symmetric "quadrupole matrix" to ensure the near-field condition. By multiplying Eq. (1) with a suitably chosen complex phase factor, it is possible to maximize the strength of the real part of the gradient. The same choice of the phase factor also leads to $\beta_i = \beta_r - \pi/2$. We now write $(B_r, B_i) = B(\cos\varphi, \sin\varphi)$ and $(B'_r, B'_i) \equiv B'(\cos\psi, \sin\psi)$. A suitable choice for the domain of the parameters is $B, B' \in \mathbb{R}$, $\alpha_r, \beta_r, \psi \in [0, \pi[$, $\alpha_i, \beta_i, \varphi \in [-\pi/2, \pi/2[$. Further imposing the condition that $|\vec{B}|$ has a minimum at the origin leads to $\alpha_i - \alpha_r + \pi/2 = n \cdot \pi$ with $n \in \mathbb{Z}$. For our choice of parameters, the left-hand side must be in

$]-\pi,\pi[$, and thus, $n=0$ and also $\alpha_i=\alpha_r-\pi/2$. Also from $|\vec{B}|$ minimal at the origin, we find $\varphi=\psi-\pi/2$. With $\alpha\equiv\alpha_r$ and $\beta\equiv\beta_r$, the field is finally given by

$$\vec{B}=\mathrm{Re}\Big\{e^{i\omega t}[B(\vec{e}_\alpha\sin\psi-i\vec{e}_{\alpha-\pi/2}\cos\psi)+B'(Q_\beta\cos\psi+iQ_{\beta-\pi/2}\sin\psi)\vec{r}+\cdots]\Big\}\qquad(2)$$

with just five free parameters — the strengths B and B' of the offset field and of the gradient, respectively, one angle α and β each for their spatial orientation, and an angle ψ characterizing the relative strength of the real and imaginary part of the gradient (and thus the polarization). The reduction from eight to five parameters compared to Eq. (1) is due to the assumption of a specific phase and of a minimum of $|\vec{B}|$ at the origin.

To give a specific example, consider the surface-electrode trap structure shown in Fig. 1(a), a design evolved from Ref. 19. It is located in a room temperature vacuum enclosure evacuated to $\approx 1\times10^{-11}$ mbar. The trap is composed of 11 μm thick electroplated gold electrodes (yellow, bright, and dark orange) with insulating 5 μm wide gaps (black lines) between the electrodes on top of an insulating AlN substrate (gray).[20] A single $^9Be^+$ ion is trapped above the surface by DC and RF electric fields. These are generated

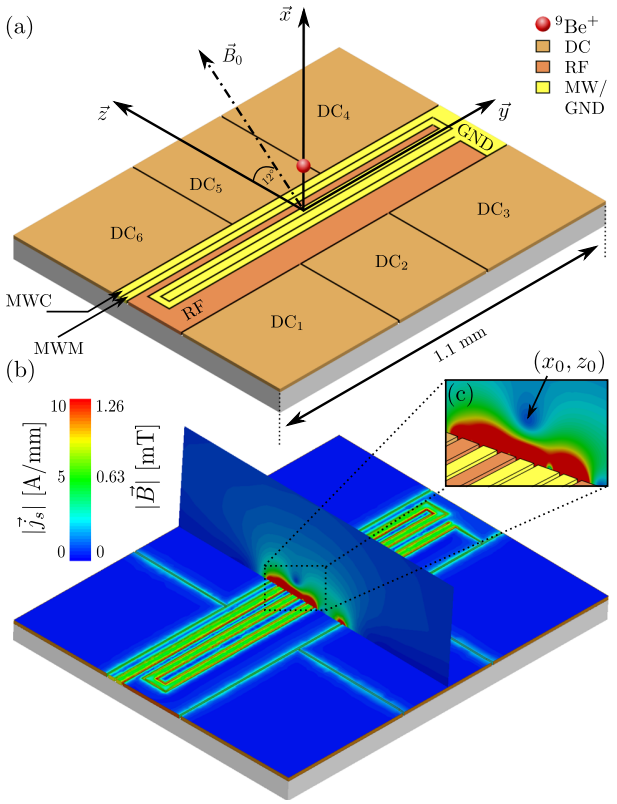

FIG. 1. (a) Surface-electrode ion trap structure. DC and RF voltages applied to the bright and dark orange electrodes create a harmonic trapping potential for a single ion at the position indicated by the red sphere. A microwave current coupled into the conductor MWM (yellow) leads to the surface-current distribution $|\vec{j}_s|$ depicted in (b). The resulting magnetic near-field $|\vec{B}|$ is shown in the xz plane (close-up in (c)). Around (x_0, z_0), the near-field is described by the model of Eq. (2) and characterized using a single ion as a microwave quantum sensor. For clarity, the height of the ion above the surface has been exaggerated in (a).

by applying a radio-frequency voltage ($2\pi\cdot 88$ MHz, 100 V_{pp}) to the electrode (RF), resulting in ponderomotive forces pushing the ion towards $(x_p, z_p)=(45.7, 2.9)$ μm. Additional DC voltages applied to electrodes DC$_{1-6}$ push the ion towards $y=0$ but may also create additional forces in the xz plane. The latter let us fine-tune the position of the ion, indicated by the red sphere, in the xz plane. The trap depth is 39 meV, and the trap frequencies are given by $\omega_y\simeq 2\pi\cdot 1$ MHz and $\omega_{x,z}\simeq 2\pi\cdot 11$ MHz.

In addition, microwave conductors, shown in yellow in Fig. 1(a), are integrated into the structure for the quantum state control of trapped ions. For this purpose, it is desirable to achieve a near-field pattern as described by Eq. (2) with B/B' as small as possible at a position where the ion can be trapped. These near-fields can then be used to implement multi-qubit quantum logic gates for quantum information processing with trapped ions.[9,10] Towards this end, we apply a microwave current at 1.093 GHz to the conductor MWM. Fig. 1(b) shows the corresponding simulated surface current distribution $|\vec{j}_s|$ in the electrode structure. A slice in the xz plane shows the resulting magnetic near-field $|\vec{B}|$ for $y=0$. Fig. 1(c) shows a close-up of the distribution of $|\vec{B}|$ around $(x_0, z_0)\approx(45.5, -0.9)$ μm, where it exhibits a local minimum. Here, we show that around (x_0, z_0), this near-field is accurately described by Eq. (2). We characterize the field distribution using a single ion as a quantum sensor and show agreement with numerical simulations of $\vec{B}$.

We simulate the structure, including the parts of the surrounding connector board, using Ansys HFSS. The simulations deliver $\vec{B}$ on a grid in the xz plane. The simulations show that B_y is much smaller than B_x and B_z, which validates the assumption of a 2D field configuration. We thus fit the model of Eq. (2) to the numerical B_x and B_z data on a 3 μm by 3 μm square to extract the parameters of Eq. (2). Here, in Eq. (2), we substitute $\vec{r}$ by $\vec{r}-(x_0, z_0)^T$, as the local field minimum is not located at the origin, and obtain the values of x_0 and z_0 as additional fit parameters. The resulting parameters are shown in Table I. Note that B and B' depend on the input current, and hence, only B/B' is given. Our simulations show a rather small value for ψ; as a result, the real part of the quadrupole is much stronger than the imaginary part. Hence, the polarization is mostly linear. The dominant contribution to the gradient B' stems from the three conductor segments forming the meander MWM, while the offset field B, which is $\pi/2$ out of phase with the gradient, results from inductive coupling to neighboring metal electrodes and from the associated eddy currents visible in Fig. 1(b), as well as

TABLE I. Parameters of the microwave near-fields according to Eq. (2), determined from simulations and from experimental measurements using a single $^9Be^+$ ion (Fig. 3).

Parameter (units)	Simulation	Experimental data
B/B' [μm]	8.20(2)	8.7(1.0)
ψ [°]	6.5(1)	4.3(1.2)
α [°]	25.15(2)	31.1(3)
β [°]	99.3(1)	109.1(11.5)
x_0 [μm]	45.46(2)	45.3(1)
z_0 [μm]	−0.855(6)	−0.8(2)

from phase delays along the meander.[19] The errors of the fit parameters are the standard errors from the nonlinear least squares fit and indicate how well the model of Eq. (2) describes the field distribution.

The magnetic near-field $\vec{B}$ primarily results in energy shifts of internal hyperfine states of the $^9Be^+$ ion and does not affect its position significantly. The main idea of the experiment is to measure these shifts spectroscopically for different positions of the ion controlled by the DC voltages. We can thus determine the parameters of Eq. (2) experimentally and compare them to the simulations. We load single ions into the trap by hitting a solid ^{9}Be target with single pulses of a nanosecond pulsed laser at 1064 nm and by subsequent resonant two-photon ionization at 235 nm[21,22] from the resulting ablation plume. Ions are laser cooled and detected using light resonant with the cycling transition $|S_{1/2}, F = 2, m_F = 2\rangle \rightarrow |P_{3/2}, m_J = +3/2, m_I = +3/2\rangle$ at 313 nm. We apply a static bias field $\vec{B}_0$ in the yz plane and at an angle of 12° with respect to the z axis to lift the degeneracy of the hyperfine levels. The hyperfine sublevels of the ground state are shown in Fig. 2 and labeled with $|F, m_F\rangle$. Here, F is the quantum number of the total angular momentum $\vec{F}$ and m_F the quantum number of its projection on $\vec{B}_0$. At the experimental value of $B_0 = 22.3$ mT, the state combination $|F = 2, m_F = 1\rangle$ and $|F = 1, m_F = 1\rangle$ forms a first order magnetic-field independent qubit,[23] which can be exploited for long coherence times. Laser cooling prepares the ion in $|F = 2, m_F = 2\rangle$. Through a series of microwave current pulses on the conductor MWC (cf. Fig. 1(a)), resonant with suitable hyperfine transitions, we can prepare an arbitrary target state within the $S_{1/2}$ hyperfine manifold of Fig. 2 and determine the population of any state by transferring it back to $|F = 2, m_F = 2\rangle$ and subsequently detecting fluorescence photons scattered on the cycling transition.

We determine the properties of the microwave near-field through AC Zeeman energy shifts which they induce on suitable atomic hyperfine states, analogous to AC Stark shifts for optical fields. The AC Zeeman shift of a hyperfine energy level E_i is given by

$$\delta E_{\mathrm{AC}} = \hbar \cdot \mathrm{sgn}(E_j - E_i) \sum_{j \neq i} \frac{|\Omega_{ij}(\vec{B})|^2}{\omega - \omega_{ij}}, \tag{3}$$

where the sum is over all other energy levels j, $\omega_{ij} = |E_i - E_j|/\hbar$, and $\Omega_{ij}(\vec{B})$ is the Rabi rate for the $i \leftrightarrow j$ transition that depends linearly on atomic matrix elements

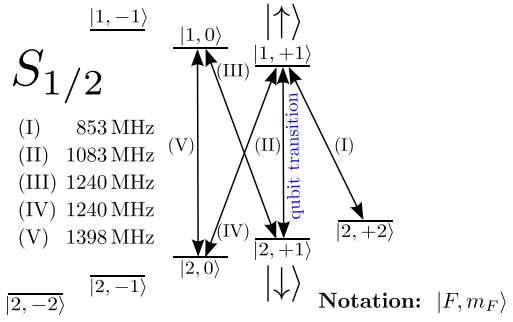

FIG. 2. Hyperfine structure of the $^9Be^+$ ground state at 22.3 mT, where transition (II) is a first-order magnetic-field independent qubit transition.

and the components of $\vec{B}$. For actual calculations, we also take into account the (small) Bloch-Siegert shift from the counter-rotating term. Plugging in $\vec{B}$ from Eq. (2), the AC Zeeman shift of a hyperfine energy level is a polynomial in $x - x_0$ and $z - z_0$ (up to second order in each), where the coefficients are built from atomic matrix elements, trigonometric functions of ψ, α, β, and B and B'. We perform a nonlinear least-squares fit of this expression to experimentally measured AC Zeeman shifts as a function of x and z to obtain $\psi, \alpha, \beta, B, B', x_0$, and z_0. Experimentally, we cannot measure absolute energies but only relative shifts of two energy levels by probing the transition frequency between them. The shift of the transition frequency, thus, has the same form as the AC Zeeman shift of an individual level, just more terms. We denote these as $\delta f_{\mathrm{AC},k}(x, z; B, B', \psi, \alpha, \beta, x_0, z_0)$, where k identifies a transition in Fig. 2, for example, $k = (\mathrm{II})$.

We simultaneously fit datasets for two different transitions within the structure shown in Fig. 2, (V) and (II), because they couple to the polarization components of the field differently and thus provide complementary information. The (II) data exhibit a strong sensitivity to α, β, ψ, whereas the (V) data are mainly sensitive to B', B, x_0, and z_0. We first test this procedure on numerical HFSS data from which we calculate the expected AC Zeeman shifts on a useful grid of ion positions (x, z). We simultaneously fit $\delta f_{\mathrm{AC,(II)}}$ and $\delta f_{\mathrm{AC,(V)}}$ to these simulated AC Zeeman shift data. We find perfect agreement between the field parameters obtained from the simulated AC Zeeman shift data and those extracted directly from the fit of Eq. (2) to the simulation data (Table I).

While in principle such shifts could be measured by Rabi spectroscopy, we employ the Ramsey method described in Ref. 14 because it lends itself to easy automation. It does, however, not directly reveal the sign of the Zeeman shifts. In the following, we will therefore always show positive signs of the net shifts. The first column of Fig. 3 shows AC Zeeman shifts of transitions (II) (top) and (V) (bottom) as a

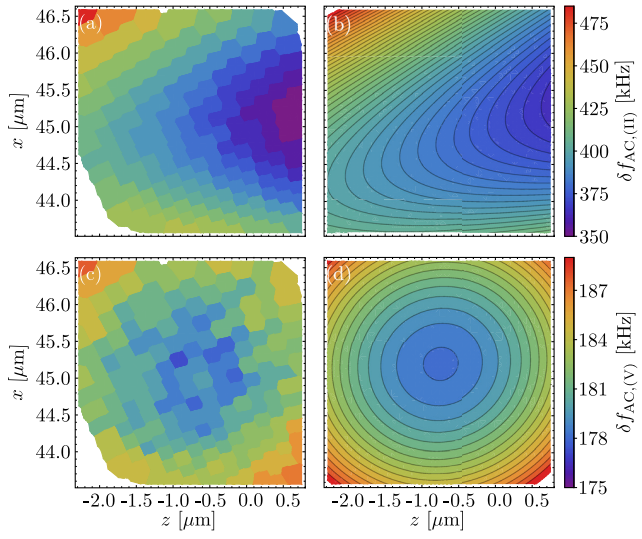

FIG. 3. AC Zeeman shifts $\delta f_{\mathrm{AC},k}$ induced by 2D near-fields on a single ion. The two rows show data for transitions (II) and (V) of Fig. 2, respectively. The first column shows AC Zeeman shifts measured using a single ion, and the second column shows the result of a fit of Eq. (2) to the experimental data. Empty (white) areas in the radial plane indicate where we cannot stably trap ions.

function of x and z, measured using a single ion. For transition (V), the AC Zeeman shift should exhibit a minimum close to the minimum of $|\vec{B}|$. As can be seen from Fig. 3(a), the data for transition (II) exhibit a more complex structure, which is a result of terms with different signs adding up in the total AC Zeeman shift calculation. We fit $\delta f_{\mathrm{AC},(\mathrm{II})}$ and $\delta f_{\mathrm{AC},(\mathrm{V})}$ to these data to obtain the fit parameters given in the third column of Table I. The calculated AC Zeeman shifts resulting from the fitted model are plotted in the right column of Fig. 3. Data for transition (V) were taken at a power level that was nominally 6 dB higher than that for (II) in order to reach higher frequency shifts. Thus, we also fitted the experimental power ratio between Figs. 3(c) and 3(a), yielding 6.47(15) dB. Experimental and fitted data have been scaled to the power level of Fig. 3(a). For reference, Figs. 3(a) and 3(b) correspond to $B' \approx 45\,\mathrm{T/m}$, while the data for Figs. 3(c) and 3(d) were taken for $B' \approx 94\,\mathrm{T/m}$ and were then scaled to match Figs. 3(a) and 3(b) as described above. As can be seen from Table I, the agreement between simulations and experiment is at the sub-micron and few-degree level. This is remarkable given the complicated interplay of primary and induced currents in this microfabricated structure where the properties of the field around the minimum essentially result from the subtraction of rather large contributions from individual conductors.[9,19]

An issue that may cause the fitted parameters to deviate slightly from the simulations is the accuracy of the assumed spatial position of the ion as a function of trap voltages applied. The position was extracted from electrostatic simulations and the pseudopotential approximation. Also, in our simulations, we found that spurious couplings to the electrode MWC had a rather strong influence on B/B' and on (x_0, z_0). There is a $\approx$10% coupling from the MWM to the MWC conductor. The value of B/B', therefore, depends on the assumed termination on the MWC input. For our simulations, we assumed that about 5% of the total power coupled from the MWM to the MWC conductor is reflected back into the structure. This is not an unreasonably high value, given a number of impedance changes that occur between the structure shown in Fig. 1 and the amplifier connected to MWC. Additional frequency shifts as a result of a potentially inhomogeneous bias field B_0 or spurious oscillatory magnetic fields associated with the RF trap drive might arise. However, these should be fully canceled by the spin-echo sequence employed in the spectroscopy.[14]

In summary, we have developed an intuitive model of 2D microwave quadrupole fields around a local minimum of $|\vec{B}|$, performed accurate numerical simulations of a 2D near-field structure, and confirmed their accuracy at the sub-micron and few-degree level using a single ion as a local field probe. The field model of Eq. (2) is essential as it allows us to compare simulations with experimental data. This description is applicable not only to microwave but also to lower frequency rf fields. Our results will inform the design of advanced structures for microwave quantum logic applications[9–11,24–26] of trapped ions. The model delivers a figure of merit, B/B', and parameters (α, β, ψ), directly relevant for this application. Ideally, future designs would be based on a multi-layer structure[27–29] so that signals could be delivered in separated layers underneath the structure via embedded waveguides and only brought to the surface close to the ion.[30] This would decouple the design of near-field structures from other trap "modules" on a scalable trap array[31] for quantum simulation[32,33] or quantum logic applications.[34,35] One can also interpret our measurements as a nanometer range resolution quantum enabled microwave magnetic field probe. The methodology developed here, combined with a "stylus" ion trap,[36] could be used to characterize microantennas and waveguides. Our findings may be applicable to integrated microwave circuits and hybrid quantum approaches coupling ions to other microwave or rf quantum devices.[17,18]

We are grateful for useful discussions with P. O. Schmidt, the NIST ion storage group, the Oxford ion trapping group, and J. Schöbel. We acknowledge the contributions by C. Vollmer in an early stage of the experiment, support by the PTB clean room facility team, packaging support by F. Schmidt-Kaler's group, and funding from QUEST, PTB, LUH, NTH (Project No. 2.2.11), and DFG through CRC 1227 DQ-*mat*.

[1]W. Ketterle, D. S. Durfee, and D. M. Stamper-Kurn, in *Proceedings of the 1998 Enrico Fermi Summer School on Bose-Einstein Condensation in Varenna, Italy* (IOS Press, Amsterdam, 1999), pp. 67–176.
[2]P. K. Ghosh, *Ion Traps*, International Series of Monographs on Physics (Clarendon Press, Oxford, 1996).
[3]S. Y. T. van de Meerakker, H. L. Bethlem, N. Vanhaecke, and G. Meijer, Chem. Rev. **112**, 4828 (2012).
[4]D. J. Berkeland, J. D. Miller, J. C. Bergquist, W. M. Itano, and D. J. Wineland, J. Appl. Phys. **83**, 5025 (1998).
[5]J. Fortágh and C. Zimmermann, Rev. Mod. Phys. **79**, 235 (2007).
[6]T. Calarco, E. A. Hinds, D. Jaksch, J. Schmiedmayer, J. I. Cirac, and P. Zoller, Phys. Rev. A **61**, 022304 (2000).
[7]P. Treutlein, T. W. Hänsch, J. Reichel, A. Negretti, M. A. Cirone, and T. Calarco, Phys. Rev. A **74**, 022312 (2006).
[8]W. Maineult, C. Deutsch, K. Gibble, J. Reichel, and P. Rosenbusch, Phys. Rev. Lett. **109**, 020407 (2012).
[9]C. Ospelkaus, C. E. Langer, J. M. Amini, K. R. Brown, D. Leibfried, and D. J. Wineland, Phys. Rev. Lett. **101**, 090502 (2008).
[10]C. Ospelkaus, U. Warring, Y. Colombe, K. R. Brown, J. M. Amini, D. Leibfried, and D. J. Wineland, Nature **476**, 181 (2011).
[11]D. T. C. Allcock, T. P. Harty, C. J. Ballance, B. C. Keitch, N. M. Linke, D. N. Stacey, and D. M. Lucas, Appl. Phys. Lett. **102**, 044103 (2013).
[12]P. Böhi, M. F. Riedel, T. W. Hänsch, and P. Treutlein, Appl. Phys. Lett. **97**, 051101 (2010).
[13]A. Horsley, G.-X. Du, and P. Treutlein, New J. Phys. **17**, 112002 (2015).
[14]U. Warring, C. Ospelkaus, Y. Colombe, K. R. Brown, J. M. Amini, M. Carsjens, D. Leibfried, and D. J. Wineland, Phys. Rev. A **87**, 013437 (2013).
[15]A. Walther, U. Poschinger, F. Ziesel, M. Hettrich, A. Wiens, J. Welzel, and F. Schmidt-Kaler, Phys. Rev. A **83**, 062329 (2011).
[16]I. Baumgart, J.-M. Cai, A. Retzker, M. Plenio, and C. Wunderlich, Phys. Rev. Lett. **116**, 240801 (2016).
[17]D. I. Schuster, L. S. Bishop, I. L. Chuang, D. DeMille, and R. J. Schoelkopf, Phys. Rev. A **83**, 012311 (2011).
[18]D. Kielpinski, D. Kafri, M. J. Woolley, G. J. Milburn, and J. M. Taylor, Phys. Rev. Lett. **108**, 130504 (2012).
[19]M. Carsjens, M. Kohnen, T. Dubielzig, and C. Ospelkaus, Appl. Phys. B **114**, 243 (2014).
[20]P. Treutlein, Ph.D. thesis, Ludwig-Maximilians-Universität Müchen (2008).
[21]H.-Y. Lo, J. Alonso, D. Kienzler, B. C. Keitch, L. E. D. Clercq, V. Negnevitsky, and J. P. Home, Appl. Phys. B **114**, 17 (2013).
[22]R. J. Hendricks, D. M. Grant, P. F. Herskind, A. Dantan, and M. Drewsen, Appl. Phys. B **88**, 507 (2007).
[23]C. Langer, R. Ozeri, J. D. Jost, J. Chiaverini, B. DeMarco, A. Ben-Kish, R. B. Blakestad, J. Britton, D. B. Hume, W. M. Itano *et al.*, Phys. Rev. Lett. **95**, 060502 (2005).
[24]F. Mintert and C. Wunderlich, Phys. Rev. Lett. **87**, 257904 (2001).

[25]A. Khromova, C. Piltz, B. Scharfenberger, T. F. Gloger, M. Johanning, A. F. Varón, and C. Wunderlich, Phys. Rev. Lett. **108**, 220502 (2012).
[26]K. Lake, S. Weidt, J. Randall, E. D. Standing, S. C. Webster, and W. K. Hensinger, Phys. Rev. A **91**, 012319 (2015).
[27]J. M. Amini, H. Uys, J. H. Wesenberg, S. Seidelin, J. Britton, J. J. Bollinger, D. Leibfried, C. Ospelkaus, A. P. VanDevender, and D. J. Wineland, New J. Phys. **12**, 033031 (2010).
[28]N. D. Guise, S. D. Fallek, K. E. Stevens, K. R. Brown, C. Volin, A. W. Harter, J. M. Amini, R. E. Higashi, S. T. Lu, H. M. Chanhvongsak *et al.*, J. Appl. Phys. **117**, 174901 (2015).
[29]D. L. Moehring, C. Highstrete, D. Stick, K. M. Fortier, R. Haltli, C. Tigges, and M. G. Blain, New J. Phys. **13**, 075018 (2011).
[30]D. P. L. A. Craik, N. M. Linke, T. P. Harty, C. J. Ballance, D. M. Lucas, A. M. Steane, and D. T. C. Allcock, Appl. Phys. B **114**, 3 (2014).
[31]M. Mielenz, H. Kalis, M. Wittemer, F. Hakelberg, R. Schmied, M. Blain, P. Maunz, D. Leibfried, U. Warring, and T. Schaetz, Nat. Commun. **7**, 11839 (2016).
[32]R. Blatt and C. F. Roos, Nat. Phys. **8**, 277 (2012).
[33]C. Schneider, D. Porras, and T. Schaetz, Rep. Prog. Phys. **75**, 024401 (2012).
[34]D. J. Wineland, Rev. Mod. Phys. **85**, 1103 (2013).
[35]C. Monroe and J. Kim, Science **339**, 1164 (2013).
[36]R. Maiwald, D. Leibfried, J. Britton, J. C. Bergquist, G. Leuchs, and D. J. Wineland, Nat. Phys. **5**, 551 (2009).

Chapter 3

Ion trap scalability

In the last chapter we have seen how to simulate the near-field pattern necessary for spin-motional coupling using FEM models. Following the simulation results a single-layer trap has been verified to match the simulated oscillating quadrupole. To implement the QCCD architecture for the trapped-ion quantum computer based on the microwave near-field approach it is necessary to be able to fabricate and operate multi level structures. This chapter discusses the trap fabrication process, simulation and characterization of an advanced multilayer surface-electrode ion trap with embedded microwave conductors. The ability to fabricate multi level structures is fundamental to the QCCD architecture as we will discuss in detail. This work has been published in the peer-reviewed article **P2** and **P3** [BSZH$^+$19, HZBS$^+$19] reported in Sec. 3.4 and 3.5 at the end of this chapter.

3.1 Fabrication

Surface-electrode ion traps can be fabricated using standard microfabrication techniques [HLBH11], for high precision and reproducibility. The use of multilayer surface-electrode traps has also been previously proposed and demonstrated. Ion traps fabricated using industry-level MEMS [CHLK15] or CMOS [SFH$^+$10] processes have been shown but such methods present a limit in the thickness of the metal layers. CMOS techniques are generally limited to about $3\,\mu$m thick aluminum films, furthermore there are issues with thin

gold film deposition due to contamination[2]. MEMS processes can indeed be used to build large structures but they are limited to silicon micromachining and it might be challenging to planarize structures with high aspect ratios. The patented fabrication process [BSOWM19] used in this work allows to fabricate any number of thick planarized metal layers with high aspect ratio. As described in the published article, aspect ratios up to 14 : 1 have been fabricated. This feature is of interest because of the importance of shielding the ion from patch potentials that can lead to trapping instabilities. These potentials are formed from charges deposited on the exposed dielectric in between the electrode gaps. As shown in Fig. 7 of [Sch10], high aspect ratios, larger than 1 : 1, are necessary to minimize the effects of such charges. In addition, thick metal electrodes are useful in case of argon cleaning of the ion trap [HCW+12], a procedure used to clean the trap surface from potential adsorbates or other contaminants in order to reduce the so-called 'anomalous motional heating' issue. This procedure may remove few tens of nanometers of gold. Hence, thin metal layers are at risk of being completely removed or damaged in a way that could destroy the trap functionality. The purpose for employing argon cleaning in the experiment is explained further in Sec. 4.7.

The fabrication method adopted in this work is explained in detail in publication **P2** which reports how to fabricate single and multilayer surface-electrode traps. Fig. 2 of **P2** shows a schematic of the fabrication process and layer definition. Here, only a summary of the fabrication recipe for multilayer traps is presented:

a. A Ti 10 nm-thin and a 50 nm-thin seed layer of Au are evaporated on the wafer substrate.

b. Negative photoresist is coated, patterned via UV lithography and then developed.

c. Au is electroplated for building the bottom layer L_1, photoresist is removed and the structures cleaned under plasma etching.

d. Steps b) and c) are repeated to fabricate a vertical interconnect layer V_1 on top of L_1.

[2]This issue is known as gold-aluminum intermetallic formation. Informally known as 'purple plague' or 'white plague' depending on the exact chemical nature of the alloy formed.

e. The Au/Ti seed layer is removed using dry etching, then a polymer (PI) is coated on top of the already built layers and planarized by chemical mechanical polishing (CMP).

f. An additional Au/Ti seed layer is evaporated on top of the PI.

g. Steps b) and c) are repeated to built a second metal layer L_2.

h. Exposed dielectric in between the electrodes in L_2 is removed completely by plasma etching down to the wafer substrate.

The last step of the process, the plasma etching, combined with optimized electroplating parameters, is of particular interest since it allows to obtain a surface rms roughness of about $8.3 \pm 0.5\,\text{nm}$, two orders of magnitude better compared with our previous results. By minimizing the surface roughness the scattered light from the detection laser, and therefore the measurement background, is reduced, for more information see Sec. 4.5. Surface roughness can also play an important role in reducing electric noise experienced by the ion [LLC16] at cryogenic temperatures, although this is still under investigation in our traps.

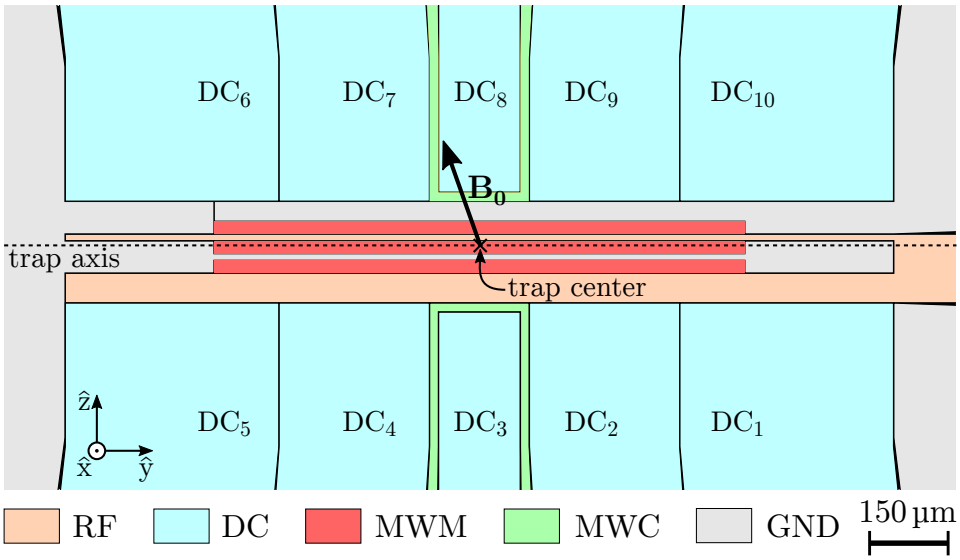

Figure 3.1: Schematic of the multilayer trap 'ML5G' top layer L_2. Electrodes are highlighted with different colors on the basis of their different functionality. Interconnects between the different segments of MWM are placed in the lower layers.

The ability to build multiple interconnected metal layers is fundamental to increase flexibility in the design of dedicated zones for readout, storing and

manipulation in the QCCD architecture [KMW02]. Moreover, the fabrication capability permits to bury signal feedlines and therefore to avoid routing problems, such as crossing lines, as would happen in a single-layer structure. The electrical contact of electrodes and feedlines located in different metal layers is done through the Vertical Interconnect Access (VIAs) that are present in layer V_1, this can be seen in Fig. 1 b) of **P3**. From a comparison between Fig. 2.1 and 3.1 the advantage of multiple layers can be pointed out. In the previous single-layer trap presented in Sec. 2.2, the MWM conductor is continuous on a single plane which forces to end the RF electrode abruptly. In an extended trap structure, this abrupt end of the RF electrode forbids transport of ions in that specific axial direction since no radial confinement is possible. In the multilayer design the turning points between the segments of the MWM conductor are buried in the lower layers. In this way the RF electrode is uninterrupted in the axial (y) direction providing the necessary confinement which permits to transport ions.

Given the introduction of thick insulating material, the PI, in the multilayer fabrication process, compared to the single metal layer case, it is of relevance to study heat conduction due to the high microwave current involved in the near-field approach. The polymide used[3] is a good electrical insulator but a poor thermal conductor. One solution is to extend the microwave conductors all the way down to the top of the substrate. The thermal behavior of the trap at critical points, such as the center of the three MWM segments, has been investigated to ensure the feasibility of desired operations, see appendix of **P3**. In the fabricated trap 'ML5G' the top and bottom metal layers are $h_3 = 5.2\,\mu$m and $h_1 = 4.4\,\mu$m thick, respectively. The three MWM segments have a length $l_m = 1\,$mm each and present a polymide filled pocket of length $l_{\mathrm{th}} = 200\,\mu$m and $h_2 = 9.4\,\mu$m of thickness. The reason for the pocket is that a MWM conductor continuous down to the substract was not found to be advantageous from a microwave near-field design perspective. The reason for the presence of this polymide filled pocket are further explained in Sec. 3.2 and in the published article. Ideally it is desirable to have an insulator with higher thermal conductivity. A good insulator choice would then be CVD diamond or PECVD (SiN). With respect to the thermal behavior, a different challenge with some interesting prospects could be the employment of metamaterials with high thermal conductivity in the regions of interest. Such materials could

[3] PI 2600 series from HD MicroSystems™

enhance the thermal conductivity while keeping the electrical insulation.

Future development regarding trap fabrication could be the integration of useful optical elements such as laser waveguides [MBM+16, WLK+19, MZM+20] or photon detectors [SVL+17]. These elements, if integrated, would then decrease experimental complexity since the same functions are currently provided by elements outside of the experimental vacuum chamber. Another useful feature would be the inclusion of through-substrate vias for contacting the front and backside of the ion trap, thus removing the need for wirebonding close to the trap and consequently enhancing laser optical access [GFS+15, VOW+17]. Another option to enhance optical access to the trap is to use three-dimensional structures which allow for optimization of the laser access such as the geometry described in [Mau16].

3.2 Multilayer trap simulations

As explained in Chapter 2, all traps with an integrated microwave conductor have to be simulated and tested to ensure the correct oscillating quadrupole field pattern. For the multilayer trap named 'ML5G', discussed in this chapter (a picture of the trap is shown in Fig. 2 of **P3**), the results have been published in the peer-reviewed article **P3** and reported in Tab. 3.1. The simulation and measurement procedure is the same as for the previous single-layer trap.

	$B\,[\mu\mathrm{T}]$	$B'\,[\mathrm{T/m}]$	$\alpha\,[^\circ]$	$\beta\,[^\circ]$	$\psi\,[^\circ]$	$x_0\,[\mu\mathrm{m}]$	$z_0\,[\mu\mathrm{m}]$
Sim.	1.47	54.8	40.8	87.3	0.1	34.72	0.73
Exp.	$\lesssim 34$	54.8(1.2)	-	86.8(1.7)	1.5(7.6)	34.62(0.05)	0.6(0.7)

Table 3.1: Parameters of the microwave near-field according to Eq. 2.1, determined from simulations and from experimental measurements of the surface-electrode trap 'ML5G' as reported in publication **P3**.

For the trap 'ML5G', a three-layer structure was chosen, two metal layers and one interconnect, to demonstrate the feasibility of the process. Additional layers will be considered for future trap generations where more complex structures are needed. In the fabricated trap, the bottom metal layer L_1 contains

the feedline and bottom part of the MWM conductor; the top metal layer L_2 contains all other feedlines and electrodes: RF, DC and two MWC conductors. The RF electrode has been designed without a shielding ground plane to avoid an increase in the trap capacitance. The measured trap capacitance is 3.28 pF as reported in Chapter 6 of [Hah19].

The layout shown in Fig. 1 c) of **P3**, a 3D microwave conductor with an insulator filled pocket, was found out to be an ideal geometry to achieve the overlap between the magnetic field quadrupole minimum and the pseudopotential minimum along the vertical (x) direction. It is not possible to achieve this overlap either with conductors lying on a single plane or with a full metal conductor, i.e. $l_{\mathrm{th}} = 0\,\mu$m.

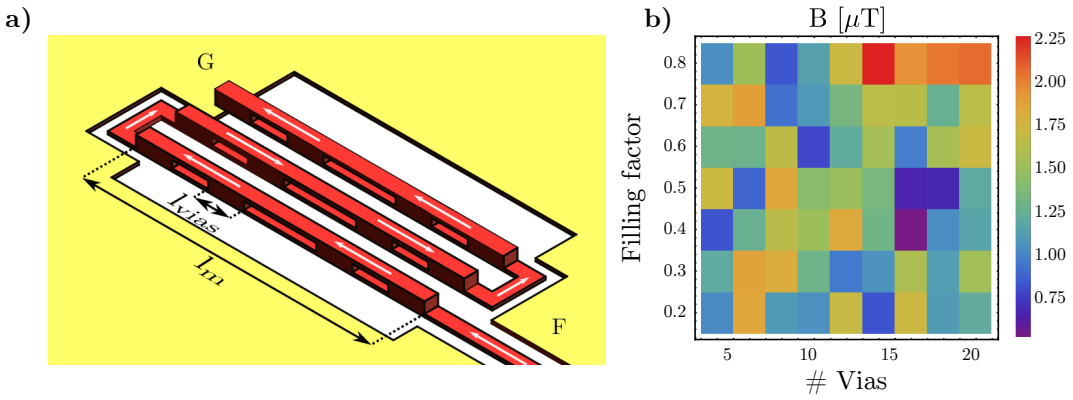

Figure 3.2: a) Schematic of a 4 vias design with $FF = 0.5$ b) residual B field map for 1 W input power on conductor MWM for designs with multiple vias and different filling factor. The trap 'ML5G' with 2 vias and $FF = 0.8$ expected $B = 0.82\,\mu$T from the FEM simulation model.

Other designs for the three-dimensional MWM conductor have been considered, this is because the fabrication process is more reliable for interconnects with smaller areas in layer V_1. Therefore the design of the interconnects between the top and bottom layer has been analyzed to study the behavior of the conductor under interconnect variation. A schematic of these alternative designs is shown in Fig. 3.2 a). The number of vias and their filling factor has been varied, which is defined as $FF = Nl_{\mathrm{vias}}/l_m$, where l_{vias} corresponds to the length of a single via, N is the total number of vias and $l_m = 1\,$mm corresponds to the length of a single MWM conductor segment. The integer N

is always even numbered so that a insulator pocket larger than the others is always present in the central region. The MWM structure in the fabricated trap 'ML5G' is effectively a two-via design with a $FF = 0.8$. Assuming an input power of 1 W at the expected $^9Be^+$ qubit frequency on conductor MWM, the simulation model predicts a residual field of $B = 0.82\,\mu$T at the quadrupole minimum. In Fig. 3.2 b) is shown the simulation result for alternative designs of conductor MWM with changing N and FF. Most of the alternative simulated structures present similar or worse characteristics than the 'ML5G' design fabricated. It is interesting to note that there is no optimal design considering only the near-field requirements. However, it is clear that, given the thermal conduction requirements, it is necessary to keep FF as high as possible, i.e low l_{th}. In this condition the simulations show that higher residual B are obtained for a large number of vias, making the 'ML5G' design the best combination when considering the thermal and magnetic field properties.

3.3 Carrier coupling

One issue that was noticed during the operation of the single-layer trap 'Spydertrap' was the strong coupling produced between the main MWM conductor and the carrier one, MWC. As reported in [Wah16], this can lead to induced currents reflected at different steps in the microwave electronic chain and propagating back to the trap structures. These currents produce an oscillating magnetic field at the same frequency of the magnetic field quadrupole and therefore modify its properties, as already mentioned in Sec. 2.3. The most important effect is a displacement of the quadrupole minimum compared to the simulated position and a variation of the residual field experienced by the ion.

To quantify the coupling between different electrodes we use the matrix elements, called S-parameters, of the scattering matrix for multi-port devices, they represent the coupling between the different ports of the trap. The single-layer trap 'Spydertrap' has an S-parameter of $-9.0\,$dB for the coupling between the MWC and MWM conductors; as discussed in Sec. 4.2.4 of [Wah16], low values indicate better electrode isolation. This coupling means that the quadrupole minimum can move by more than $1\,\mu$m from the expected position assuming a reflection amplitude of about 1%, as shown in Fig. 4.21 of [Wah16]. In the multilayer trap there are 2 MWC conductors which, as

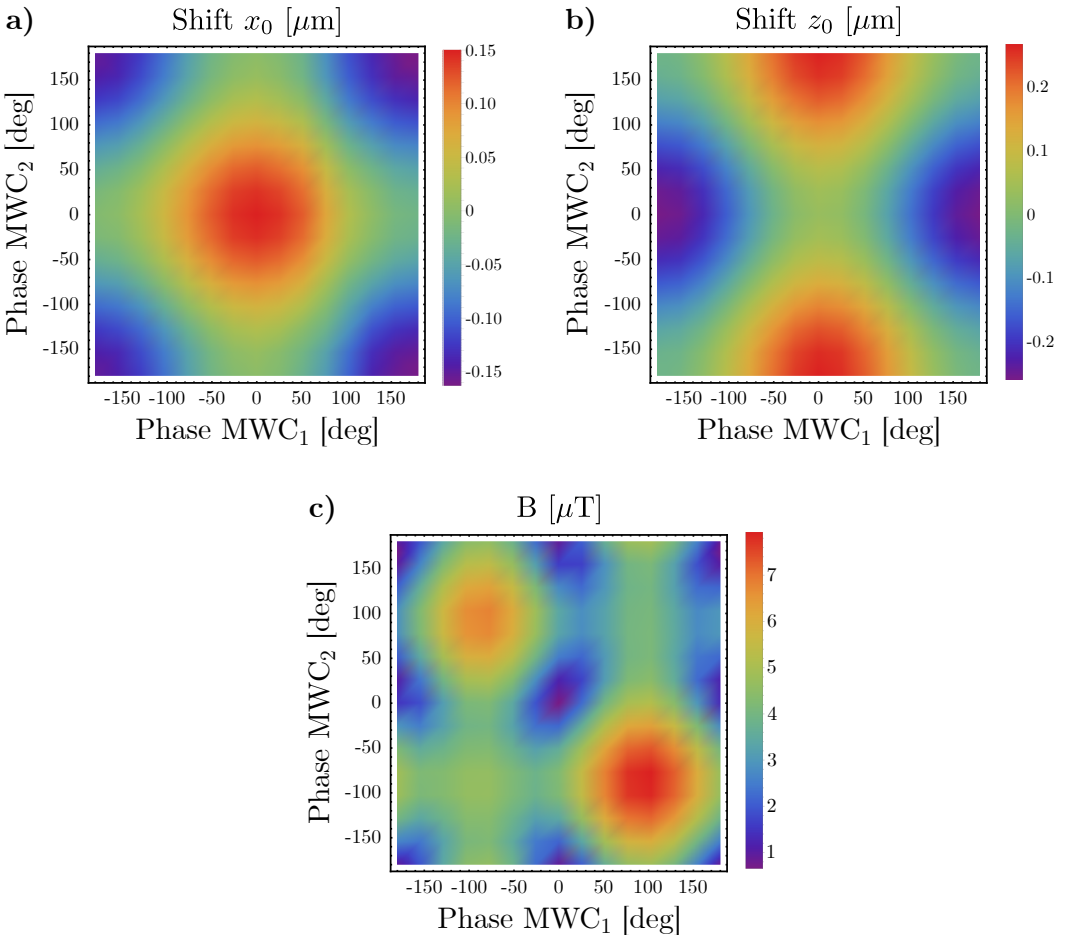

Figure 3.3: Simulated effect of a fully backreflected current from the 2 carriers with a 1 W input power on MWM. The phase on each current depends on the transmission line a) map of shift x_0 b) map of shift z_0, c) map of residual B field.

described in peer-reviewd publication **P3**, have S-parameters of -27.9 and -27.8 dB respectively. In the fabricated trap the MWC ground has been connected through the interconnect layer $V1$ to reduce the number of wirebonds to maximize optical access. Lower S-parameters could have been achieved by connecting the ground of the MWC conductors on the filterboard instead due to the reduced resistive coupling between MWC and MWM. In the publication, the effect of a total back reflected current as a function of the phase in electrode MWC$_2$ is reported. In Fig. 3.3 one can observe the combined effect of two fully reflected currents on the magnetic field quadrupole[4]. By the in-

[4]Note that the oscillation of the z_0 shift as a function of MWC$_2$ phase is different from the published one. This is due to a mistake in reference frame when producing Fig. 4 of **P3**, where the sign of the shift should be inverted.

teraction of two fields it is possible to achieve even larger shifts. This already intuitively explains that in a future multi-site surface-electrode trap based on the microwave near-field approach, it will be of high relevance to minimize the coupling between different electrodes to avoid issues such as the one just described.

3.4 P2: Multilayer ion trap technology for scalable quantum computing and quantum simulation

Authors: A. Bautista-Salvador, **G. Zarantonello**, H. Hahn, A. Preciado-Grijalva, J. Morgner, M. Wahnschaffe and C. Ospelkaus.

Journal: New Journal of Physics

DOI: 10.1088/1367-2630/ab0e46

Author contribution: ABS, JM and MW developed the fabrication method. ABS and APG fabricated the trap. JM and MW performed the preliminary FEM simulations. **GZ** and MW designed the trap used in the experiments. HH designed the experimental apparatus. **GZ** and HH performed and analyzed the measurements reported in the article. CO devised the experiment plan. All authors participated in the realization of the manuscript.

New Journal of Physics
The open access journal at the forefront of physics

Deutsche Physikalische Gesellschaft DPG
IOP Institute of Physics

Published in partnership with: Deutsche Physikalische Gesellschaft and the Institute of Physics

OPEN ACCESS

RECEIVED
4 December 2018

REVISED
1 February 2019

ACCEPTED FOR PUBLICATION
8 March 2019

PUBLISHED
8 April 2019

PAPER

Multilayer ion trap technology for scalable quantum computing and quantum simulation

A Bautista-Salvador[1,2,3], **G Zarantonello**[1,2], **H Hahn**[1,2], **A Preciado-Grijalva**[1], **J Morgner**[1,2], **M Wahnschaffe**[1,2,3] **and C Ospelkaus**[1,2,3]

[1] Physikalisch-Technische Bundesanstalt, Bundesallee 100, D-38116, Braunschweig, Germany
[2] Institute of Quantum Optics, Leibniz Universität Hannover, Welfengarten 1, D-30167, Hannover, Germany
[3] Laboratory for Nano- and Quantum Engineering, Leibniz Universität Hannover, Schneiderberg 39, D-30167, Hannover, Germany

E-mail: amado.bautista@ptb.de

Keywords: surface-electrode ion trap, atom chip, microfabrication, quantum logic and simulation

Abstract

We present a novel ion trap fabrication method enabling the realization of multilayer ion traps scalable to an in principle arbitrary number of metal-dielectric levels. We benchmark our method by fabricating a multilayer ion trap with integrated three-dimensional microwave circuitry. We demonstrate ion trapping and microwave control of the hyperfine states of a laser cooled $^{9}Be^{+}$ ion held at a distance of 35 μm above the trap surface. This method can be used to implement large-scale ion trap arrays for scalable quantum information processing and quantum simulation.

1. Introduction

Trapped ions are not only one of the most promising platforms for the practical implementation of quantum computing and quantum simulations, but also sensitive systems for measuring very small magnetic and electric fields. Typically, they are held in Paul or Penning traps at high vacuum, laser cooled close to absolute zero temperature, and their internal states coupled to their motion can be manipulated with high fidelity by either laser fields [1, 2] or microwave radiation [3, 4]. However, scaling these elementary demonstrations to larger systems remains a formidable technological challenge [5].

Surface-electrode ion traps [6] represent a strong candidate for the realization of a quantum charge-coupled device [7, 8] for scaling quantum logic operations. Such an ion trap array could feature dedicated zones for storing, manipulation and read-out, thus promising a modular hardware for quantum computation and quantum simulation [9]. Conventionally, in surface-electrode ion traps all electrodes are built in a single plane by standard microfabrication techniques [10]. First integration of key scalable elements into a single layer chip such as micro-optical components [11], nanophotonic waveguide devices [12] or microwave conductors (MWC) [13] have been demonstrated. However, interconnecting separated components built in this system imposes new challenges on trap design where signal lines have to be routed around other elements. Therefore, the realization of a highly integrated large-scale ion trap device requires a more flexible approach where signal routings can be distributed on vertically well-separated levels of interconnects.

Demonstrations of multilayer processes in ion traps so far are based on techniques borrowed from microelectromechanical systems (MEMS) [14, 15] or CMOS [16, 17]; however the resulting trap structures are limited to thin interconnect levels. Moreover, there is a need of a nearly material-independent processing capable of including most dielectric substrates and thick metallization. For example, room temperature and cryogenic operation each favor different dielectric substrates when it comes to high thermal conductivity and low rf loss tangent. Thick metallization, when combined with narrow gaps between neighboring electrodes, allows for efficient shielding of the ion(s) from charges that might accumulate on top of exposed dielectrics in between electrodes and affect the ion(s) in an uncontrolled way [18]. Thick metallization can support strong currents for integrated control elements based on static or oscillating magnetic field gradients [19, 20]. Thick vertical interconnect access (VIAS) are of general interest for building ion trapping devices as they allow to

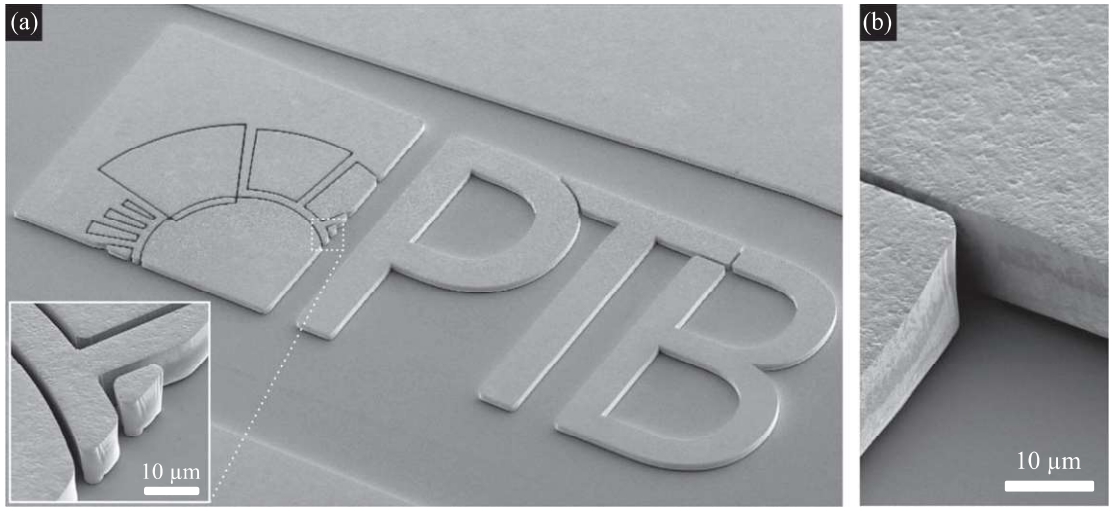

Figure 1. Gold structures with high aspect ratio supported on sapphire. (a) Au structures separated by gaps of about 2 μm with a high aspect ratio of 5:1 (inset). (b) Pair of Au electrodes separated by a 0.8 μm gap, resulting in a gap with an aspect ratio of 14:1. For both SEM micrographs shown in (a) and (b) the sample is tilted by 45°.

minimize parasitic capacitances and crosstalk and reduce the risk of chip electrical breakdown. Any fabrication process will have to comply with the specific requirements of an ion trap, such as a material mix which features extremely low material outgassing and needs to be compatible with ultra-high vacuum operation, low dielectric losses and non-magnetic metal surfaces.

Here we present a robust fabrication method, scalable to an in principle arbitrary number of planarized thick metal-dielectric layers, enabling the realization of scalable ion trap devices. The method complies with the stringent requirements of a scalable ion trapping array, allowing the fabrication of complex trap designs using relatively forgiving fabrication techniques on nearly any type of substrate (sapphire, quartz, AlN, Si, …) and insulating dielectrics such as polyimide, teflon or BCB. To demonstrate the approach, we fabricate and operate a multilayer ion trap chip with three-dimensional (3D) microwave circuitry towards the realization of high fidelity muli-qubit gates [13]. A fabrication yield of above 80% is achieved, limited by the stringent geometric requirements for the particular application of integrated near-field microwave control. For a more conventional multilayer design yields exceeding 90% should be possible.

2. Fabrication methods

Methods for building surface-electrode ion traps [10] or atom chips [21, 22] are typically based on standard semiconductor processing. For the simplest case, in which all metal electrodes are aligned in a single plane, a generic fabrication workflow consists of a three-step processing: wafer patterning, electrode formation and electric insulation. Depending on the requirements one will choose between different materials and processing methods at hand. In what follows we will describe our own fabrication methods to build single layer and multilayer microfabricated ion traps.

2.1. Single level processing (SLP) method

For the SLP method all steps are carried out on 3 inch diameter wafers in a fabrication line located at Physikalisch-Technische Bundesanstalt, Braunschweig. We have fabricated similar structures to the ones presented in figure 1 on AlN, sapphire, organic polymers and high resistivity (HiR) float zone Si wafers, demonstrating the compatibility of the method with a wide range of substrates suitable for ion trap technology.

The first step during wafer preparation involves the deposition of a Ti adhesion layer (15 nm thin) and an Au seed layer (50 nm thin) on top of the substrate by resistive evaporation. The first film acts as an adhesion promoter between the substrate and the Au seed layer, and the second film serves as a starting conductive layer for a later electrodeposition step.

Second, to define the trap geometry, a 25 μm thick positive or 16 μm thick negative resist is spin coated on top of the Au seed layer and the wafer is exposed to UV light by contact lithography. A subsequent development of the exposed resist results in open areas on the substrate which are filled to a desired thickness by electrodeposition of Au in a sulphite-based bath.

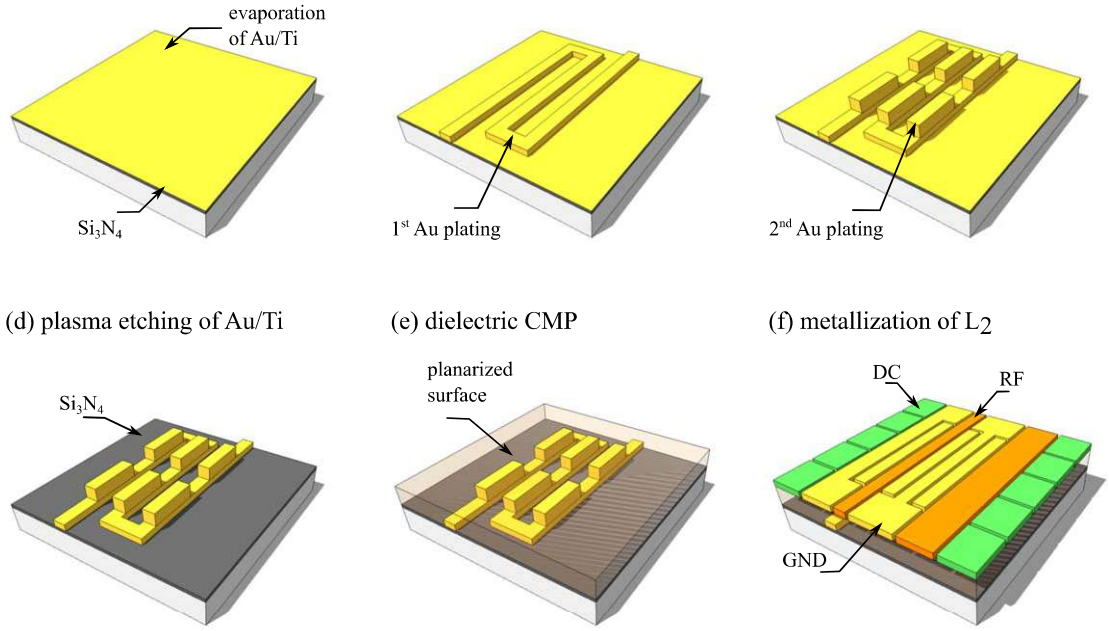

Figure 2. Schematics of the multilevel processing flow. (a) A wafer is coated with an SiN film and a conductive Au/Ti bilayer. (b) A lower level (L_1) is formed via electroplating. (c) A via V_1 is electroplated on top of L_1. (d) Dry etching of Au/Ti bilayer film. (e) A polymer is spin coated over both L_1 and V_1 and subsequently planarized by CMP. (f) A second metallization L_2 repeating steps (a), (b) and (d) on a planarized dielectric surface. Exposed dielectric between electrodes in L_2 is removed by plasma etching down to the top surface of the Si_3N_4 layer.

Finally, after gold electroplating the resist mask is removed chemically and the wafer is cleaned under oxygen-based plasma etching. Additionally, the wafer is exposed to a fluorine-based plasma to further remove possible resist debris. Immediately afterwards the seed Au layer is removed via Ar etching and the Ti layer removed by a fluorine-based plasma etching.

This method allows the fabrication of gold structures with high aspect ratios as exemplified in figure 1. Gold structures with a width as narrow as 5 μm and gap separation as narrow as 2 μm are shown in figure 1(a). Another example is depicted in figure 1(b) consisting of a pair of gold electrodes separated by a gap with an aspect ratio of 14:1. One additional advantage of the method is that after dry etching of the Au/Ti bilayer the resulting trap surfaces have a superior finishing quality compared to the commonly used wet etching.

2.2. Multilevel processing (MLP) method

In this section a MLP method is presented, which combines techniques borrowed from MEMS and Integrated Circuits processing. The method is also compatible with other common substrates used for ion trap technology such as silicon, sapphire, borosilicate glass and quartz.

To demonstrate the simplicity and robustness of our method we have fabricated an ion trap with integrated 3D microwave circuitry. It comprises a lower interconnect level L_1 and an upper electrode level L_2. An additional vertical interconnect access V_1, called via, allows microwave signals to be transmitted between levels. A more detailed description of the microwave and quantum logic aspects of the trap design and the corresponding characterization will be covered elsewhere [26].

The method presented here mainly consists of six processing steps: (a) wafer preparation, (b) metallization of lower level L_1, (c) metallization of via V_1, (d) removal of seed layer, (e) deposition and planarization of dielectric layer D_1 and (f) metallization of upper level L_2. A schematics of the fabrication flow is given in figure 2.

The supporting material is a 3 inch silicon wafer with HiR ($\sigma > 1 \times 10^4$ Ωcm). On top of it and as shown in figure 2(a), a 2 μm thick film of Si_3N_4 is deposited by physical enhanced chemical vapor deposition. This dielectric film may improve trap operation by avoiding detrimental diffusion of Au into silicon and increasing the flashover voltage as demonstrated in [23]. Thereafter, a 10 nm thin layer of Ti and a 50 nm thin layer of Au are thermally evaporated on top of Si_3N_4.

To build the lower level L_1 on top of Si_3N_4/Si, a negative resist is spin coated and patterned via UV lithography. Once the negative resist is developed to form a resist mold, gold electrodes are grown (4 μm) by electroplating as depicted in figure 2(b). After electroplating is completed, the resist mask is stripped and the wafer cleaned under plasma etching.

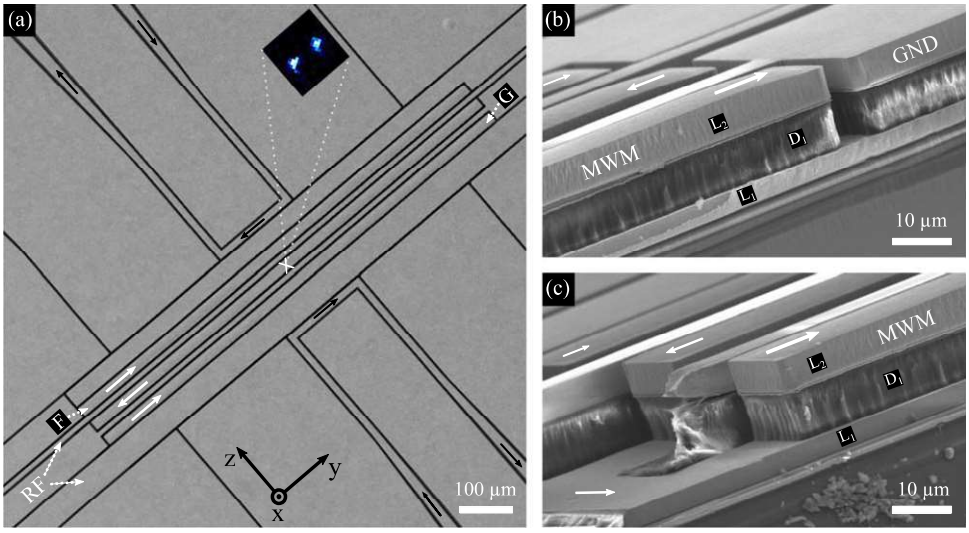

Figure 3. SEM micrograph of the central part of a trap chip fabricated using the MLP method. White and black arrows are drawn on top of the microwave conductors as a guide for the eye. (a) Upper metal level L_2 of the trap chip in which black lines correspond to electrode gaps of about 5 μm. (b) Part of a cleaved chip showing a cross-section mainly on the *xy*-plane around position 'G'. (c) Similar to (b) but with a close-up corresponding to position 'F' in (a). Ions are trapped at $d = 35$ μm above the position marked as '*X*'.

For the metallization of the via V_1 we repeat the photolithography and electroplating steps presented in (b) but this time on top of L_1 by using a thick (>12 μm) developed negative resist as a plating mold. Electroplated VIAS grown up to 10 μm on top of L_1 are depicted in figure 2(c) after stripping the negative resist mask and plasma cleaning of the wafer.

To remove the Au seed layer and the Ti adhesion layer we use the last dry etching step from the SLP method. This step allows a controllable etch of Au and Ti of 50 nm min^{-1} and 10 nm min^{-1} respectively, resulting in a minimal change of the surface quality on top of both L_1 and V_1 surfaces. The electrically isolated elements on V_1 and L_1 are schematically illustrated in figure 2(d).

Polyimide (PI 2600 series, HD MicroSystems^{TM}) is then spin coated on top of L_1 and V_1 (figure 2(e)). After thermal curing, excess material is present on top of the underlying structures L_1 and V_1. The imprinted dielectric topography is globally planarized through a chemical-mechanical polishing step, which is stopped at the top of V_1 or close to it. To assure electrical contact between V_1 and the subsequent level L_2 a global or local etch-back process is performed. In the case of a local etch-back, this requires an additional photolithography step. In that case, the resulting resist mask covers the PI film everywhere except on defined zones on top of the V_1 area. After performing a fluorine-based plasma etch, the remaining material on top of V_1 is completely removed.

To define the top metal layer the SLP method is again employed but this time on top of the planarized polymer surface (figure 2(f)). Once the plating has been completed (5 μm) and the resist mold removed, the remaining polymer film between gaps underneath and between the electrodes in L_2 is etched down to the Si_3N_4 layer by a fluorine-based plasma to hide possible patch potentials built on the exposed insulator.

3. Fabrication outcome and trap operation

Here we briefly present the design and characterization of a trap with 3D MWC integrated into a microfabricated ion trap using the MLP method. The microwave circuitry is embedded to implement quantum logic operations using near-field microwaves [13, 20, 24, 25]. The specific design is discussed elsewhere in detail [26] and here only described as one of many scenarios that benefits from the multilayer technology.

In the upper level (L_2) the trap includes two RF electrodes and ten DC electrodes to confine the ions to a local minimum (x_0, z_0), see figure 3(a). A microwave signal (white arrows) of frequency 1 GHz can be applied on a 3D microwave meander (MWM) conductor between two contact points labeled as 'F' and 'G', thus generating an oscillating magnetic near-field gradient '*B*' in the *xz*-radial plane with a local minimum at (x_1, z_1). The three apparent independent MWC indicated by the white arrows are indeed part of a single 3D MWM connected to L_1 by VIAS and routed over L_1 as indicated in figure 3. A central part of a diced trap chip (5 mm × 5 mm) fabricated using the MLP method is presented in figure 3(a). There are also two additional MWC surrounding the central DC electrodes, in which an oscillating current (black arrows) can be applied to produce an oscillating *B* field.

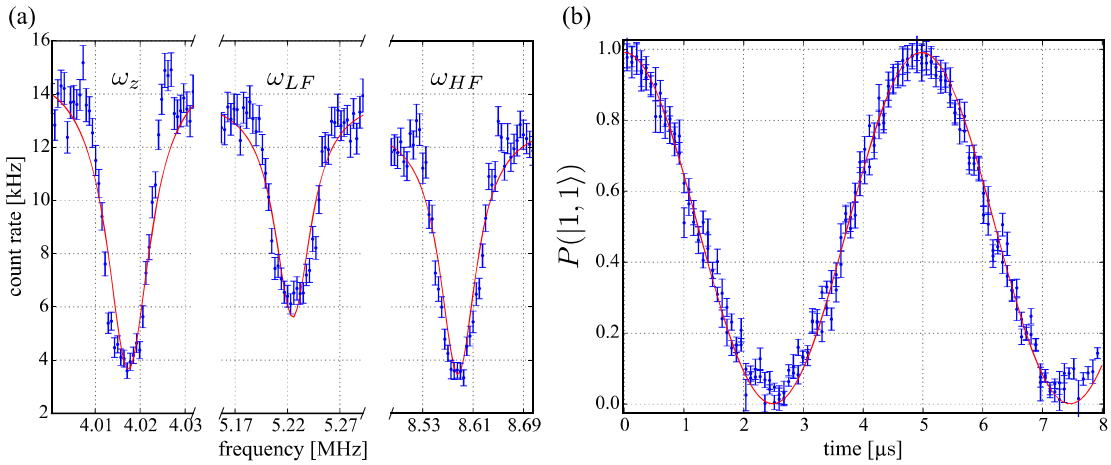

Figure 4. Secular frequencies and microwave qubit transition. (a) Motional frequency measurements using the DC tickle method. The (red) solid lines show Lorentzian fits to the data. The left axis corresponds to the photon average counts after a fluoresence detection of 1.3 ms. (b) Rabi flopping on the qubit transition using a microwave conductor embedded in the trap driving the $|F = 1,\ m_F = +1\rangle \leftrightarrow |F = 2,\ m_F = +1\rangle$ [27] transition.

A cleaved chip revealing a cross-section view of the metal-dielectric stack around position 'F' and position 'G' is shown in figures 3(b) and (c), respectively. The ion trap (RF and DC electrodes) as well as the uppermost part of the MWM conductor are entirely located in L_2, whereas the microwave signals and the ground plane are routed between L_1 and L_2 through VIAS in V_1 (not visible in the micrograph but behind D_1 in figures 2(b) and (c)). Any remaining non-planarity is due to imperfections in the etch-back process and independent of the number of metal-dielectric layers implemented. It can be made much smaller than 1 μm, which again is small compared to the typical ion-to-electrode distance.

Removing both Au and Ti films by means of dry etching has improved the trap surface quality. For a similar chip as the one here presented an rms roughness $R_{\mathrm{rms}} = 8.3 \pm 0.5$ nm is obtained by atomic-force microscopy over an area of 25 μm $\times$ 25 μm. This represents a two-order of magnitude improvement when compared to a wet etching process using aqua regia [27]. These nearly mirror-like surfaces are relevant since there is a reduction of stray light scattered in the direction perpendicular to the trap surface during resonance fluorescence imaging for ion state detection. Also an ion trap with minimal surface roughness might be less prone to anomalous motional heating at cryogenic temperatures [28].

The diced trap chip is glued onto a copper block and wirebonded to a custom printed circuit board for filtering and signal routing. The whole assembly is installed in a vacuum system at a pressure better than 1×10^{-11} mbar and connected to an in-vacuum coaxial resonator similar to the one used in [29]. For ion loading we employ a laser ablation scheme [27] and subsequent two-photon ionization using 235 nm light [30]. Single $^9Be^+$ ions are loaded at 35 μm above the upper surface of L_2 around the position 'X' (see figure 3(a)).

For an RF drive frequency of $\Omega_{\mathrm{RF}} = 2\pi \times 176.5$ MHz with amplitude $V_{\mathrm{RF}} = 100$ V and supplied DC voltages ranging within ± 25 V, we measure secular trap frequencies of $(\omega_z, \omega_{\mathrm{LF}}, \omega_{\mathrm{HF}}) = 2\pi \cdot (4.02, 5.23, 8.59)$ MHz. To determine the trap frequencies we apply an oscillating tickle voltage to one of the DC electrodes and scan the frequency [31]. Once the tickle drive is resonant with a secular frequency, the motion of the ion is excited and the ion fluorescence drops (figure 4(a)).

Finally we employ the integrated MWC to manipulate the internal state of the ion. Figure 4(b) shows Rabi oscillations on the qubit transition $|F = 1,\ m_F = +1\rangle \leftrightarrow |F = 2,\ m_F = +1\rangle$ [27] of the electronic ground state $^2S_{1/2}$ of a single $^9Be^+$ ion at an external magnetic field of $|\boldsymbol{B}_0| = 22.3$ mT when applying a microwave current of frequency $\omega_0 \simeq 1\ 082.55$ MHz to one of the MWC conductors. Here, F is referring to the total angular momentum $\boldsymbol{F}$ and m_F the quantum number of its projection on $\boldsymbol{B}_0$. The state readout is carried out via ion fluorescence detection on the closed-cycling transition $|S_{1/2},\ F = 2,\ m_F = 2\rangle \rightarrow |P_{3/2},\ m_J = +3/2,\ m_I = +3/2\rangle$, combined with suitable microwave transfer pulses [27].

4. Conclusion and outlook

We have presented a novel multilayer method for fabricating scalable surface-electrode ion traps. The flexibility and robustness of the method allows to benchmark the integration of 3D microwave circuitry into a multilayer

ion trap. Furthermore, we have demonstrated successful trapping of $^{9}Be^{+}$ and basic qubit manipulation by applying microwave oscillating currents on one of the conductors.

The MLP method presented here can in principle be extended to a nearly arbitrary number of layers to comply with the stringent needs of scaling surface-electrode ion traps. Moreover, the method permits the integration of 3D and planarized features with high aspect ratio. This technique opens new routes towards the realization of more complex and powerful ion trap devices.

In contrast to a typical CMOS situation where the 'device' is fabricated on top of the substrate, with interconnect layers on top of the device, in our case the 'device' is the top electrode layer which is controlling the ion(s), whereas the layers closer to the substrate are used as interconnects. In the future, these lower interconnects may be combined with through-wafer VIAS to achieve contacting of the ion trap chip from the back-side, eliminating the need of wirebonds and likely obstruction of laser beams. Through-wafer slots for back-side ion loading can also be produced in the same way. These same techniques could be applied to realize so-called analog quantum simulators in ion trap arrays [32–34], possibly with integrated control [35]. Moreover, such an approach may enable the embedding of complex integrated components such as trench capacitors [36, 37], low-loss integrated waveguides [38]; or the realization of more elaborate devices including reliable ion-transport junctions [39, 40], increased optical access [17] or manipulation of scalable arrays of two-dimensional trapped ion systems [33, 34].

The MLP method can also be used to extend multilayer 'atom chips' [22, 41, 42] or to fabricate scalable hybrid atom-ion traps [43, 44] for quantum many-body physics experiments and quantum sensing with neutral atoms. In this context the thick metal conductors can support substantial currents required for magnetic trapping and the planarization together with the demonstrated minimized surface roughness allows the implementation of mirror-like surfaces and transfer coatings for integrated magneto-optical traps.

Acknowledgments

We acknowledge support by the PTB cleanroom facility team, in particular T Weimann and P Hinze. We also acknowledge support by the LNQE cleanroom staff in particular O Kerker. We acknowledge funding from PTB, QUEST, LUH, NTH (project number 2.2.11) and DFG through CRC 1227 DQ-*mat*, project A01.

ORCID iDs

C Ospelkaus https://orcid.org/0000-0002-4170-2936

References

[1] Gaebler J *et al* 2016 *Phys. Rev. Lett.* **117** 060505
[2] Ballance C, Harty T, Linke N, Sepiol M and Lucas D 2016 *Phys. Rev. Lett.* **117** 060504
[3] Harty T, Sepiol M, Allcock D, Ballance C, Tarlton J and Lucas D 2016 *Phys. Rev. Lett.* **117** 140501
[4] Weidt S, Randall J, Webster S, Lake K, Webb A, Cohen I, Navickas T, Lekitsch B, Retzker A and Hensinger W 2016 *Phys. Rev. Lett.* **117** 1079–7114
[5] Monroe C and Kim J 2013 *Science* **339** 1164–9
[6] Seidelin S *et al* 2006 *Phys. Rev. Lett.* **96** 253003
[7] Wineland D J, Monroe C R, Itano W M, Leibfried D, King B E and Meekhof D M 1998 *J. Res. Natl Inst. Stand. Technol.* **103** 259–328
[8] Kielpinski D, Monroe C and Wineland D J 2002 *Nature* **417** 709–11
[9] Lekitsch B, Weidt S, Fowler A G, Mølmer K, Devitt S J, Wunderlich C and Hensinger W K 2017 *Sci. Adv.* **3** e1601540
[10] Hughes M D, Lekitsch B, Broersma J A and Hensinger W K 2011 *Contemp. Phys.* **52** 505–29
[11] Merrill J T *et al* 2011 *New J. Phys.* **13** 103005
[12] Mehta K K, Bruzewicz C D, McConnell R, Ram R J, Sage J M and Chiaverini J 2016 *Nat. Nanotechnol.* **11** 1066–70
[13] Ospelkaus C, Warring U, Colombe Y, Brown K R, Amini J M, Leibfried D and Wineland D J 2011 *Nature* **476** 181–4
[14] Cho D I D, Hong S, Lee M and Kim T 2015 *Micro Nano Syst. Lett.* **3** 1
[15] Hong S, Lee M, Cheon H, Kim T and Cho D I D 2016 *Sensors* **16** 616
[16] Stick D, Fortier K M, Haltli R, Highstrete C, Moehring D L, Tigges C and Blain M G 2010 arXiv:1008.0990
[17] Maunz P L W 2016 High optical access trap 2.0 *Technical Report* SAND-2016-0796R Sandia National Lab. (SNL-NM), Albuquerque, NM (United States)
[18] Schmied R 2010 *New J. Phys.* **12** 023038
[19] Mintert F and Wunderlich C 2001 *Phys. Rev. Lett.* **87** 257904
[20] Ospelkaus C, Langer C E, Amini J M, Brown K R, Leibfried D and Wineland D J 2008 *Phys. Rev. Lett.* **101** 090502
[21] Treutlein P 2008 Coherent manipulation of ultracold atoms on atom chips *PhD Thesis* Ludwig-Maximilians-Universität München
[22] Fortágh J and Zimmermann C 2007 *Rev. Mod. Phys.* **79** 235
[23] Sterling R C, Hughes M D, Mellor C J and Hensinger W K 2013 *Appl. Phys. Lett.* **103** 143504
[24] Warring U, Ospelkaus C, Colombe Y, Brown K R, Amini J M, Carsjens M, Leibfried D and Wineland D J 2013 *Phys. Rev.* A **87** 013437
[25] Carsjens M, Kohnen M, Dubielzig T and Ospelkaus C 2014 *Appl. Phys.* B **114** 243–50

[26] Hahn H, Zarantonello G, Bautista-Salvador A, Wahnschaffe M, Kohnen M, Schoebel J, Schmidt P O and Ospelkaus C 2018 arXiv:1812.02445
[27] Wahnschaffe M, Hahn H, Zarantonello G, Dubielzig T, Grondkowski S, Bautista-Salvador A, Kohnen M and Ospelkaus C 2017 *Appl. Phys. Lett.* **110** 034103
[28] Lin K Y, Low G H and Chuang I L 2016 *Phys. Rev.* A **94** 013418
[29] Jefferts S R, Monroe C, Bell E W and Wineland D J 1995 *Phys. Rev.* A **51** 3112
[30] Leibrandt D R, Clark R J, Labaziewicz J, Antohi P, Bakr W, Brown K R and Chuang I L 2007 *Phys. Rev.* A **76** 055403
[31] Home J P, Hanneke D, Jost J D, Leibfried D and Wineland D J 2011 *New J. Phys.* **13** 073026
[32] Porras D and Cirac J I 2004 *Phys. Rev. Lett.* **92** 207901
[33] Mielenz M *et al* 2016 *Nat. Commun.* **7** 11839
[34] Bruzewicz C D, McConnell R, Chiaverini J and Sage J M 2016 *Nat. Commun.* **7** 13005
[35] Chiaverini J and Lybarger W E 2008 *Phys. Rev.* A **77** 022324
[36] Allcock D T C *et al* 2012 *Appl. Phys.* B **107** 913–9
[37] Guise N D *et al* 2015 *J. Appl. Phys.* **117** 174901
[38] West G N, Loh W, Kharas D, Sorace-Agaskar C, Mehta K K, Sage J, Chiaverini J and Ram R J 2019 *APL Photonics* **4** 026101
[39] Moehring D L, Highstrete C, Stick D, Fortier K M, Haltli R, Tigges C and Blain M G 2011 *New J. Phys.* **13** 075018
[40] Wright K *et al* 2013 *New J. Phys.* **15** 033004
[41] Trinker M, Groth S, Haslinger S, Manz S, Betz T, Schneider S, Bar-Joseph I, Schumm T and Schmiedmayer J 2008 *Appl. Phys. Lett.* **92** 254102
[42] Bohi P, Riedel M F, Hoffrogge J, Reichel J, Hansch T W and Treutlein P 2009 *Nat. Phys.* **5** 592–7
[43] Härter A and Denschlag J H 2014 *Contemp. Phys.* **55** 33–45
[44] Bahrami A, Müller M, Drechsler M, Joger J, Gerritsma R and Schmidt-Kaler F 2018 arXiv:1811.07670

3.5 P3: Multilayer ion trap with three-dimensional microwave circuitry for scalable quantum logic applications

Authors: H. Hahn[†], **G. Zarantonello**[†], A. Bautista-Salvador, M. Wahnschaffe, M. Kohnen, J. Schoebel, P. O. Schmidt and C. Ospelkaus.

Journal: Applied Physics B

DOI: 10.1007/s00340-019-7265-1

Author contribution: **GZ** and MW designed the trap used in the experiments and performed the FEM simulations. HH designed the experimental apparatus. ABS fabricated the trap and performed the heat dissipation simulations. HH and **GZ** performed and analyzed the measurement reported in the article. JS performed the S-parameter measurements and contributed to the simulation model. CO and POS devised the experiment plan. All authors participated in the realization of the manuscript.

Note[†] : HH and **GZ** contributed equally to this work.

Applied Physics B (2019) 125:154
https://doi.org/10.1007/s00340-019-7265-1

Applied Physics B
Lasers and Optics

Multilayer ion trap with three-dimensional microwave circuitry for scalable quantum logic applications

H. Hahn[1,2] · G. Zarantonello[1,2] · A. Bautista-Salvador[1,2,3] · M. Wahnschaffe[1,2,3] · M. Kohnen[1,2] · J. Schoebel[4] · P. O. Schmidt[1,2] · C. Ospelkaus[1,2,3]

Received: 4 December 2018 / Accepted: 21 July 2019 / Published online: 31 July 2019

Abstract
We present a multilayer surface-electrode ion trap with embedded 3D microwave circuitry for implementing entangling quantum logic gates. We discuss the electromagnetic full-wave simulation procedure that has led to the trap design and the characterization of the resulting microwave field pattern using a single ion as a local field probe. The results agree with simulations within the uncertainty; compared to previous traps, this design reduces detrimental AC Zeeman shifts by three orders of magnitude. The design presented here can be viewed as an entangling gate component in a library for surface-electrode ion traps intended for quantum logic operations.

1 Introduction

Trapped ions are a promising platform to explore applications in quantum simulation and quantum computation [1–4]. Towards the ultimate goal of a large-scale universal quantum machine solving specific problems with a quantum speed-up [5], milestones for first experimental implementations of quantum algorithms and quantum simulations have recently been achieved [6–9]. However, to improve their practical use in substantial problems, the number of stored and manipulated qubits as well as the fidelity of operations have yet to be increased significantly, highlighting the remaining key ingredient of a scalable architecture [10].

Surface-electrode traps [11], where all electrodes are located in a plane, represent a suitable scalable platform as they allow to implement elements of the so-called 'quantum CCD' architecture [12, 13]. Based on well-developed microfabrication techniques, surface traps unite an intrinsically scalable fabrication with a high degree of reproducibility. In such a planar geometry, the ion is trapped and influenced by the potentials that are applied to the metal electrodes located at the very top of the structure. Scaling to large arrays of ion traps [14] will lead to complex electrode arrangements and thus make it indispensable to incorporate interconnections to lower layers embedded into the structure [15–17]. Any such layer would be shielded from the ion by the top metal layer, but can be used to supply the electrodes in the top layer with control voltages.

For universal qubit manipulation, single- and multi-qubit gates driven by microwave radiation [18, 19] benefit from microfabricated traps as the control elements can be included as an integrated microwave conductor in the trap design. For qubits with transition frequencies in the RF or microwave regime, such as in $^9Be^+$, this enables direct access to the qubit transition and, for these atoms, thus avoids the necessity for a complex Raman laser system to carry out gates [20, 21]. In contrast to laser-based schemes, achievable fidelities of the microwave approaches [22–26] show no fundamental limit due to photon scattering [27] and are approaching the fault-tolerant regime for universal gate sequences [23, 28].

In this paper we introduce a microfabricated radio-frequency ion trap with integrated 3D microwave circuitry.

H. Hahn and G. Zarantonello contributed equally to this work.

✉ C. Ospelkaus
christian.ospelkaus@iqo.uni-hannover.de

[1] Physikalisch-Technische Bundesanstalt, Bundesallee 100, 38116 Braunschweig, Germany

[2] Institute of Quantum Optics, Leibniz Universität Hannover, Welfengarten 1, 30167 Hannover, Germany

[3] Laboratory for Nano- and Quantum Engineering, Leibniz Universität Hannover, Schneiderberg 39, 30167 Hannover, Germany

[4] Department for High-Frequency Technology, Technische Universität Braunschweig, Schleinitzstraße 22, 38106 Braunschweig, Germany

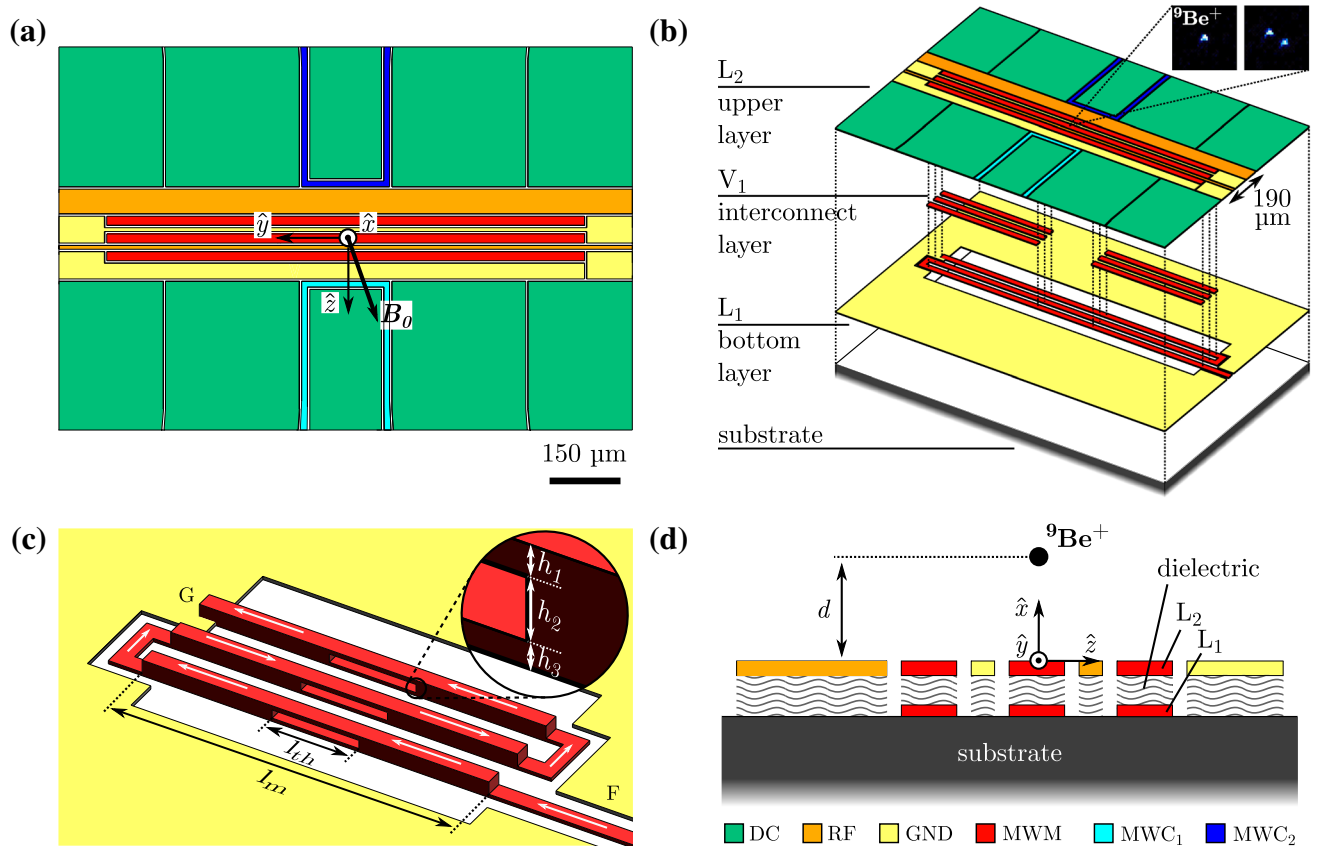

Fig. 1 Multilayer trap layout **a** electrode configuration of the upper layer L_2, **b** exploded-view of the three trap layers (dielectric material in L_1 and L_2 not shown). The inset gives the EMCCD camera signal for a single- and 2-ion crystal. **c** Schematic of the 3D meander-like microwave conductor MWM with distorted dimensions for clarity, showing its extension to the three fabrication layers L_1, V_1, and L_2 with respective thicknesses h_1, h_2 and h_3 (inset). White arrows indicate the direction of a hypothetic applied DC current as used in simulations for thermal effects (see "Appendix"). Surrounding electrodes as well as the dielectric material have been excluded for illustration purposes, **d** cross section of the RF electrodes and the 3D microwave conductor MWM in the radial xz-plane at $y = 0$. The dielectric material is used to isolate structures between the bottom and upper layer. For this trap configuration the ions are confined at $d \simeq 35\,\mu m$ above the surface of L_2

Besides two microwave conductors that can be used to drive single-qubit gates, the trap design features an embedded 3D microwave conductor with a meander-like shape that has been designed to carry out multi-qubit gates using microwave near-fields. The trap has been produced in a novel multilayer fabrication process enabling a scalable trap architecture based on microwave (near-field) quantum logic [30].

In Sect. 2 we briefly introduce the fabrication process, trap design, and experimental setup. Section 3 treats the design of the 3D microwave conductor usable for multi-qubit gates in more detail and highlights its advantages in terms of scalability and field properties when compared to a corresponding single-layer trap. In addition, we give a description of the full-wave simulation model used for extracting its resulting magnetic field configuration. In Sect. 4 we compare these simulations to experimental results, including an S-parameter measurement and a Ramsey-type, single-ion experiment to map out the produced field configuration. Finally, in Sect. 5 we summarize and conclude our findings.

2 Trap design and fabrication

The trap presented here is a multilayer extension of a surface-electrode ion trap with integrated microwave conductors [29] and consists of three individual fabrication layers called L_1, V_1 and L_2. Here, L_1 represents the bottom layer, L_2 the upper layer and V_1 the interconnect layer used to connect L_1 and L_2 where required (Fig. 1b). The fabrication process starts with a high-resistivity Si substrate coated with a 2 µm -thick insulating Si_3N_4 layer by plasma-enhanced chemical vapor deposition (PECVD). After thermally evaporating a 10 nm-thin layer of Ti and a 50 nm-thin layer of Au on top of the Si_3N_4 layer, the bottom layer L_1 is metallized by UV photolithography and a subsequent gold electroplating step.

The metallization of the interconnect layer V_1 follows the same procedure as for L_1. After removing the Ti adhesion and Au seed layers with plasma etching, a dielectric film is spin-coated on top of V_1 and L_1 (Fig. 1d). Dielectric used is Polyimide (PI 2600 series, HD MicroSystems™). A chemical-mechanical polishing (CMP) step is used to planarize the top dielectric surface. To ensure electrical contact between part of V_1 and L_2 we first perform a global etch-back process and stop close to the top part of V_1. Then we perform a local etch-back process on areas defined by photolithography on top of V_1.

To form the upper layer L_2 we repeat the steps used for L_1; Au/Ti deposition, UV photolithography and gold electroplating. As a final step, via plasma etching, we remove the adhesion and seed layer between the electrodes which would otherwise short out all electrodes in L_2, and the dielectric underneath down to either L_1 or to the substrate. For the trap described here, the resulting electrode thicknesses are $h_1 = 4.4\,\mu\text{m}$ for L_1, $h_2 = 9.5\,\mu\text{m}$ for V_1 and $h_3 = 5.2\,\mu\text{m}$ for L_2. The thickness values result from the optimization described in Sect. 3. The field required for electrical breakdown of the polymide is nominally $> 2 \times 10^8$ V/m. For the voltage here reported no electrical breakdown is expected. For further details on the general fabrication method, see Ref. [30].

Figure 1a shows the upper layer L_2 which holds all electrodes relevant for ion trapping, given by two RF electrodes for radial confinement (both originating from a common feedline) and ten DC electrodes for axial confinement. For this trap the resulting ion-to-electrode distance between the ions and L_2 is $d \simeq 35\,\mu\text{m}$ (Fig. 1d). A radio frequency signal with frequency $\omega_{\text{RF}} \simeq 2\pi \times 176.5\,\text{MHz}$ and amplitude $V_{\text{RF}} \simeq 100\,\text{V}$ is applied to the RF electrode. The voltages applied to the DC electrodes range between $\pm 26\,\text{V}$. For the experiments performed in Sect. 4 this corresponds to secular trap frequencies in axial and radial direction of $(\omega_{\text{ax}}, \omega_{\text{LF}}, \omega_{\text{HF}}) \simeq 2\pi \times (4.12, 5.6, 9.33)\,\text{MHz}$ for a single $^9\text{Be}^+$ ion. Based on calculations using the gapless plane approximation [31] the high-frequency (HF) radial mode forms an angle of $-5.9°$ with respect to the x-axis and the intrinsic trap depth is 10 meV.

In contrast to the electrodes needed for ion trapping, the 3D microwave conductor labeled MWM in Fig. 1 is extended to all three fabrication layers (L_1, V_1, L_2), enabling a complex microwave conductor design, which is discussed in more detail in Sect. 3. It is designed to produce an oscillating magnetic near-field gradient at the ion position suitable to drive motional sidebands (the key ingredient for multi-qubit gates) on the first-order field-independent qubit transition $|F = 2, m_{\text{F}} = +1\rangle \equiv |\uparrow\rangle \leftrightarrow |F = 1, m_{\text{F}} = +1\rangle \equiv |\downarrow\rangle$; of the electronic ground state $^2\text{S}_{1/2}$ with $\omega_0 \simeq 2\pi \times 1082.55\,\text{MHz}$ at $|B_0| \simeq 22.3\,\text{mT}$ (see Fig. 2 in Ref. [29] for a level scheme). Here, F refers to the total angular momentum F and m_{F} is the quantum number of its projection on B_0. The transition $|2, 0\rangle \leftrightarrow |1, 0\rangle$ has a frequency of $\omega_1 \simeq 2\pi \times 1397.56\,\text{MHz}$, this transition will be relevant in Sect. 4. The two additional microwave conductors labeled MWC_1 and MWC_2 produce an oscillating magnetic field amplitude at the ion position and can each be used to induce carrier transitions in the $^2\text{S}_{1/2}$ hyperfine manifold with $\Delta m_{\text{F}} \in \{0, \pm 1\}$. The grounded electrodes in the upper and bottom layer are connected via multiple interconnects in V_1, see Fig. 2. The number of interconnects is kept high to increase the conductivity between the layers.

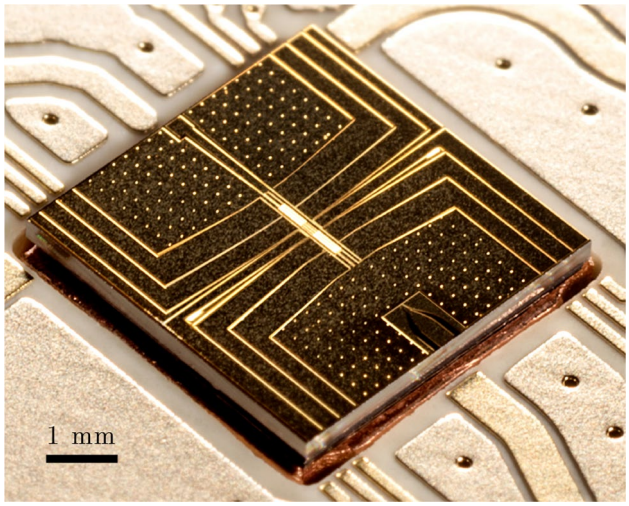

Fig. 2 Photograph of the presented multilayer trap surrounded by a custom printed circuit board before wirebonding. The feedline of MWM lies completely in L_1 and starts with a tapered bonding pad centered at the bottom right side. In the trap center the conductor is partly extended to L_2. Multiple vias in V_1 that interconnect ground electrodes in L_1 and L_2 are seen as bright dots

The trap is mounted and wire-bonded to a custom printed circuit board (PCB) placed in a room temperature vacuum system with pressure around 1×10^{-11} mbar. The PCB features $50\,\Omega$ coplanar microwave waveguides and RC filters ($f_c \simeq 194\,\text{kHz}$) for each DC trace. The Polyimide has a maximum long time baking temperature of 250 °C; more stringent constraints to the used maximum baking temperature in our setup come from in-vacuum microwave components. The trap is loaded by an ablation loading scheme [32] utilizing nanosecond pulses at 1064 nm to create a neutral ^{9}Be ablation plume above the trap center and a 235 nm cw laser beam for subsequent photoionization [33]. Doppler cooling is performed on the cycling transition $|^2\text{S}_{1/2}, 2, +2\rangle \leftrightarrow |^2P_{3/2}, m_{\text{J}} = +3/2, m_{\text{I}} = +3/2\rangle$ using σ^+ polarized light at $\simeq 313$ nm [34] propagating parallel to B_0, forming an angle of 30° with the z-axis.

3 Three-dimensional microwave conductor

3.1 Microwave conductor design

In the microwave near-field approach the Rabi rate of motional sideband transitions is proportional to the oscillating magnetic field gradient B' multiplied by the ion wavepacket size $x_{\mathrm{wp}} = \sqrt{\hbar/(2m\omega_{\mathrm{m}})}$ where m is the ion mass and ω_{m} the motional mode frequency ($x_{\mathrm{wp}} \approx 8\,\mathrm{nm}$ for $\omega_{\mathrm{m}} = \omega_{\mathrm{HF}} = 2\pi \times 9.33\,\mathrm{MHz}$). Whereas a high magnetic field gradient increases the motional coupling speed, any residual magnetic field amplitude B at the ion position can degrade the spin-motion coupling fidelity by off-resonant carrier excitations and/or uncompensated AC Zeeman shifts [23]. Consequently, the main design criterion of the microwave conductor MWM introduced in Fig. 1 is to produce a magnetic field configuration which maximizes B' at the ion position while keeping B as small as possible.

As shown in previous work, a single microwave conductor with a meander-like shape [35] can fulfill these field requirements by producing an oscillating magnetic quadrupole whose central field minimum is overlapped with the ion position at the RF null position. The minimum of the magnetic quadrupole is defined as the point where the amplitude of the magnetic field oscillation is minimized. Compared to a three-conductor design [24], the single meander-shaped conductor eliminates position fluctuations of the microwave magnetic field minimum due to phase and amplitude instabilities between the independently driven conductors of [24]. The meander-shaped MWM conductor design for the present trap is sketched in Fig. 1c (not to scale).

As can be seen, the feedline coming from the position labeled 'F' as well as the turning parts of the meander structure itself are completely in the bottom layer L_1, while MWM extends to all trap layers (L_1, V_1, L_2) along the three segments of length l_{m}. The turning points are moved away from the segments and placed underneath the ground electrodes of L_2. This will shield the connection segments from the ion(s). At the center of each segment, there is a pocket of length $l_{\mathrm{th}} = 200\,\mu\mathrm{m}$ and thickness h_2 which is filled with dielectric material during the fabrication process (see Fig. 1d for a cross-section through the pocket center labeled 'X' in Fig. 1c). At its end, the conductor is terminated to a ground patch in L_1 at the position labeled 'G'. The main advantages of the multilayer fabrication and the 3D meander-like conductor over equivalent single-layer trap designs are summarized in the following.

First, we demonstrate the possibility to bring in signals, such as the microwave signal for MWM, in the bottom layer L_1 and to connect them to trap electrodes controlling the ion only where needed. This avoids having to put these signal paths in the upper layer in L_2, where they would interfere with other trap electrodes, and is highly desirable for scalability. The same approach can also be applied to DC and RF electrodes.

Second, the fact that the different segments of the MWM conductor are only connected in the bottom layer L_1 allows us to independently choose the length of the RF electrode and the length l_{m} of the MWM segments. To achieve the desired overlap of the RF and microwave field minima, at least one RF electrode needs to be placed between MWM segments. For comparison, in the single-layer design of [29], this constrained the length of the RF electrodes to be less than the length of the MWM segments. It is, however, desirable to extend the RF electrodes much further along the axial direction to be able to transport ions between the entangling gate trap module presented here and other trap zones which would then be part of a surface-electrode ion trap array implementing the 'quantum CCD architecture' [12, 13].

Lastly, the implementation of the pocket inside the meander segments allows, in this configuration, to reduce the residual magnetic field B at the ion position by roughly one order of magnitude while keeping the gradient unchanged,[1] thus dramatically improving the field properties of MWM. No simple physical picture has been found for this decrease. In the discussed design this is possible only with a three-dimensional architecture of MWM, no other comparable magnetic field suppression was found by varying parameters which affect the arrangement of the electrodes in the trap plane. From numerical simulations we have investigated the influence of the pocket length l_{th} on both the thermal load and the residual field B. For the latter we have not found further suppression for values higher than $l_{\mathrm{th}} = 200\,\mu\mathrm{m}$. We perform resistive heating simulation to determine the thermal behaviour of MWM. This is of importance because the pocket is filled by polyimide which is a worse thermal conductor than gold. We simulate the effect of a DC current of 1A and measure the temperature at the position marked by X in Fig. 1c. As can be intuitively understood the heating is smaller for smaller sizes of l_{th}. A detailed discussion of the thermal load in the trap caused by operating the MWM conductor can be found in the Appendix.

3.2 Simulation model

Before starting any simulation of the MWM conductor design as discussed in the next paragraph, a decision about the desired ion-to-electrode distance d has to be made. The

[1] For a simulated input power of $1W$ we obtain $B = 7\,\mu\mathrm{T}$ without a thermal gap and $B = 0.8\,\mu\mathrm{T}$ with a thermal gap of length $l_{\mathrm{th}} = 200\,\mu\mathrm{m}$; the gradient $B' = 28\,\mathrm{T/m}$ remains unchanged in both cases.

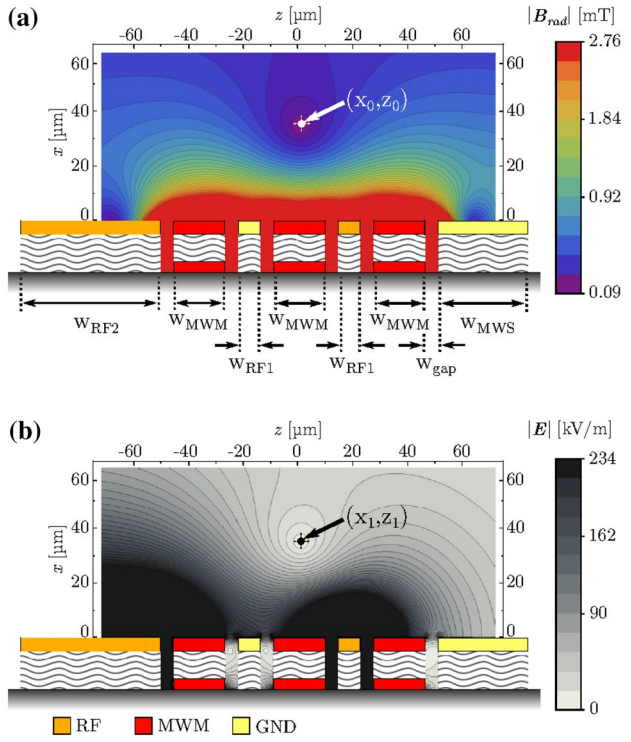

Fig. 3 **a** Simulated magnetic field pattern in the radial x–z plane produced by the microwave conductor MWM for 1 W of excitation. The dimensions indicated below are swept in simulations to overlap the magnetic field minimum at (x_0, z_0) with the ion position. **b** Simulated electric field pattern produced by the RF electrodes for 1 W of excitation. The ions are trapped in the RF null position at (x_1, z_1). For a perfect overlap of the two indicated positions, the gradient B' is maximized and the residual field B minimized at the ion(s) position

following points are particularly relevant here: on the one hand, the achievable gradient at the ion position scales as d^{-2}, consequently allowing high multi-qubit gate speeds for small distances. On the other hand, the motional heating rate $\dot{\bar{n}}$ should be expected to scale as d^{-4} [36], making the heating rate a significant error source during multi-qubit gates for small values of d. In our case, we consider an ion-to-electrode distance of $d \simeq 35\,\mu\text{m}$ to be a good compromise. This distance was selected to enhance the gradient as much as possible while still being at a distance which was known to work for other surface-electrode trap experiments.

The simulation model we employ to predict the resulting field configuration of a specific MWM conductor design around the qubit transition frequency ($\simeq 1$ GHz) is based on full-wave finite-element simulations using Ansys HFSS 17.2 software and addresses high-frequency effects like the skin-depth, eddy currents or couplings between neighbouring conductors. Its overall purpose is to find a MWM conductor design maximizing B' while minimizing B at the ion position by overlapping the magnetic field minimum at $(x_0, z_0)_{y=0}$ with the RF null position at $(x_1, z_1)_{y=0}$ as shown in Fig. 3.

All simulations are performed with a radiation boundary condition, assuming a gold conductivity at room temperature of 4.1×10^7 Siemens/m for all electrodes and conductors and include wirebonds as well as a section of the surrounding PCB. The nominal loss tangent of the polyimide is 0.002 at 1 kHz which is also the parameter used in the simulation, it is assumed constant at all frequencies to simplify the simulation. No strong change in results has been observed for the variation of this parameter. The input of MWM is simulated with a 50 Ω waveport while lumped ports are used for the inputs of the RF electrode as well as MWC_1 and MWC_2. The RF lumped port has a complex impedance of $100 + 1000i\,\Omega$, the carrier ones have an impedance of 50 Ω as each is connected to a 50 Ω waveguide. For the RF port we have assumed a mostly inductive behaviour reflected in the high reactance with some losses. A typical simulation workflow includes parametric sweeps of all the parameters given in Figs. 1c and 3a and can be structured in the following three steps.

In the first step, we only aim to find a starting geometry that coarsely fulfills the aforementioned field properties, namely an overlap of the magnetic field minimum and the RF null position about 35 µm above the trap. Here multiple electrode shapes, which differ from the one in Fig. 1c, can be tested. The location of the magnetic field minimum is found to depend most strongly on the spacing between the three MWM segments of length l_m, their width w_MWM, the width w_MWS of the left ground electrode and the width w_RF2 of RF2 (see Fig. 3a). Analogously, the RF null position depends on the spacing between RF1 and RF2 as well as their individual widths w_RF1 and w_RF2. For each iteration the RF null position is calculated using the gapless plane approximation [31] while the behaviour of the magnetic field minimum is inferred from multiple coarse parameter sweeps using the finite-element software. For this specific configuration the spacing between the three MWM segments is kept symmetric, therefore the distance between the segments is equal to two times the gap size w_gap plus w_{RF_1}. No additional residual field cancellation effect has been observed in breaking this symmetry.

Once a coarse geometry has been found, the second step is to perform fine sweeps over all parameters with priority to further minimize the residual field B (even at the cost of an increased mismatch between the RF null and the magnetic field minimum of up to 1–2 µm).

In the last step the likely present mismatch is addressed by changing only parameters with a known impact on the magnetic field minimum or the RF null position. For instance, w_RF2 and the width of the large ground electrode w_MWS can be used to minimize a minimum mismatch along the z-axis, while the upper layer's thickness h_3 mostly affects the magnetic field minimum along the x-axis. Due to increased sensitivity requirements, we determine the RF null position in

this last step using finite-element simulations with the correct frequency applied to the RF electrode. In our simulation model we consider a final mismach between $(x_0, z_0)_{y=0}$ and $(x_1, z_1)_{y=0}$ of smaller than 100 nm acceptable.

3.3 Couplings between conductors

The presence of multiple conductors constitutes a complex problem which the FEM simulation model cannot fully account for due to its limited size. The issue arises because of the inductive and resistive coupling between electrodes and the possibility of back reflections of the induced currents in those electrodes. It affects mostly the field configuration created by MWM since any back reflected current can change the magnetic near-field configuration and hence can disturb the overlap with the ion's position. Since RF and DC are floating electrodes, the effect is negligible. On the other hand, the coupling to the microwave conductors MWC_1 and MWC_2, see Fig. 1, can cause notable changes of the minimum in MWM magnetic field that depends on coupling parameters and the transmission line of the other conductor [29]. This can be explained in the following way. The signal in MWM produces currents in MWC_1 and MWC_2 which propagate along the transmission line of each electrode. Some fraction of these induced currents is backreflected at every impedance variation or imperfection in the transmission line, each with a certain phase depending on the transmission line properties. Once the sum of reflected currents has traveled back to the original electrode, it generates magnetic fields which have to be added to the magnetic field initially produced by MWM, causing an effective shift of the magnetic quadrupole minimum position. The simulation model used here includes only a section of the PCB, so any reflection which does not take place there or on the trap is not accounted for. To evaluate the impact of these reflections we consider a single perfect backreflection from the transmission line which reflects all the current sent to it. The effect is implemented by applying a signal to the corresponding lumped port exactly equal to the power coupled into it by MWM. This constitutes a worst-case scenario since the backreflected current can not be higher than the one originally coupled into an electrode. To understand the possible variation range it is necessary to analyze what happens for different phases of the backreflection. The blue markers (circles for z-axis, squares for x-axis) in Fig. 4 show the position of the magnetic field minimum as a function of the phase of the backreflected current in MWC_2 for a coupling of − 27.8 dB at an input power of 1W in MWM (the effect of MWC_1 is neglected here for clarity, but would just be added to the field of MWC_2). The change of the residual magnetic field B at the magnetic minimum position is shown by the orange markers in Fig. 4. Even though for some phases the additional field further suppresses the overall residual field, for most phases the total value of B increases.

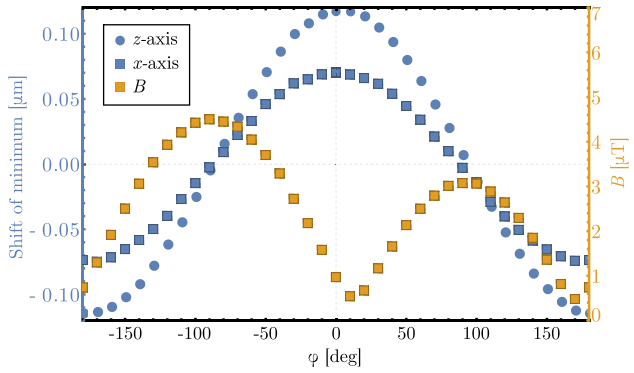

Fig. 4 Effect of the − 27.8 dB coupling between the MWM and MWC_2 conductors, at 1W input power in MWM, for different phases of the backreflection on the transmission line attached to MWC_2. Blue markers: effect on the magnetic field minimum position of the quadrupole produced by MWM. Orange markers: effect on the total residual magnetic field B due to additional magnetic fields produced by backreflections in MWC_2

In the previous trap design mentioned above, the coupling between MWM and the neighbouring microwave conductor, given by the S_{21} parameter, was simulated to be − 9 dB. The resulting position changes of the magnetic field minimum were up to 3 µm and made it necessary to minimize the effect by engineering the transmission line appropriately. Since a reason of the strong coupling was found to be the immediate proximity of both involved conductors (compare Fig. 1 in Ref. [29]), we took special care in the conductor layout of MWC_1 and MWC_2 in the present multilayer trap. Here, the two microwave conductors are routed around the central DC electrode on each side which minimizes the length of closest proximity and allows a higher spatial separation of MWM and MWC_1 by introducing an additional ground electrode of width w_{MWS} (see Fig. 3a). Following this approach, the coupling from MWM to MWC_1 and MWC_2 could be reduced by roughly 19 dB compared to the previous trap design to simulated values of − 27.9 dB and − 27.8 dB, respectively. MWC_1 and MWC_2 are connected through wirebonds to the filterboard and are grounded at the other end via interconnects in V_1, which provide connection to a ground electrode in L_1. With the described configuration the coupling could be reduced to a level where its effect can be neglected in the fields overlap predictions, so no further increase of isolation was investigated.

4 Experimental data

To measure the magnetic near-field pattern produced by MWM and compare it to our simulation model, we measure the induced AC Zeeman energy shift on suitable transitions in the atomic hyperfine structure for different ion positions in

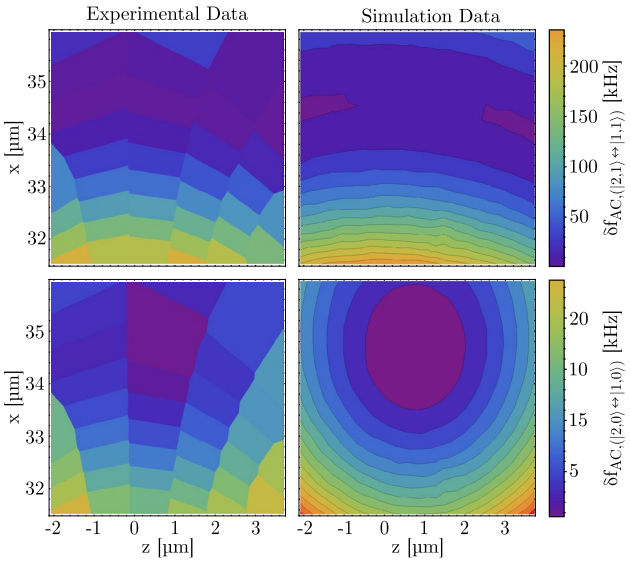

Fig. 5 Comparison of experimentally measured (left column) and simulated (right column) absolute AC Zeeman shifts induced by the resulting field of the microwave conductor MWM. The upper row shows the data for the qubit transition $|2,+1\rangle \leftrightarrow |1,+1\rangle$ while the bottom row shows the one for the $|2,0\rangle \leftrightarrow |1,0\rangle$ transition. The position of the experimental data is relative to the position of the RF null which, in the coordinate system of Fig. 1, appears nominally at $(x_1, z_1) = (0.75, 34.55)$ µm. See main text for details

the radial plane. The exact procedure is detailed in Ref. [29] and based on previous work [37]. The basic idea is to off-resonantly excite MWM between two $\frac{\pi}{2}$ pulses of a standard Ramsey experiment and to measure the induced AC Zeeman shift on the transitions $|F = 2, m_F = +1\rangle \leftrightarrow |1,+1\rangle$ (qubit) and $|2,0\rangle \leftrightarrow |1,0\rangle$ of the electronic ground state $^2S_{1/2}$ by fitting the observed phase accumulations due to the induced transition frequency change. The MWM conductor is excited with a frequency of $\omega \simeq 2\pi \times 1092.55$ MHz. While the shift on the qubit transition is mainly induced by the π-component of the excitation field, the shift on the other transition is also induced by its σ-components. Moving the ion along the x- and z-direction by applying DC potentials allows to map the AC Zeeman energy shifts in the radial plane and to infer the resulting magnetic field distribution produced by MWM.

Figure 5 shows the absolute values of measured AC Zeeman shifts on the qubit transition $|2,+1\rangle \leftrightarrow |1,+1\rangle$ (upper row) and the $|2,0\rangle \leftrightarrow |1,0\rangle$ transition (lower row) as a function of x and z around the calculated RF null position at $(x_1, z_1) = (0.75, 34.55)$ µm. While the left column displays experimentally measured data, the right column shows AC Zeeman shifts calculated from the magnetic fields obtained by the simulation model introduced in Sect. 3.2. The AC Zeeman shifts of the experimental data and the magnetic field of the simulations are each fitted in a single least squares fit using the 2D quadrupole model of Eq. (2) in Ref. [29] with B, B', α, β, ψ, x_0 and z_0 as fit parameters. Here, B is the residual field in the minimum, B' the magnetic field gradient, α the rotation angle of the residual field, β the rotation angle of the gradient in the quadrupole, ψ the relative angle between real and imaginary part and (x_0, z_0) the magnetic field minimum position. Since the residual field in the minimum of the experimental data was too low to be fitted accurately, B and α were manually set to zero in the fit procedure. In consequence, only an upper bound for B can be given. A comparison of the fit parameters determined in the experiment and by simulations can be found in Table 1. The upper bound for B is obtained by introducing it again in the fitted model as a parameter and by calculating the B required to obtain the lowest measured AC Zeeman shift on the $|2,0\rangle \leftrightarrow |1,0\rangle$ transition given by 551 Hz. For the calculation we assume that the measured shift is located at the absolute minimum. The value for α is set to 0° since it minimizes the coupling, consequently giving us an upper boundary for the residual field B of ~ 34 µT. We note that a smaller boundary could possibly be achieved by increasing the spatial resolution of the measurement.

Table 1 Comparison of the 2D quadrupole parameters determined by simulations and by experimental measurements using a single $^9Be^+$ ion (Fig. 5)

Parameter (units)	Simulation	Experiment
B (µT)	1.47	$\lesssim 34$
B' (T/m)	54.8	54.8 (1.2)
α (°)	40.8	–
β (°)	87.3	86.8 (1.7)
ψ [°]	0.1	1.5 (7.6)
x_0 (µm)	34.72	34.62 (0.05)
z_0 (µm)	0.73	0.6 (0.7)

To induce higher frequency shifts, the data in the lower row were taken and simulated at a nominally 3 dB higher power level than the data set in the upper row. For reference, the data in the upper row in Fig. 5 correspond to $B' \approx 54.8$ T/m obtained with 1.9 W of input power to the system.

Complementary information can be obtained by analyzing the structure in terms of a microwave circuit. Our full-wave numerical simulations provide the S parameters of the structure for all implemented ports. Using a wafer prober, we can compare this data to actual measurements on fabricated devices (see Fig. 6). Within the frequency regime of interest (around 1 GHz), simulations and experimental data are in good agreement. The deviations for higher frequencies are not relevant for our experiments and can be explained by subtleties of the wafer prober measurements at higher frequencies, where the exact method of contacting the prober to the sample becomes more relevant and slightly deviates from the scenario employed in the simulations. Note that here

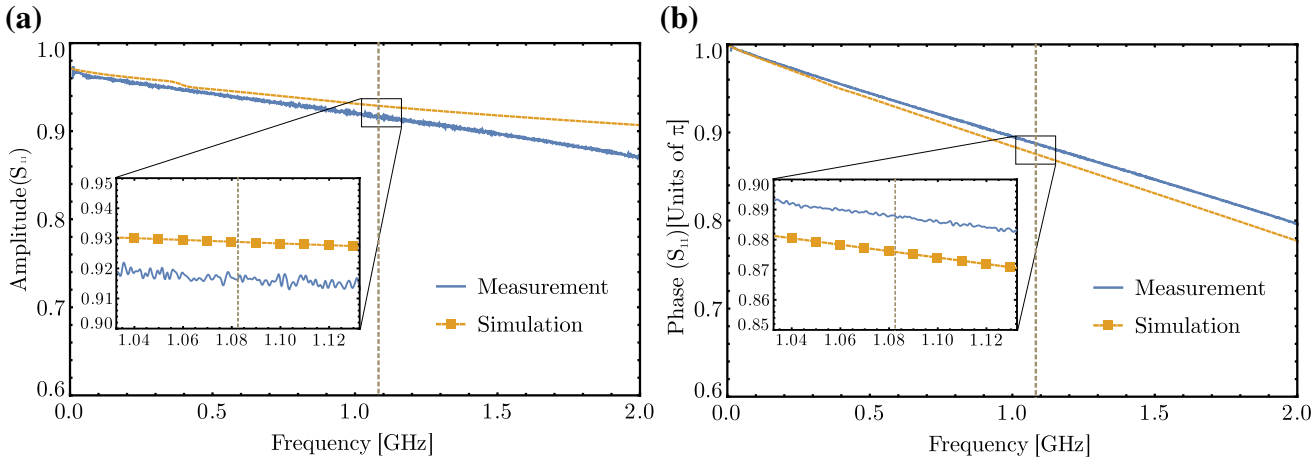

Fig. 6 Comparison of MWM's measured and simulated S_{11} parameter in amplitude (**a**) and phase (**b**) as a function of frequency. Measurement in blue simulations in dashed orange. The frequency of the qubit transition is highlighted by the dashed grey line. At that frequency we measure a reflected amplitude of 0.916 while from simulation we expect 0.927. The inset show a more detailed plot around the qubit frequency

we re-run the field simulations with all electrodes floating except for MWM and without the filterboard to mimic the conditions of the measurement.

5 Summary and conclusion

We have presented a multilayer surface-electrode ion trap based on a novel fabrication technique [30]. The trap design features two microwave conductors (MWC_1, MWC_2) to produce a high field amplitude for driving single-qubit gates and one 3D meander-like microwave conductor (MWM) to produce an oscillating near-field gradient with minimal residual field for driving multi-qubit gates around 1 GHz. Besides a general trap characterization, we give detailed information about the employed full-wave simulation model and the design criteria of the microwave conductors to produce the desired field configuration. The resulting field pattern of MWM was experimentally measured in a Ramsey-type single-ion experiment and subsequently analyzed in a least square model fit. The extracted 2D quadrupole properties of the experimental data were found to be in good agreement with the expected values from our simulation model close to the ion position. The 3D microwave conductor extends to all three fabrication layers and allows an advanced version of a meander-shaped microwave conductor design when compared to a corresponding single-layer design. In the demonstrated multilayer trap, the 3D conductor enables an improved field pattern for multi-qubit gates by further suppressing the residual magnetic field B at the ion's position. For comparison, the lowest residual field at a gradient of 54.8 T/m in this trap was determined to be $\sim 34\,\mu$T while the residual field in a previous single-layer design [29] was calculated to be at least a factor of 14 larger (447 μT) when scaled to the same gradient. The resulting AC Zeeman shift can cause significant error contributions during multi-qubit gates [23] and depends on the residual field's magnitude and polarization. Analyzing the data sets of both traps, we found the absolute lowest measured AC Zeeman shift for the qubit transition in the multilayer trap (697 Hz) to be almost three orders of magnitude smaller than in the previous single-layer trap (505 kHz) when scaled to the same gradient.

Assuming the residual field of $\lesssim 34\,\mu$T to be perfectly π -polarized we expect at the quadrupole minimum an on-resonance Carrier pi-time longer than 1.5 μs for the qubit transition. Based on the measured values of the gradient and the HF radial mode 2, we calculate the minimum time for an entangling gate operation based on the Mølmer–Sørensen interaction [38, 39] to be $\approx 120\,\mu$s. Future work will focus on achieving control over the motion at the single-quantum level, measure heating rates and employ such devices for the implementation of entangling gates and effective spin–spin interactions.

Acknowledgements We acknowledge support by the PTB cleanroom facility team and funding from PTB, LUH, the clusters of excellence QUEST and Quantum Frontiers, NTH (project number 2.2.11), the EU QT Flagship project MicroQC (grant no 820314) and DFG through SFB 1227 DQ-*mat*, project A01.

Appendix: Joule heating

When microwave currents are applied to the trap through a conductor with finite conductivity, electric energy is converted into heat through resistive losses. Excessive resistive heating in the trap might lead to a degeneration of its

performance or, in extreme cases, to an irreversible damage of the conductor. This is especially critical for an ion trap with multiple layers as discussed here, since current-carrying conductors defined around the geometric trap center have relatively narrow lateral dimensions, i.e., poor thermal contact to the substrate.

To include thermal effects caused by applying short microwave pulses with high power to the MWM conductor imitating real experimental conditions, one would need to numerically solve a complex system, including the whole chip geometry and inductive heating caused on neighbouring electrodes. However, it is also possible to gain insight into thermal effects in the trap design using a simplified model in which a constant DC current is applied to MWM. As already introduced in Sect. 3.1, we make use of a pocket in the three segments of MWM with length l_m to further decrease the residual magnetic field B at the ion's position. Since we are interested in a compromise between a sufficiently low heat load and low B, the simplified DC power model still reveals the qualitative behaviour of the system.

In the experiment we apply 1.9W to the MWM structure corresponding to c.a. 160mW of power not reflected by the trap given the measured S-parameter, see caption of Fig. 6. To better understand the limits of thermal dissipation we perform simulations on a DC current in a similar structure. We use a current of 1A which corresponds to a dissipated power of 200 mW since the nominal geometry considered in the model, $l_{th} = 200\,\mu m$, has a resistance of $0.2\,\Omega$.

The numerical simulations are performed using the AC/DC and heat transfer modules of COMSOL 4.3, assuming a DC current of 1 A applied to MWM, supported on an Si_3N_4 /Si substrate of 1.5 mm × 1.5 mm. We perform a parametric sweep of l_{th} along the y-axis. As a result of the fabrication process, the pockets are filled with a dielectric material, which we included in the model assuming a thermal conductivity of $0.15\,W\,m^{-1}\,K$. The electrical and thermal properties of Au (conductor material) and Si_3N_4 (wafer material) are taken from the built-in materials data library. While the room temperature ($T_0 = 293.15\,K$) reference is defined to be at the backside of the chip trap, the temperature of MWM is monitored on the surface of L_2 at the geometric trap center marked as 'X' in Fig. 1c. At this position the heat load is maximal because each segment of MWM vertically splits into two parts of thickness h_1 and h_3, respectively, separated by the pocket of thickness h_2 in the interconnect layer V_1 filled with the dielectric material (see inset Fig. 1c). Naturally, at this point the heat will be poorly transported along the x-axis perpendicular to the trap.

Figure 7 shows the resulting temperature change with respect to room temperature for different values of l_{th} as a function of time. For $l_{th} = 200\,\mu m$, the system reaches a steady state after 0.6 ms, increasing its temperature by 17 K. As shorter values for l_{th} decrease the temperature change, but increase B at the ion position (see Sect. 3.1), we found $l_{th} = 200\,\mu m$ to be the best compromise as illustrated in Fig. 8.

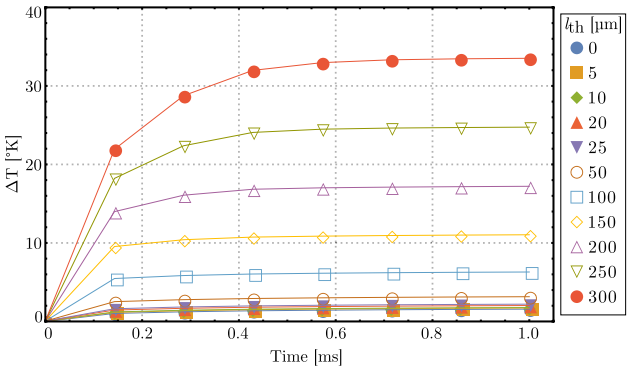

Fig. 7 Results of the simplified finite-element model in which a constant current of 1A is applied to MWM. The plots show the temperature increase in the center of MWM as a function of excitation time. Different colors indicate a different pocket length l_{th}

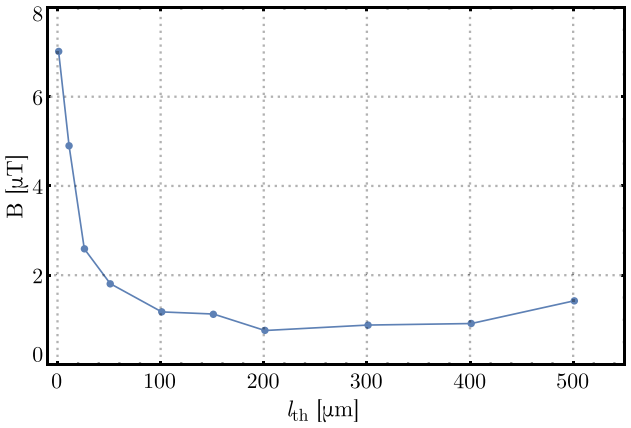

Fig. 8 Residual magnetic field B for different pocket lengths l_{th} in the segments of the MWM conductor. At about $l_{th} = 200\,\mu m$ there is no further decrease in the residual field. The values were obtained by performing FEM simulations using our simulation model discussed in Sect. 3.2

References

1. J.I. Cirac, P. Zoller, Phys. Rev. Lett. **74**, 4091 (1995)
2. R. Blatt, D. Wineland, Nature **453**, 1008 (2008)
3. I.M. Georgescu, S. Ashhab, F. Nori, Rev. Mod. Phys. **86**, 153 (2014)
4. A. Bermudez, X. Xu, R. Nigmatullin, J. O'Gorman, V. Negnevitsky, P. Schindler, T. Monz, U. Poschinger, C. Hempel, J. Home, F. Schmidt-Kaler, M. Biercuk, R. Blatt, S. Benjamin, M. Müller, Phys. Rev. X **7**, 041061 (2017)
5. A. Montanaro, npj Quantum Inf. **2**, 15023 (2016)
6. S. Debnath, N.M. Linke, C. Figgatt, K.A. Landsman, K. Wright, C. Monroe, Nature **536**, 63 (2016)

7. T. Monz, D. Nigg, E.A. Martinez, M.F. Brandl, P. Schindler, R. Rines, S. XWang, I.L. Chuang, R. Blatt, Science **351**, 1068 (2016)
8. J. Zhang, G. Pagano, P.W. Hess, A. Kyprianidis, P. Becker, H. Kaplan, A.V. Gorshkov, Z.-X. Gong, C. Monroe, Nature **551**, 601 (2017)
9. P. Jurcevic, H. Shen, P. Hauke, C. Maier, T. Brydges, C. Hempel, B. Lanyon, M. Heyl, R. Blatt, C. Roos, Phys. Rev. Lett. **119**, 080501 (2017)
10. C. Monroe, J. Kim, Science **339**, 1164 (2013)
11. S. Seidelin, J. Chiaverini, R. Reichle, J.J. Bollinger, D. Leibfried, J. Britton, J.H. Wesenberg, R.B. Blakestad, R.J. Epstein, D.B. Hume, W.M. Itano, J.D. Jost, C. Langer, R. Ozeri, N. Shiga, D.J. Wineland, Phys. Rev. Lett. **96**, 253003 (2006)
12. D.J. Wineland, C.R. Monroe, W.M. Itano, D. Leibfried, B.E. King, D.M. Meekhof, J. Res. NIST **103**, 259 (1998)
13. D. Kielpinski, C. Monroe, D.J. Wineland, Nature **417**, 709 (2002)
14. J.M. Amini, H. Uys, J.H. Wesenberg, S. Seidelin, J. Britton, J.J. Bollinger, D. Leibfried, C. Ospelkaus, A.P. VanDevender, D.J. Wineland, New J. Phys. **12**, 033031 (2010)
15. D.P.L.A. Craik, N.M. Linke, T.P. Harty, C.J. Ballance, D.M. Lucas, A.M. Steane, D.T.C. Allcock, Appl. Phys. B **114**, 3 (2014)
16. N.D. Guise, S.D. Fallek, K.E. Stevens, K.R. Brown, C. Volin, A.W. Harter, J.M. Amini, R.E. Higashi, S.T. Lu, H.M. Chanhvongsak, T.A. Nguyen, M.S. Marcus, T.R. Ohnstein, D.W. Youngner, J. Appl. Phys. **117**, 174901 (2015)
17. P.L.W. Maunz, Technical report. Sandia National Lab. SAND-2016-0796R (2016)
18. C. Ospelkaus, C.E. Langer, J.M. Amini, K.R. Brown, D. Leibfried, D.J. Wineland, Phys. Rev. Lett. **101**, 090502 (2008)
19. F. Mintert, C. Wunderlich, Phys. Rev. Lett. **87**, 257904 (2001)
20. J. Gaebler, T. Tan, Y. Lin, Y. Wan, R. Bowler, A. Keith, S. Glancy, K. Coakley, E. Knill, D. Leibfried, D.J. Wineland, Phys. Rev. Lett. **117**, 060505 (2016)
21. C. Ballance, T. Harty, N. Linke, M. Sepiol, D. Lucas, Phys. Rev. Lett. **117**, 060504 (2016)
22. M. Johanning, A. Braun, N. Timoney, V. Elman, W. Neuhauser, C. Wunderlich, Phys. Rev. Lett. **102**, 073004 (2009)
23. T. Harty, M. Sepiol, D. Allcock, C. Ballance, J. Tarlton, D. Lucas, Phys. Rev. Lett. **117**, 140501 (2016)
24. C. Ospelkaus, U. Warring, Y. Colombe, K.R. Brown, J.M. Amini, D. Leibfried, D.J. Wineland, Nature **476**, 181 (2011)
25. A. Khromova, C. Piltz, B. Scharfenberger, T.F. Gloger, M. Johanning, A.F. Varón, C. Wunderlich, Phys. Rev. Lett. **108**, 220502 (2012)
26. S. Weidt, J. Randall, S. Webster, K. Lake, A. Webb, I. Cohen, T. Navickas, B. Lekitsch, A. Retzker, W. Hensinger, Phys. Rev. Lett. **117**, 220501 (2016)
27. R. Ozeri, W.M. Itano, R.B. Blakestad, J. Britton, J. Chiaverini, J.D. Jost, C. Langer, D. Leibfried, R. Reichle, S. Seidelin, J.H. Wesenberg, D.J. Wineland, Phys. Rev. A **75**, 042329 (2007)
28. T. Harty, D. Allcock, C. Ballance, L. Guidoni, H. Janacek, N. Linke, D. Stacey, D. Lucas, Phys. Rev. Lett. **113**, 220501 (2014)
29. M. Wahnschaffe, H. Hahn, G. Zarantonello, T. Dubielzig, S. Grondkowski, A. Bautista-Salvador, M. Kohnen, C. Ospelkaus, Appl. Phys. Lett. **110**, 034103 (2017)
30. A. Bautista-Salvador, G. Zarantonello, H. Hahn, A. Preciado-Grijalva, J. Morgner, M. Wahnschaffe, C. Ospelkaus, New Phys. J. **21**, 043011 (2019)
31. J.H. Wesenberg, Phys. Rev. A **78**, 063410 (2008)
32. D.R. Leibrandt, R.J. Clark, J. Labaziewicz, P. Antohi, W. Bakr, K.R. Brown, I.L. Chuang, Phys. Rev. A **76**, 055403 (2007)
33. H.-Y. Lo, J. Alonso, D. Kienzler, B.C. Keitch, LEd Clercq, V. Negnevitsky, J.P. Home, Appl. Phys. B **114**, 17 (2013)
34. A.C. Wilson, C. Ospelkaus, A.P. VanDevender, J.A. Mlynek, K.R. Brown, D. Leibfried, D.J. Wineland, Appl. Phys. B **105**, 741 (2011)
35. M. Carsjens, M. Kohnen, T. Dubielzig, C. Ospelkaus, Appl. Phys. B **114**, 243 (2014)
36. Q.A. Turchette, D. Kielpinski, B.E. King, D. Leibfried, D.M. Meekhof, C.J. Myatt, M.A. Rowe, C.A. Sackett, C.S. Wood, W.M. Itano, C. Monroe, D.J. Wineland, Phys. Rev. A **61**, 063418 (2000)
37. U. Warring, C. Ospelkaus, Y. Colombe, R. Jördens, D. Leibfried, D.J. Wineland, Phys. Rev. A **87**, 013437 (2013)
38. A. Sørensen, K. Mølmer, Phys. Rev. Lett. **82**, 1971 (1999)
39. K. Mølmer, A. Sørensen, Phys. Rev. Lett. **82**, 1835 (1999)

Chapter 4

Microwave-driven quantum operations

In the previous chapter we have discussed the capability to fabricate, simulate and operate multi level surface-electrode ion traps. This gives the basic building block for the scalable QCCD architecture. In this chapter we discuss the theory of near-field microwaves and their application for entangled state generation using the Mølmer-Sørensen interaction. This results provides the last of the DiVincenzo criteria: a 'universal' set of quantum gates. The experimental implementation of the gate in a single-layer trap has been published in the peer-reviewed article **P4** [HZS+19] reported in Sec. 4.8 at the end of this chapter. Additional information can be found in [Osp16, Hah19].

4.1 Motivation

Microwave-driven quantum operations [MW01, OLA+08] are an alternative approach to laser-based operations for transitions in the appropriate frequency range, typically hyperfine or Zeeman transitions. The use of microwaves for the purpose of quantum computing has been first implemented successfully for Nuclear Magnetic Resonance (NMR) experiments to implement small-scale quantum algorithms [CVZ+98]. Atomic species used so far for microwave based experiments with trapped ion include for example: $^{9}Be^{+}$, $^{25}Mg^{+}$, $^{43}Ca^{+}$ and

$^{171}Yb^{+}$. All of these species offer suitable hyperfine qubit transitions in the few GHz range. Microwave-driven operations have the advantage of being directly resonant with the transition addressed. The use of directly resonant fields avoids off-resonant scattering [OLJ+05, OIB+07], which is one of the main issues typical of Raman laser transitions [WMI+98a, LBMW03]. In a Raman laser system are used two lasers beams which frequency differs by the qubit transition of interest. By coupling through a virtual excited level, it is possible to perform a coherent transition from one qubit state to the other. The finite frequency difference between the virtual level and the real one leads to a non-zero probability to scatter photons off-resonantly. This effect can be reduced with more laser power and a larger detuning from the real level, but will always be present and therefore contribute to an error. Current state of the art laser-driven two-qubit entangling gates are limited by scattering errors due to the limited laser power available [GTL+16]. For microwave-based two-qubit entangling gates no spontaneous decay occurs as the transition is driven directly. It is of interest to note that also hybrid microwave-laser approaches have been proposed [LBP13].

The first step to achieve in order to perform entanglement operations, is to produce a spin-motional coupling by producing a magnetic field with a gradient. As already explained in section 2.2, the natural oscillation of optical wavelength radiation is enough to produce such a gradient, while it is more challenging for microwave radiation. Currently, three different gradient schemes for microwave transitions have been identified to produce spin-motional coupling. The first one is the static gradient scheme [MW01] which makes use of a static magnetic field with a linear gradient. The scheme on which this thesis work is based is the near-qubit-frequency oscillating gradient scheme [OLA+08] where the magnetic field with a gradient oscillates at a frequency close to the qubit transition, generally in the GHz range for hyperfine transitions. A more recent scheme is the near-motional-frequency oscillating gradient [SSB+19] where the magnetic field gradient oscillates at a frequency close to the motional frequency of the trapped ion, generally in the MHz range.

4.2 Microwave operation

In this section and the next, we will follow the derivation of ref. [Hah19] to discuss the theory behind the use of microwave near-fields. Oscillating magnetic fields allow to couple two energy levels through the magnetic dipole interaction. The interaction Hamiltonian is:

$$H_{\mathrm{i}} = \boldsymbol{\mu} \cdot \boldsymbol{B}(\boldsymbol{x}, t) \quad , \tag{4.1}$$

where $\boldsymbol{\mu}$ is the magnetic moment of the selected transition and $\boldsymbol{B}$ is the magnetic field, oscillating at frequency ω with phase ϕ, which can be written as

$$\boldsymbol{B}(\boldsymbol{x}, t) = (B_x + B_y + B_z)\cos(\omega t + \phi) \quad . \tag{4.2}$$

Here B_i with $i \in \{x, y, z\}$ are the different components of $\boldsymbol{B}$. In the works discussed in this thesis, all experiments have been performed on a first-order field-independent qubit transition in $^9\mathrm{Be}^+$ ions at an external magnetic field of 223 G. This is a transition with $\Delta m_F = 0$, i.e. a π-transition, for which the interaction Hamiltonian, assuming a quantization axis aligned along the direction z, can be written as:

$$H_{\mathrm{i}} = -\left(\mu_{\parallel}\sigma^x + \mu_z\sigma^z + \mu_{id}\mathbb{1}\right) B_z \cos\left(\omega t + \phi\right). \tag{4.3}$$

Here σ^i with $i \in \{x, y, z\}$ are the Pauli operators. The term with σ^z represents an energy shift of opposite sign between the two qubit states. The term with the identity operator $\mathbb{1}$ represents an energy shift in the same direction of the involved states. In a $\Delta m_F = \pm 1$ transition, i.e. a σ-transition, the magnetic moment $\boldsymbol{\mu}$ will be different and therefore H_{i} will also be different.

We assume that the ions can be described as a two-level interaction free Hamiltonian H_{sys} with H_{int} to indicate the internal electronic levels of N ions and H_m for the motional term of the ions in the harmonic potential. They can be written as:

$$H_{\mathrm{sys}} = H_{\mathrm{int}} + H_{\mathrm{m}} \tag{4.4}$$

$$H_{\mathrm{int}} = \hbar\omega_0 \sum_{j=1}^{N} \sigma_j^z \tag{4.5}$$

$$H_{\mathrm{m}} = \hbar\omega_r a^\dagger a \quad , \tag{4.6}$$

where in the motional term the ground state energy has been neglected. The frequency ω_0 indicates the transition frequency between the two qubit levels, ω_r

the motional mode frequency of the harmonic oscillator with ladder operators a and $a^\dagger$. Generally for N ions there are $3N$ motional modes, in the motional term H_m only one mode has been considered. More details can be found in [Jam98]. The interaction term, Eq. 4.3, can then be written as:

$$H_\mathrm{i} = -\mu_\parallel \sigma^x B_z(\boldsymbol{x}) \cos(\omega t + \phi) \quad , \tag{4.7}$$

where $B_z(\boldsymbol{x})$ denotes a spatial dependence on the B_z component of the magnetic field. In the following, we consider the coordinate x to be in the harmonic oscillator direction for simplicity. Eq. 4.7 can be expanded with the Taylor series expansion around the equilibrium position of the harmonic oscillator:

$$H_i = \mu_\parallel (\sigma^+ + \sigma^-) \cos(\omega t + \phi) \sum_k \frac{1}{k!} \left.\frac{\partial^k B(x)}{\partial x^k}\right|_{x=0} q_0^k (a + a^\dagger)^k \quad , \tag{4.8}$$

where the position operator x has been written in terms of the ladder operators $x = q_0(a + a^\dagger)$ while the Pauli operator σ^x has been written in terms of its ladder operators $\sigma^x = (\sigma^+ + \sigma^-)$. The ground state wavepacket extent q_0 is equal to $\sqrt{\hbar/(2m\omega_r)}$. It is useful to write H_i in the interaction picture of H_sys:

$$H_\mathrm{I} = \frac{\hbar}{2} \left(e^{i(\omega t+\phi)} + e^{-i(\omega t+\phi)}\right) \left(\sigma^+ e^{i\omega_0 t} + \sigma^- e^{-i\omega_0 t}\right) \sum_k \frac{\Omega_k}{k!} (e^{-i\omega_r t} a + e^{i\omega_r t} a^\dagger)^k \quad ,$$

where Ω_k is defined as: $-\frac{\mu_\parallel}{\hbar} \frac{\partial^k B(x)}{\partial x^k}|_{x=0} (q_0)^k$. The development is done under the rotating wave approximation. The term with $k = 0$ now describes the carrier operation, with Rabi rate Ω_0, which drives transitions between the two qubit states with a magnetic field oscillating at frequency $\omega = \omega_0$. The term with $k = 1$ describes the sideband transitions, with Rabi rate Ω_1, both the motion adding (blue sideband) at $\omega = \omega_0 + \omega_r$ and motion substracting one (red sideband) at $\omega = \omega_0 - \omega_r$.

4.3 Mølmer-Sørensen entangling gate

There are multiple schemes which allow two-qubit entangling gate operations as required by the DiVincenzo criteria [CZ95, LDM+03, KMJ+11]. The scheme chosen for this work has been developed by Mølmer and Sørensen [MS99, SM99, SdMFZ99, MSJ00] two decades ago. In a specific eigenbasis, this scheme can be understood as a geometric phase gate considering that only specific states

can gain a phase, while the others remain unaffected. The process makes use of a transient motional-spin excitation but does not require the ions to be in the motional ground state as required by some similar protocols, for example [CZ95]. This feature simplifies the experimental operations, making perfect ground state cooling not a mandatory requirement.

For the Mølmer and Sørensen interaction, the entire dynamics of the ions system is driven by a bichromatic field: two magnetic fields are applied at the same time, one at a frequency of $\omega_B = \omega_0 + \omega_r + \delta$ and the other one at $\omega_R = \omega_0 - \omega_r - \delta$. A schematic of the levels and the fields involved for the two-ion case is shown in Fig. 4.1, where $|n\rangle$ represents the ion motional state. These microwave fields effectively drive sideband transitions with the addition of a symmetric frequency detuning δ. The interaction Hamiltonian for 2 ions on a single motional mode can then be written as:

$$H_{\mathrm{MS}} = \frac{\hbar}{2}\Omega_{\mathrm{MS}} \sum_{j=1}^{2} \left(\sigma_j^+ + \sigma_j^-\right)\left(a e^{i\delta t} + a^\dagger e^{-i\delta t}\right) \quad , \tag{4.9}$$

where Ω_{MS} is the gate Rabi rate. This rate depends on the single-ion sideband Rabi rate Ω_1 and on the motional mode amplitude. The latter depends on the number of ions present, the specific motional mode addressed and the ion position in the Coulomb crystal [Jam98].

While the interaction described by the Hamiltonian H_{MS} is active, the system undergoes a specific time-evolution. When the time for which the interaction is applied, τ, respects the constraint $\tau = \frac{2\pi K}{\delta}$ and the symmetric detuning is given by $\delta = 2\Omega_{\mathrm{MS}}\sqrt{K}$, the dynamics generates entangled states. The integer K identifies the number of loops performed in phase space by the selected motional mode. The discussion of these loops can be found later in Sec. 5.1 since they are fundamental for understanding the amplitude modulated version of the entangling gate. The propagator for such a time evolution is independent, in absence of errors, of the ions' initial motional state and results in some spin eigenstates[5] of the σ^x operator acquiring an additional phase of $\pi/2$. As implemented experimentally in this work, the starting state $|\uparrow\uparrow\rangle$ evolves, due to this additional phases, into the maximally entangled Bell state $|\Psi\rangle = \left(|\uparrow\uparrow\rangle + i\,|\downarrow\downarrow\rangle\right)/\sqrt{2}$.

[5] specifically $|+-\rangle$ and $|-+\rangle$ for the two ion case, see [Hah19] for details.

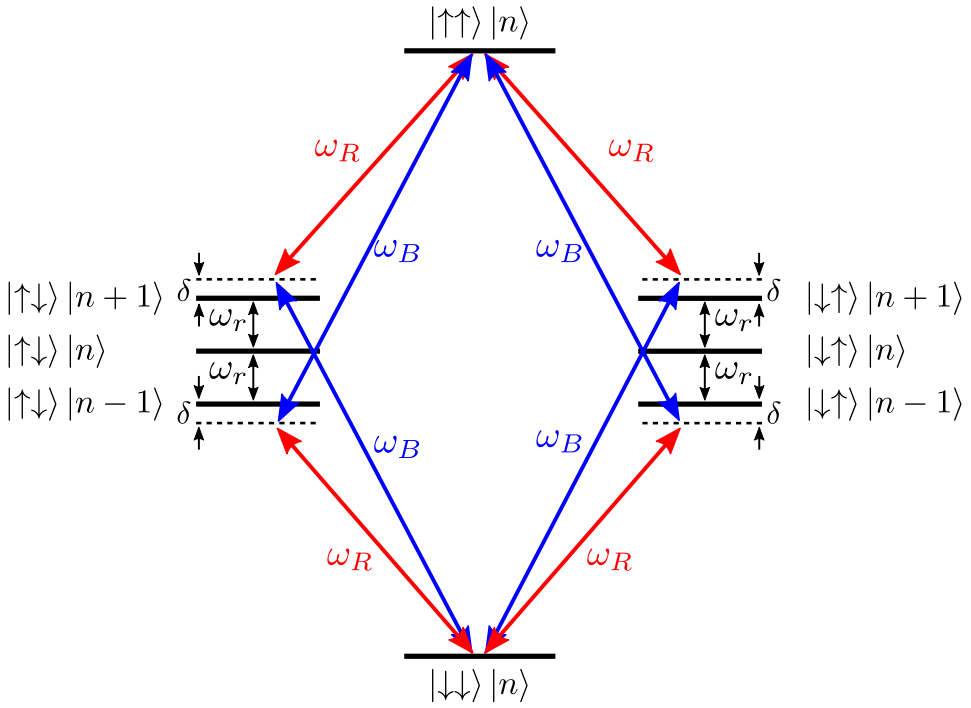

Figure 4.1: Scheme shows the possible states, transitions and fields in the two-ion case that are involved in the Mølmer-Sørensen entangling gate. See main text for parameter definitions.

4.4 ConsTrap Design

The experiments for the generation of the maximally entangled state $|\Psi\rangle$ have been performed in the single-layer trap called 'ConsTrap'. A schematic of the trap's electrode layout is shown in Fig. 4.2 and is comparable to the one of the multilayer trap used in publications **P2** and **P3**. It features 10 DC and 2 carrier conductors, each of them presents a S-parameter coupling to the MWM conductor of $-19.5\,\mathrm{dB}$.

The ConsTrap has been designed with a higher ion-electrode distance of $70\,\mu\mathrm{m}$ when compared to the $35\,\mu\mathrm{m}$ of the multilayer trap. Besides the MWM conductor which has a single-layer layout, the main difference between the 'ConsTrap' and the 'ML5G' trap is the shape of the RF electrode feedline. This difference can be noted by comparing the layout compared in Fig. 4.2 with the electrode structure shown in Fig. 2.1 and 3.1. The reason for this shape is to minimize the amplitude of the axial components of the RF field generating the pseudopotential. Such components could lead to unwanted axial micromotion [BMB+98]. To fully characterize the trap the same experiment

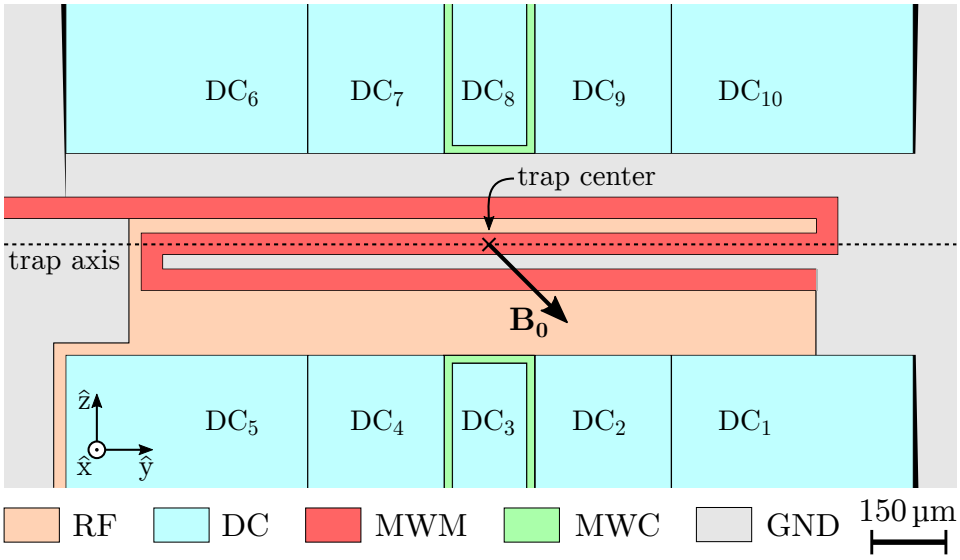

Figure 4.2: Schematic of the trap as reported in peer-reviewed publication P4, Sec. 4.8, at Fig. 1. Electrodes are highlighted with different colors on the basis of their different functionality.

described in Sec. 2.4 has been performed. In Table 4.1 the measurement and their comparison with the simulation model are reported.

	B/B' [μm]	α [°]	β [°]	ψ [°]	x_0 [μm]	z_0 [μm]
Sim.	1.910(4)	98.1(1)	88.2(1)	0.24(7)	71.144(3)	0.687(3)
Exp.	1.89(6)	84.7(9.1)	87.6(1.2)	4.0(1.3)	71.81(4)	0.08(0.6)

Table 4.1: Parameters of the microwave near-fields according to Eq. 2.1, determined from simulations and from experimental measurements of surface-electrode trap 'ConsTrap'.

The mismatch between the simulated and measured position of the quadrupole minimum (x_0, z_0) has not yet been investigated. The simulation result given relies on assuming an electrode thickness of 10.2 μm which has been measured on a trap produced from the same batch and might therefore be slightly different. Overall we can measure that the magnetic quadrupole and the pseudopotential minimum, predicted to be at $(70.60, 0.64)$ μm, are shifted by about $(1.21, -0.56)$ μm from each other.

4.5 State detection

In our setup, multi-ion state detection is performed by a photomultiplier tube (PMT) which counts the photons scattered by resonant fluorescence from the ions, see A.1 for details. Multiple detections allow to produce a histogram of photon counts. The probability to detect n photons in a single detection interval ideally follows a weighted sum of Poissonian distributions, $P_j(n)$, where each distribution has an average of $\lambda_0 + j\lambda_1$. Where $j \in \{0, 1, .., N\}$ is the number of bright ions, nλ_0 is the average number of photons detected when all ions are in the dark state and λ_1 is the average number of photons scattered by one ion when in the bright state, see the level scheme in Fig. A.1. The corresponding weight for each distribution will be equal to the populations of the state with the given amount of bright ions. For the case of two ions this results in $P_{\text{tot}}(n) = P_{\uparrow\uparrow}P_2(n) + P_{(\uparrow\downarrow,\downarrow\uparrow)}P_1(n) + P_{\downarrow\downarrow}P_0(n)$. Here $P_{\uparrow\uparrow}$, $P_{(\uparrow\downarrow,\downarrow\uparrow)}$, $P_{\downarrow\downarrow}$ are the population probabilities defined as:

$$
\begin{aligned}
P_{\uparrow\uparrow} &= \rho_{\uparrow\uparrow,\uparrow\uparrow} \\
P_{(\uparrow\downarrow,\downarrow\uparrow)} &= \rho_{\uparrow\downarrow,\uparrow\downarrow} + \rho_{\downarrow\uparrow,\downarrow\uparrow} && (4.10) \\
P_{\downarrow\downarrow} &= \rho_{\downarrow\downarrow,\downarrow\downarrow} \quad . && (4.11)
\end{aligned}
$$

Where ρ is the density matrix of the detected state and $\rho_{ii,jj} = \langle ii| \rho |jj\rangle$ is the matrix element with $i, j \in \{\uparrow, \downarrow\}$.

For measuring reliably the populations, it is necessary to account for state preparation and measurement (SPAM) errors which might affect the result. To this end, the same procedure as in [OWC+11], see methods section for more details, has been used in publication **P4**. We performed a Ramsey experiment where the phase of the second $\pi/2$ pulse is scanned. The populations at each specific phase are assumed to fit perfectly the theory. The experimentally measured histogram for i ions in the bright state is then assumed to be:

$$
P'_i(n) = \sum_{j=0}^{N} c_{ij} P_j(n) \quad . \tag{4.12}
$$

Where $P'_i(n)$ is then a sum of weighted Poissonians with coefficients c_{ij}. These coefficients indicate the probability of measuring j ions bright when preparing a state with i ions bright. Through interpolation of the Ramsey experiment

data, it is possible to obtain all the λ_j and c_{ij} coefficients and therefore calibrate the detection system to account for the experimental imperfections. Further correction of this detection analysis is needed to include additional effects such as the depumping from the dark to the bright state [ABH$^+$05, Lan06]. As a consequence, the distribution $P_0(n)$ results to be not simply a Poissonian but rather a convolution of a Poisson distribution with an exponential decay due to the optical depumping of the state. Fig. 4.3 shows an example of experimental data and the Poissonians $P_j(n)$ used in the interpolation, wherein the 'tail' belonging to distribution P_0 is due to dark to bright depumping. In the peer-reviewed publication **P4** the effect of bright to dark pumping induced by the detection laser is not considered.

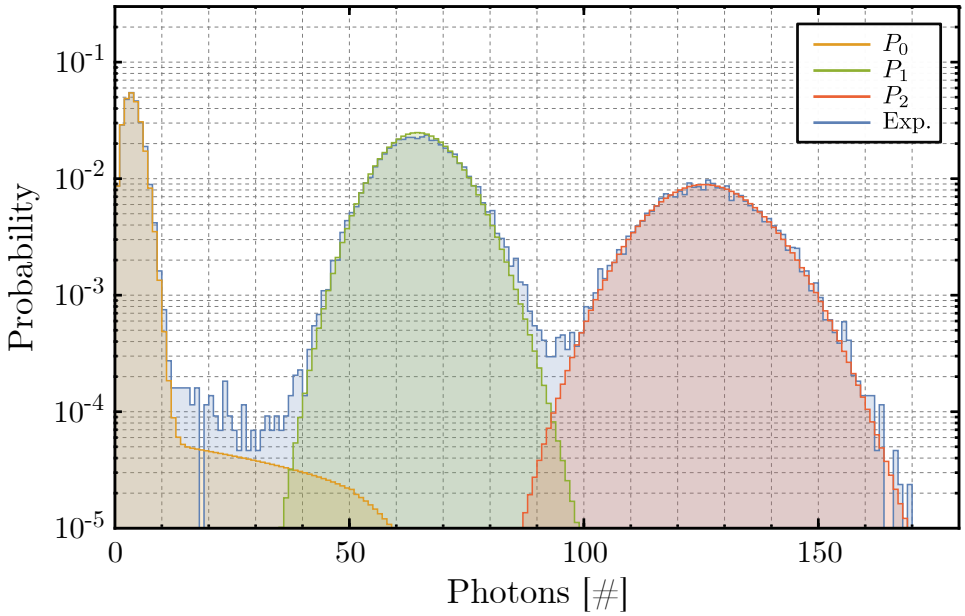

Figure 4.3: Example of experimentally measured histogram, in blue, for two ions with equal populations in all four combinations of spin states. In red and green Poissonian distribution for 2 and 1 ion in the bright state. In yellow convoluted Poissonian distribution resulting from dark to bright depumping of ions during the 400 μs long detection interval when ions are initially in the dark state.

The fidelity of the detection system for this type of collective detection is limited by how much the distributions $P_i(n)$ overlap with each other. In the case of a single detection event, if the number of detected photons is in a region where two distributions have roughly the same probability, it is not possible to determine correctly the number of bright ions. It would be possible, through additional data such as the time of arrival of the single pho-

tons. For collective PMT detection is therefore highly beneficial to have a high efficiency photon detection system to minimize the intersection region between distributions. Effort in this direction prompted the development of more efficient light collection systems [KMK11] and more efficient integrated detectors [SVL+17]. Other approaches include the use of spatially resolved detectors [BSWL10, DLF+16], time-resolved detection [MSW+08] or more advanced analysis algorithms [SLL+18].

4.6 Fidelity analysis

Different methods can be used to quantify the performance of the entangling gate operation: full quantum state tomography [VR89, RLR+04], randomized benchmarking [KLR+08] or partial tomography [SKK+00, LDM+03]. The latter is experimentally easy to implement and it has been chosen for the fidelity estimation in the peer-reviewed publications considered in this thesis. The partial tomography method consists in measuring the Bell state fidelity $\mathcal{F}$, defined as:

$$\mathcal{F} = \langle\Psi|\,\rho\,|\Psi\rangle = \frac{1}{2}\left(\rho_{\uparrow\uparrow,\uparrow\uparrow} + \rho_{\downarrow\downarrow,\downarrow\downarrow}\right) + |\rho_{\uparrow\uparrow,\downarrow\downarrow}| \quad . \tag{4.13}$$

The first two matrix elements can be measured directly from the detected fluorescence signal and are given by the populations in the states $|\uparrow\uparrow\rangle$ and $|\downarrow\downarrow\rangle$. To measure $|\rho_{\uparrow\uparrow,\downarrow\downarrow}|$ it is necessary to use a $\pi/2$ analysis pulse, on the generated entangled state, and scan its phase while the global fluorescence of the ions is monitored. This operation results in an oscillation between the states $|\Psi\rangle = \left(|\uparrow\uparrow\rangle + i\,|\downarrow\downarrow\rangle\right)/\sqrt{2}$ and $|\Phi\rangle = \left(|\uparrow\downarrow\rangle + i\,|\downarrow\uparrow\rangle\right)/\sqrt{2}$ and provides us an entanglement witness. These two maximally entangled states have opposite parity[6] and the amplitude $A(\Pi)$ of the parity oscillation is equal to $2\,|\rho_{\uparrow\uparrow,\downarrow\downarrow}|$ which is the last term needed to measure $\mathcal{F}$.

The collective fluorescence histograms resulting from a $K = 3$ loops Mølmer-Sørensen gate have been recorded after the $\pi/2$ analysis pulse and analyzed with the Poissonians sum method described in Sec. 4.5. From this analysis we estimated $\rho_{\uparrow\uparrow,\uparrow\uparrow} = 0.487(15)$, $\rho_{\downarrow\downarrow,\downarrow\downarrow} = 0.503(15)$ and a parity amplitude of $A(\Pi) = 0.975(25)$ which gives the reported fidelity of $\mathcal{F} = 0.982(12)$.

[6] Parity is defined as $\Pi = P_{\uparrow\uparrow} + P_{\downarrow\downarrow} - P_{\uparrow\downarrow} - P_{\downarrow\uparrow}$

4.7 Main sources of errors

To improve the gate performances, after measuring the gate fidelity $\mathcal{F}$, it is important to identify the sources of infidelity and their relevance in an error budget. Table 4.2 reports an excerpt of the error budget from peer-reviewed publication **P4**. The error sources presented here are only the most relevant ones.

Effect	Infidelity $[1-\mathcal{F}]$
Mode instability	1.3×10^{-2}
Spectator mode	5.2×10^{-3}
Motional heating	3.8×10^{-3}

Table 4.2: Excerpt of gate error contributions from **P4**. Only the major components have been here reported.

It can be noted that all the effects reported are connected to the motion of the ions. The individual infidelity contribution to the gate were obtained by performing appropriate simulations of the full system dynamics using the Python package QuTip [noa16]. The parameters used in the simulations are the ones measured in the setup with appropriate characterization experiments. The simulation therefore includes Linblad operators to account for non-unitary dynamics such as qubit decoherence and motional heating. It is to be noted that the total measured experimental infidelity of $1.8(1.2) \times 10^{-2}$ is larger than the sum of the contributions reported. As a consequence, we assume that by reducing these three major effects, the fidelity of the gate can be considerably improved.

The smallest contribution to the infidelity is given by the motional heating of the mode of interest. The motional heating describes the energy increase of the ion motion due to interaction with the electric field noise of its environment. Possible ways to reduce heating rate effects can be: cleaning of the trap surface [HCW+12, AGH+11], cryogenic operation [BKRB15] or faster gate operation [SBT+18].

A slightly stronger infidelity contribution is given by the presence of additional motional modes, so-called spectator modes, which are off-resonantly

excited by the Mølmer-Sørensen interaction. One possible counter-measure for this error would be a better engineering of the trapping potential to increase frequency separation of the motional modes. The increased separation reduce the interaction of the gate drive with the spectator modes but leaving unaltered the interaction with the desired motional mode.

The largest contribution, with more than 1% of the total infidelity is given by the motional mode instability. It is mainly caused by two components: fast fluctuations of the motional mode frequency and the so-called frequency 'chirp'. Fast variations of the motional mode frequency ω_r with respect to the single experiment timescales, lead to the frequencies used in the bichromatic drive to be, for short instants, at the wrong values. This effect is generally connected to amplitude and frequency instabilities of the RF frequency drive and can potentially be solved through technical improvements [JWCR+16]. The second component which contributes to the motional mode instability is the frequency 'chirp'. This effect describes a motional mode frequency change while the gate drive is applied to the MWM conductor. This effect has been observed also in other near-field microwave experiments [HSA+16] and is suspected to be induced by thermal transients in the trap structures due to the high power of the applied microwave signal. To reduce such transients, a warm-up high power microwave pulse has been inserted before the actual bichromatic drive in the peer-reviewed publication. The purpose is to pre-warm the trap structures to reduce the effect of the frequency 'chirp'; it is therefore applied directly before preparing the ions in the $|\uparrow\uparrow\rangle$ state.

All these infidelity contributions, as stated initially, can be attributed to the motional mode of the ions described by the quantum harmonic oscillator. The next chapter shows that, by accurately engineering the gate drive interaction with the motional mode through quantum control techniques, the final maximally entangled Bell state can be made robust against these kind of infidelity contributions.

4.8 P4: Integrated $^{9}Be^{+}$ multi-qubit gate device for the ion-trap quantum computer

Authors: H. Hahn, **G. Zarantonello**, M. Schulte, A. Bautista-Salvador, K. Hammerer and C. Ospelkaus.

Journal: Nature Physics Journal Quantum Information

DOI: 10.1038/s41534-019-0184-5

Authors contribution: HH and **GZ** performed the measurements and analyzed the data. ABS produced the ion trap. MS and KH contributed the numerical simulations. CO devised the experiment plan. All authors participated in the error analysis and the realization of the manuscript.

npj | Quantum Information

www.nature.com/npjqi

ARTICLE OPEN

Integrated $^{9}Be^{+}$ multi-qubit gate device for the ion-trap quantum computer

H. Hahn[1,2], G. Zarantonello[1,2], M. Schulte[3], A. Bautista-Salvador[1,2,4], K. Hammerer[3] and C. Ospelkaus[1,2,4]

We demonstrate the experimental realization of a two-qubit Mølmer–Sørensen gate on a magnetic field-insensitive hyperfine transition in $^{9}Be^{+}$ ions using microwave near-fields emitted by a single microwave conductor embedded in a surface-electrode ion trap. The design of the conductor was optimized to produce a high oscillating magnetic field gradient at the ion position. The measured gate fidelity is determined to be 98.2 ± 1.2% and is limited by technical imperfections, as is confirmed by a comprehensive numerical error analysis. The conductor design can potentially simplify the implementation of multi-qubit gates and represents a self-contained, scalable module for entangling gates within the quantum CCD architecture for an ion-trap quantum computer.

npj Quantum Information (2019)5:70 ; https://doi.org/10.1038/s41534-019-0184-5

INTRODUCTION

Following the proposal by Cirac et al.,[1] trapped atomic ions have shown to be a promising and pioneering platform for implementing elements of quantum information processing (QIP).[2,3] Qubits are encoded in the internal states of individual ions, and shared motional modes are used as a "quantum bus" for multi-qubit operations. Toward a large-scale universal quantum processor based on trapped-ion qubits, the "Quantum Charge-Coupled Device" (QCCD)[4,5] is considered as a possible scalable hardware implementation. It relies on microfabricated multi-zone ion-trap arrays, in which quantum information is processed in dedicated zones interconnected via ion transport. While some key requirements such as high-fidelity ion transport[6] and fault-tolerant single-qubit gates[7,8] have already been demonstrated in multiple setups, high-fidelity multi-qubit gates[9,10] below the fault-tolerant threshold still remain challenging. In this context, entangling gates driven by microwave fields[11,12] represent a technically less demanding alternative to laser-induced gates, as microwave signals can typically be controlled more easily than optical fields from highly specialized laser systems. The microwave approach avoids spontaneous scattering as a fundamental source of infidelities[13] and experimental fidelities[14–17] are approaching the fidelities of the best laser-driven gates.[9,10] Here, we focus on the near-field microwave[12] gate approach, where the leading sources of infidelity in implementations so far comprise the spatio-temporal stability of the microwave near-field pattern[14,18] or fluctuating AC Zeeman shifts.[17,19] We note that in the latter work, the error contribution arising from fluctuating AC Zeeman shifts has been reduced to $\lesssim$0.1% through the use of a dynamical decoupling scheme.[17]

In this letter, we realize a two-qubit gate using a tailored microwave conductor embedded in a surface-electrode trap optimized to produce high oscillating magnetic near-field gradients and low residual fields at the ion position, thus directly addressing the main sources of error in previous near-field gates. The gate is realized on a field-independent hyperfine qubit in $^{9}Be^{+}$ ions, a promising ion species for scalable QIP,[20–22] following the Mølmer–Sørensen (MS)[23–26] protocol. The implementation is based on an optimized single-conductor design, which can be thought of as the prototype of a scalable multi-qubit gate module for an ion-trap quantum computer based on surface-electrode trap arrays. The measured gate fidelity of 98.2 ± 1.2% is purely limited by technical imperfections, in agreement with a numerical analysis.

RESULTS AND DISCUSSION

The surface-electrode trap was fabricated at the PTB cleanroom facility employing the single-layer method as detailed in ref. [27] on an AlN substrate (for the present trap, we chose the single-layer process in order to quickly test improvements that were made to the setup and trap orientation compared with ref. [28]). Gold electrodes are about 10 µm thick and separated by 5 µm gaps. Aiming to remove potential organic residuals on top of the electrode surfaces, the trap was cleaned in an ex situ dry-etching process before being installed in a UHV vacuum chamber at room temperature. Electrical connectivity is provided by wire bonding to a printed-circuit board for DC signal filtering and signal routing.

Figure 1 shows a top view of the trap center. Besides the microwave conductor MWM, which produces a magnetic field quadrupole[29] suitable for driving multi-qubit gates, the electrode layout includes two microwave conductors labeled MWC to generate an oscillating magnetic field for global spin-state manipulation. The ions are radially and axially confined at an ion-to-electrode distance of about 70 µm using one radio frequency (RF) and 10 DC control electrodes, respectively. With an applied RF voltage of 150V_{pp} at $\Omega_{RF} \simeq 2\pi \times 88.2$ MHz, the motional-mode frequencies of the radial rocking modes of a two-

[1]Physikalisch-Technische Bundesanstalt, Bundesallee 100, 38116 Braunschweig, Germany; [2]Institute of Quantum Optics, Leibniz University Hannover, Welfengarten 1, 30167 Hannover, Germany; [3]Institute for Theoretical Physics and Institute for Gravitational Physics (Albert-Einstein-Institute), Leibniz University Hannover, Appelstrasse 2, 30167 Hannover, Germany and [4]Laboratory for Nano- and Quantum Engineering, Leibniz University Hannover, Schneiderberg 39, 30167 Hannover, Germany
Correspondence: C. Ospelkaus (christian.ospelkaus@iqo.uni-hannover.de)

Received: 8 March 2019 Accepted: 26 July 2019
Published online: 16 August 2019

Published in partnership with The University of New South Wales

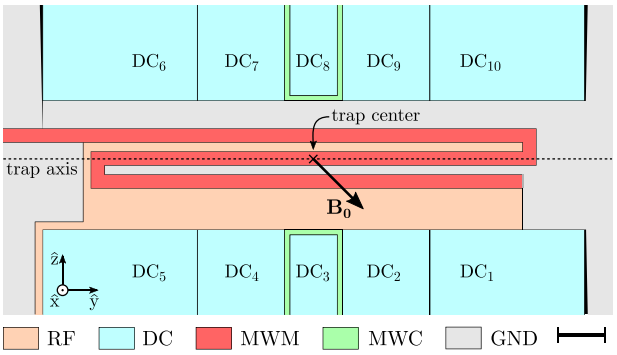

Fig. 1 Electrode configuration around the trap center. The ions are confined 70 µm above the surface using 10 DC control electrodes and one split RF electrode. The microwave conductor labeled MWM produces an oscillating magnetic near-field gradient in the $\hat{x}$–$\hat{z}$ plane in order to drive an entangling gate on two hyperfine qubits. The two microwave conductors labeled MWC can each generate an oscillating magnetic field for global manipulation of the spin state in the $^2S_{1/2}$ manifold. Scale bar: 150 µm (bottom right)

ion $^9Be^+$ crystal were measured to be $(\omega_{r1}, \omega_{r2}) \simeq 2\pi \times (6.275, 6.318)$ MHz.

The static magnetic field $\mathbf{B_0}$ defining the quantization axis at an angle of 45° with respect to the trap axis is produced by a hybrid setup consisting of two permanent magnet assemblies and a pair of compensation coils.[30] At the ion position, this setup generates a magnetic field of $|\mathbf{B_0}| = 22.3$ mT forming a first-order magnetic field-insensitive qubit[31] on the hyperfine levels $^2S_{1/2}|F=1, m_F=1\rangle \equiv |\uparrow\rangle$ and $^2S_{1/2}|F=2, m_F=1\rangle \equiv |\downarrow\rangle$ with an unperturbed transition frequency of $\omega_0 \simeq 2\pi \times 1082.55$ MHz, cf. Fig. 2. Here, F and m_F represent the quantum numbers for the ion's total angular momentum and its projection on the quantization axis, respectively.

Ions are loaded using laser ablation combined with photo-ionization.[29] State initialization is done via optical pumping to the $|2, 2\rangle$ state (also referred to as the bright state) and subsequent Doppler cooling on the closed-cycle transition $^2S_{1/2}|2, 2\rangle \leftrightarrow {}^2P_{3/2}\left|m_J = \frac{3}{2}, m_I = \frac{3}{2}\right\rangle$ (where m_J and m_I are the projections of the total electronic and nuclear angular momenta onto the quantization axis). Resolved sideband cooling is performed by a pair of counter-propagating Raman beams aligned along the $\hat{z}$ direction. Each sideband cooling cycle consists of a global π rotation on the hyperfine transition labeled "I" in Fig. 2, followed by an optical red sideband pulse on the qubit transition and a repumping sequence to transfer all population back to the initial bright state. The repumping sequence comprises multiple microwave induced π rotations on the qubit transition and laser pulses on the $^2S_{1/2}|1, 1\rangle \leftrightarrow {}^2P_{3/2}\left|\frac{1}{2}, \frac{3}{2}\right\rangle$ transition similar to ref. [18] Employing interleaved sideband cooling sequences on both radial rocking modes of a two-ion crystal, we measure a mean phonon number $\bar{n}$ of the modes $\bar{n}_{r1} \simeq 0.27$ and $\bar{n}_{r2} \simeq 0.11$ assuming a thermal distribution. The heating rate was determined to be $\dot{\bar{n}}_{r2} \simeq 28 s^{-1}$. In an earlier measurement with similar radial-mode frequencies, the heating rates of a single-ion's low-frequency (LF) and high-frequency (HF) radial mode were found to be about $\dot{\bar{n}}_{LF} \simeq 116 s^{-1}$ and $\dot{\bar{n}}_{HF} \simeq 122 s^{-1}$, respectively.

To perform a MS two-qubit entangling gate on the qubit transition using near-field microwaves,[12] we subsequently initialize the qubits in $|\uparrow\uparrow\rangle$ and apply a bichromatic microwave current to MWM at the frequencies $\omega_{RSB} = \omega_0 + \Delta - (\omega_{r2} + \delta)$ and $\omega_{BSB} = \omega_0 + \Delta + (\omega_{r2} + \delta)$. Here, δ is the gate detuning from the high-frequency rocking mode of $N = 2$ ions at ω_{r2}, and Δ is the differential AC Zeeman shift of the unperturbed qubit transition induced by the bichromatic field. In the ideal case, the

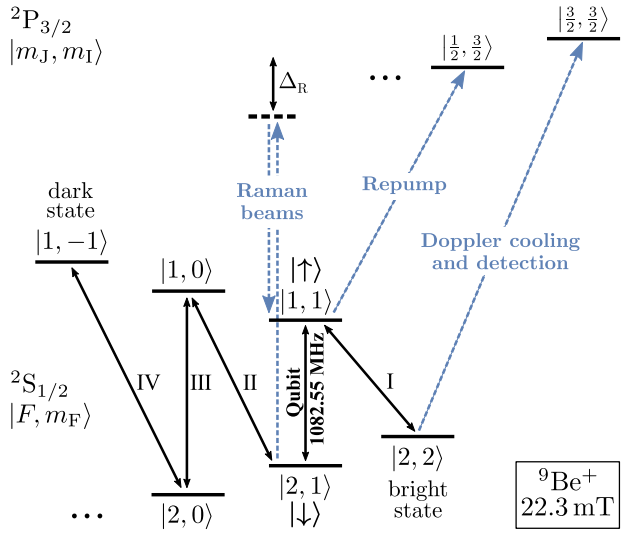

Fig. 2 Relevant energy levels of $^9Be^+$ at 22.3 mT. The transitions indicated as blue dashed lines are addressed by laser beams, while the transitions indicated by black solid lines are driven by microwave radiation. The Raman beam detuning is $\Delta_R \simeq 100$ GHz below the line center of the $^2P_{3/2}$ manifold

implemented dynamics can be described by the Hamiltonian

$$H_{MS} = \frac{\Omega}{2} \sum_{j=1}^{N} (\sigma_j^+ + \sigma_j^-)(a_{r2} e^{i\delta t} + a_{r2}^\dagger e^{-i\delta t}), \quad (1)$$

where Ω is the gate Rabi frequency, a_{r2} ($a_{r2}^\dagger$) represents the mode's annihilation (creation) operator and we define $\sigma^\pm = 1/2(\sigma^x \pm i\sigma^y)$ with σ^x and σ^y being the Pauli matrices. Following,[32,33] we apply the interaction on $|\uparrow\uparrow\rangle$ in order to produce the maximally entangled state $|\Psi\rangle = 1/\sqrt{2}(|\uparrow\uparrow\rangle + i|\downarrow\downarrow\rangle)$ at time $\tau = \pi\sqrt{K}/\Omega$ (where K is an integer number) and calculate the resulting state preparation fidelity $\mathcal{F} \equiv \langle\Psi|\rho|\Psi\rangle = 1/2(P_{\uparrow\uparrow} + P_{\downarrow\downarrow}) + |\rho_{\uparrow\uparrow,\downarrow\downarrow}|$ by determining the far off-diagonal element $\rho_{\uparrow\uparrow,\downarrow\downarrow}$ of the system's density matrix ρ as well as the population probabilities in $|\downarrow\downarrow\rangle$, $|\uparrow\downarrow\rangle$, and $|\downarrow\uparrow\rangle$, and $|\uparrow\uparrow\rangle$ given by $P_{\downarrow\downarrow}$, $P_{\uparrow\downarrow,\downarrow\uparrow}$, and $P_{\uparrow\uparrow}$, respectively.

Experimentally, we infer these quantities by adding a $\pi/2$ analysis pulse after the gate operation and observe the global ion fluorescence as a function of the analysis pulse's phase ϕ_a employing fluorescence detection on the closed-cycle transition for 400 µs. Prior to detection, we transfer the population in $|\uparrow\rangle$ back to the bright state and shelve the population in $|\downarrow\rangle$ to $|1, -1\rangle$ (also referred to as the dark state) using a sequence of π rotations on the transitions "I" and "II"–"IV", respectively. The populations are determined by repeating the experiment 200 times for each value of ϕ_a, and fitting the resulting histograms to a sum of weighted Poisson distributions representing 0, 1, and 2 ions bright. We calibrate the mean of the distributions to a reference two-ion Ramsey experiment which we assume to produce an ideal outcome following the same procedure of[14] (see Supplementary Methods section). To account for off-resonant optical pumping effects, we modify the three Poissonians to include all depumping processes from the shelved dark state to the bright state during the detection interval.[34] By consequence, we expect the resulting populations to compensate imperfect state preparation and detection within the present level of accuracy. Finally, $\rho_{\uparrow\uparrow,\downarrow\downarrow}$ can be deduced by calculating the parity $\Pi(\phi_a) = P_{\downarrow\downarrow}(\phi_a) + P_{\uparrow\uparrow}(\phi_a) - P_{\uparrow\downarrow+\downarrow\uparrow}(\phi_a)$, while ϕ_a is varied and extracting the magnitude $|A_\Pi|$ of the parity oscillation equal to $|2\rho_{\uparrow\uparrow,\downarrow\downarrow}|$.[33] Figure 3 shows the population and parity signal after performing the two-qubit gate operation using the MWM conductor. From sinusoidal fits to the extracted populations (solid lines), we calculate a corresponding gate fidelity of 98.2 ± 1.2%. The error on the fidelity is derived from

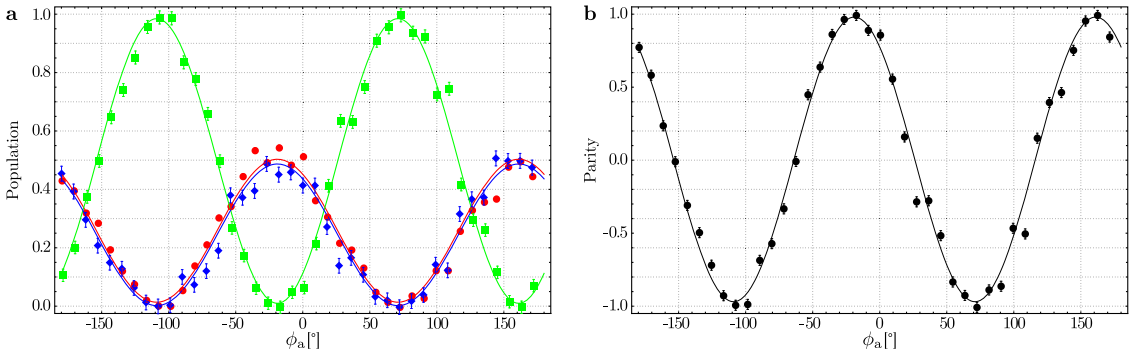

Fig. 3 Population and parity oscillation as a function of the phase ϕ_a of a $\pi/2$ analysis pulse applied after preparing the maximally entangled state $|\Psi\rangle = 1/\sqrt{2}(|\uparrow\uparrow\rangle + i|\downarrow\downarrow\rangle)$ utilizing the near-field pattern of the MWM conductor. The solid lines are sinusoidal fits to the observed data, while each data point represents the average of 200 experiments. The error bars result from the fit of the weighted Poissonians to the experimental data. **a** Population in $|\downarrow\downarrow\rangle$ ($P_{\downarrow\downarrow}$; red circles), $|\uparrow\downarrow\rangle$ and $|\downarrow\uparrow\rangle$ ($P_{\uparrow\downarrow,\downarrow\uparrow}$; green squares) and $|\uparrow\uparrow\rangle$ ($P_{\uparrow\uparrow}$; blue diamonds). The fits yield $P_{\uparrow\uparrow} + P_{\downarrow\downarrow} = 0.990 \pm 0.021$. **b** Parity $\Pi(\phi_a) = P_{\downarrow\downarrow}(\phi_a) + P_{\uparrow\uparrow}(\phi_a) - P_{\uparrow\downarrow,\downarrow\uparrow}(\phi_a)$ oscillation with a fitted amplitude of $A_\Pi = 0.975 \pm 0.012$

the uncertainties in the population fits. In more detail, we apply a power of ~5.5 W to each sideband tone, resulting in gate Rabi frequency of $\Omega/2\pi = 1.071$ kHz and an inferred near-field gradient of ~19 Tm^{-1}. For a single sideband, the corresponding residual magnetic field at the ion position is highly suppressed by the optimized conductor geometry, resulting in an on-resonance Rabi frequency of about $\Omega_c/2\pi$~450 kHz. In case the bichromatic gate drive is applied, the accompanied differential AC Zeeman shift is measured to be $\Delta/2\pi = 4.37$ kHz and is predominantly caused by σ-components of the residual magnetic fields as the induced shifts of the π-components mainly cancel each other assuming an equal power in both sideband tones. In order to suppress off-resonant spin excitations, we adiabatically shape the envelope of the gate pulse at its beginning and end with a 2 -µs long cumulative error function using a microwave envelope stabilization circuit based on a fast analog multiplier and a digital PI controller[35] with the regulator setpoint generated by an arbitrary waveform generator.[36] We optimize the gate by fixing the pulse duration to the expected value based on the gate Rabi frequency and subsequently scanning the gate detuning resulting in the highest fidelity. Following this procedure, we find an optimal gate time and detuning of $\tau = 808$ µs and $\delta/2\pi = 3.4$ kHz, respectively, corresponding to $K = 3$ loops in motional-phase space. Here, the mismatch to the theoretically predicted detuning at $\delta_{\mathrm{theory}}/2\pi =$ 3.71 kHz was tracked back to a systematic frequency offset from an independent radial-mode frequency measurement as well as a radial mode frequency "chirp" of 0.3 Hz μs^{-1} during the gate pulse. Qualitatively, a similar effect is also observed in other experiments using near-field gradients and appears to be inherent to warm-up processes in the microwave-generating structures.[19] This hypothesis is supported by our observation of a saturation behavior of the "chirp" at ~1 ms. Consequently, we reduce the impact of the "chirp" by preceding the gate with a 400 -µs long warm-up pulse with the duration chosen conservatively to avoid excessive heating of trap structures.

In order to identify current infidelity contributions in producing the maximally entangled state, we simulate the dynamics of the system using a master equation considering experimentally determined input parameters. This becomes necessary, as the exact propagator may no longer be obtained analytically in the presence of additional error sources. The master equation is given by

$$\dot{\rho} = -i[H, \rho] + \mathcal{L}_h\rho + \mathcal{L}_d\rho \tag{2}$$

where the Hamiltonian is $H = \tilde{H}_{\mathrm{MS}} + H_{\mathrm{m}} + H_{\mathrm{z}} + H_{\mathrm{spec}}$, and

$$\tilde{H}_{\mathrm{MS}} = \frac{1}{2}\sum_{j=1}^{N}(\Omega^{\mathrm{B}}(t)\sigma_j^+ a_{r2}^\dagger e^{-i\delta t} + \Omega^{\mathrm{R}}(t)\sigma_j^+ a_{r2} e^{i\delta t}) + \mathrm{H.c.} \tag{3}$$

is an extension to the ideal case presented in Eq. (1). Here, we have assumed equal Rabi frequencies and phases for both ions, which is true in the experiment to the best of our knowledge. Further, $H_{\mathrm{m}} = \delta_\epsilon(t) a_{r2}^\dagger a_{r2}$ describes the instability of the rocking mode frequency, $H_{\mathrm{z}} = \Delta_\epsilon(t)/2\sum_j \sigma_j^{\mathrm{z}}$ gives the uncompensated AC Zeeman shift resulting from shot-to-shot microwave power fluctuations, general Ω^{B} and Ω^{R} allow an imbalance in the two sideband Rabi frequencies, and time dependencies of the pulse shape are taken into account by the time-dependent parameters. Couplings via additional, off-resonant motional modes are included by the term $H_{\mathrm{spec}} = \Omega_{r1}/2\sum_{j=1}^{N}(\sigma_j^+ + \sigma_j^-)(a_{r1}e^{i(\Delta\nu+\delta)t} + a_{r1}^\dagger e^{-i(\Delta\nu+\delta)t})$ whereby we limit ourselves to the nearest mode only (with $\Omega_{r1} \simeq \Omega$), which contributes the largest error of this kind. In addition to the unitary dynamics, motional heating to a thermal state with $\overline{n}_{\mathrm{th}} \gg 1$ and qubit decoherence are considered by the Lindblad terms[32] $\mathcal{L}_{\mathrm{h}}\rho = \gamma_{\mathrm{h}}(\mathcal{D}[a_{r2}]\rho + \mathcal{D}[a_{r2}^\dagger]\rho)$ with the heating rate γ_{h} in phonons per second and $\mathcal{L}_{\mathrm{d}}\rho = \gamma_{\mathrm{d}}/2\sum_j \mathcal{D}[\sigma_j^{\mathrm{z}}]\rho$ with the decoherence rate γ_{d}, respectively, where $\mathcal{D}[\hat{O}]\rho = \hat{O}\rho\hat{O}^\dagger - \hat{O}^\dagger\hat{O}\rho/2 - \rho\hat{O}^\dagger\hat{O}/2$.

Table 1 lists contributions of the different error sources to the infidelity $1 - \mathcal{F}$. These values result from numerical simulations of the quantum dynamics according to Eq. (2) considering the ideal gate dynamics with addition of the corresponding noise in the form we described above. All simulations were done with QuTiP[37] and used a truncated Hilbert space for the motional mode. For our analysis, including the first 25 Fock states was sufficient to reach convergence given the low initial thermal distribution and the small motional displacements during the gate.

We examined the following effects, which we considered to be the most relevant, in more detail: the largest error according to our investigation results from the frequency instability of the rocking mode, which establishes the gate dynamics. This effect consists of two parts. On the one hand, normally distributed variations of the frequency with a standard deviation of $\sqrt{\langle(\delta_\epsilon/\delta)^2\rangle} = 1.1 \times 10^{-2}$, inferred from a measured instantaneous linewidth of $2\pi \times 101$ Hz in a calibration scan directly before the gate measurement. On the other hand, a frequency "chirp" within each gate that we model by a linear increase of 0.3 Hz μs^{-1} within the first 600 µs, and subsequent constant frequency leading to in total 1.3% infidelity. While the mode fluctuations can be reduced by actively stabilizing the amplitude and frequency of the trap RF signal,[38,39] the "chirp" can be reduced by e.g., longer warm-up pulses. Simulations (see Fig. 4) also us to identify the individual contribution of each effect in view of further improvements.

The second largest contribution is caused by driving the identical spin–spin interaction via the additional low-frequency

Table 1. Infidelity contributions from different sources of imperfections

Effect	Parameter	Infidelity
Mode instability	$\sqrt{\langle(\delta_\epsilon/\delta)^2\rangle} = 1.1\times10^{-2}$ 0.3 Hz μs^{-1} "chirp" for 600 μs	1.3×10^{-2}
Spectator mode	$\Delta\nu = 2\pi\times42.5$ kHz with $\overline{n}_{r1} = 0.27$	5.2×10^{-3}
Motional heating	$\gamma_h = \dot{\overline{n}}_{r2} = 28\,s^{-1}$	3.8×10^{-3}
Off-resonant scattering loss	Measured infidelity following refs. [19,43]	$<2.3\times10^{-3}$
Qubit decoherence	$\tau_d = 1/\gamma_d > 0.5$ s	$<9.3\times10^{-4}$
Pulse shape	See main text	6.3×10^{-4}
ACZS fluctuations	$\sqrt{\langle(\Delta_\epsilon/\Delta)^2\rangle} = 8\times10^{-4}$	1.1×10^{-4}
Rabi frequency imbalance	$\frac{\Omega_R-\Omega_B}{\Omega_B} = 2.33\times10^{-2}$	4.1×10^{-6}

The infidelity values result from numerical simulations of the quantum dynamics according to Eq. (2), including the respective noise effect with a strength given by the measured parameter specified in the second column

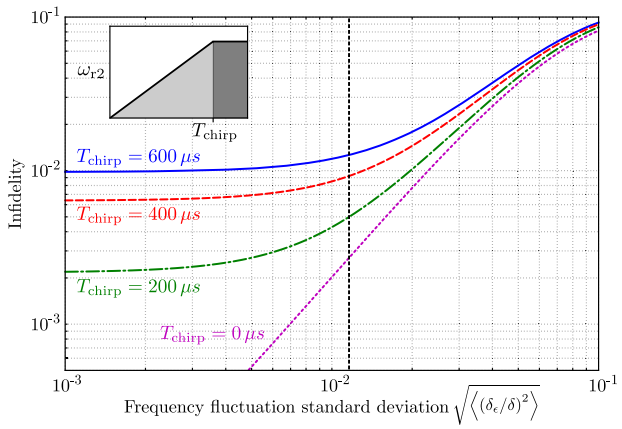

Fig. 4 Simulated infidelity assuming different variations of the relative motional mode frequency and lengths of the frequency "chirp" while considering otherwise ideal gate dynamics. In all cases, the gate parameters are as specified in the text. The experimental condition of the presented two-qubit gate is given by the intersection of the vertical line with the solid blue line. The inset illustrates the observed linear frequency increase of the selected motional mode of about 0.3 Hz μs^{-1} at the beginning of the gate pulse until time T_{chirp}

rocking mode. The measured frequency spacing was $\Delta\nu = \omega_{r2}-\omega_{r1} = 2\pi\times42.5$ kHz and ground-state cooling to $\overline{n}_{r1} = 0.27$ was applied, resulting in an infidelity of 5.2×10^{-3} from the competing gate dynamics. As this effect scales inversely with the radial-mode splitting, it can be suppressed by engineering the trap potentials or suitable pulse sequences.[40,41] Heating of the motion and decoherence of the qubits contribute ~0.1% and <0.1% infidelity, respectively. Again, both effects do not represent a fundamental limit to the gate performance and can be improved experimentally.[31,42] Off-resonant scattering on carrier transitions can lead to undesired excitations inside and outside the qubit-manifold and thus contribute a gate error. Here, an excitation other than on the qubit transition is much less probable due to the higher-frequency difference of the driving field, which is >150 MHz detuned from the next spectator transition. Direct simulation of this effect was not performed due to the vastly different timescales of the gate dynamics (~kHz) and the carrier processes (~GHz) which would have considerably increased the runtime of the numerical simulations. We instead performed direct measurements on a single qubit[19,43] to evaluate the extent of this error, which is then quantified to be $<2.3\times10^{-3}$. Infidelities below 6.3×10^{-4} resulted from distortion of the pulse shape, whereby we combine here the influence of adiabatic switching on and off as well as small changes of the Rabi frequency and AC Zeeman shift during the pulses which result from power transients on the ideally rectangular signal. Stabilization of the microwave power allowed to reduce the shot-to-shot fluctuations of the power, and accordingly of the AC Zeeman shift, to an extent that the simulated infidelity of 1.1×10^{-4} contributes only insignificantly. The same applies to the imbalance of Rabi frequencies, cf. Table 1.

In conclusion, we have demonstrated a microwave-driven two-qubit gate with $^9Be^+$ ions using a single microwave conductor with an optimized design embedded in a surface-electrode ion trap. The design of the MWM conductor has been developed to generate a high magnetic near-field gradient with low residual field at the ion position, thus suppressing AC Zeeman shift fluctuations, an inherent error source of the near-field approach, to a simulated infidelity contribution of ~10^{-4}. In contrast, according to the presented error budget, the main contributions can all be decreased upon technical improvements; the by far biggest of these (1.3%) is consistent with the measured two-qubit gate infidelity of 1.8 ± 1.2%. In addition to technical modifications to the apparatus, more elaborate gate schemes employing Walsh modulation[44] or continuous dynamic decoupling[17] can be applied in order to increase the gate fidelity as required for fault-tolerant quantum computation. In the future, the MWM conductor design can be used as an entangling gate unit of a "QCCD" architecture purely employing microwave-driven quantum gates. Moreover, the conductor design can also be integrated into a scalable multilayer trap.[27,28]

DATA AVAILABILITY

The datasets generated during and/or analyzed during the current study are available from C. Ospelkaus (christian.ospelkaus@iqo.uni-hannover.de) on reasonable request.

ACKNOWLEDGEMENTS

We acknowledge funding from DFG through CRC 1227 DQ-*mat*, projects A01 and A06, and the clusters of excellence "QUEST" and "Quantum Frontiers", from the EU QT flagship project "MicroQC" and from PTB and LUH.

AUTHOR CONTRIBUTIONS

H.H. and G.Z. performed the measurements and analyzed the data. A.B.S. produced the ion trap. M.S. and K.H. contributed the numerical simulations. C.O. devised the experiment plan. All authors participated in the error analysis and the realization of the paper.

ADDITIONAL INFORMATION

Competing interests: The authors declare no competing interests.

Publisher's note: Springer Nature remains neutral with regard to jurisdictional claims in published maps and institutional affiliations.

REFERENCES

1. Cirac, J. I. & Zoller, P. Quantum computations with cold trapped ions. *Phys. Revi. Lett.* **74**, 4091 (1995).
2. Blatt, R. & Wineland, D. Entangled states of trapped atomic ions. *Nature* **453**, 1008–1015 (2008).
3. Monroe, C. & Kim, J. Scaling the ion trap quantum processor. *Science* **339**, 1164–1169 (2013).
4. Wineland, D. J. et al. Experimental issues in coherent quantum-state manipulation of trapped atomic ions. *J. Res. NIST* **103**, 259–328 (1998).
5. Kielpinski, D., Monroe, C. & Wineland, D. J. Architecture for a large-scale ion-trap quantum computer. *Nature* **417**, 709–711 (2002).

6. Blakestad, R. B. et al. High-fidelity transport of trapped-ion qubits through an X-junction trap array. *Phys. Rev. Lett.* **102**, 153002 (2009).
7. Brown, K. R. et al. Single-qubit-gate error below 10–4 in a trapped ion. *Phys. Rev. A* **84**, 030303 (2011).
8. Harty, T. et al. High-fidelity preparation, gates, memory, and readout of a trapped-ion quantum bit. *Phys. Rev. Lett.* **113**, 220501 (2014).
9. Gaebler, J. et al. High-fidelity universal gate set for Be 9+ ion qubits. *Phys. Rev. Lett.* **117**, 060505 (2016).
10. Ballance, C., Harty, T., Linke, N., Sepiol, M. & Lucas, D. High-fidelity quantum logic gates using trapped-ion hyperfine qubits. *Phys. Rev. Lett.* **117**, 060504 (2016).
11. Mintert, F. & Wunderlich, C. Ion-trap quantum logic using long-wavelength radiation. *Phys. Rev. Lett.* **87**, 257904 (2001).
12. Ospelkaus, C. et al. Trapped-ion quantum logic gates based on oscillating magnetic fields. *Phys. Revi. Lett.* **101**, 090502 (2008).
13. Ozeri, R. et al. Errors in trapped-ion quantum gates due to spontaneous photon scattering. *Phys. Rev. A* **75**, 042329 (2007).
14. Ospelkaus, C. et al. Microwave quantum logic gates for trapped ions. *Nature* **476**, 181–184 (2011).
15. Khromova, A. et al. Designer spin pseudomolecule implemented with trapped ions in a magnetic gradient. *Phys. Rev. Lett.* **108**, 220502 (2012).
16. Weidt, S. et al. Trapped-ion quantum logic with global radiation fields. *Phys. Rev. Lett.* **117**, 220501 (2016).
17. Harty, T. et al. High-fidelity trapped-ion quantum logic using near-field microwaves. *Phys. Rev. Lett.* **117**, 140501 (2016).
18. Warring, U. et al. Techniques for microwave near-field quantum control of trapped ions. *Phys. Rev. A* **87**, 013437 (2013).
19. Sepiol, M. A. *A High-fidelity Microwave Driven Two-qubit Quantum Logic Gate in 43Ca+*. PhD thesis, Oxford (2016).
20. Home, J. P. et al. Complete methods set for scalable ion trap quantum information processing. *Science* **325**, 1227–1230 (2009).
21. Tan, T. R. et al. Demonstration of a dressed-state phase gate for trapped ions. *Phys. Rev. Lett.* **110**, 263002 (2013).
22. Negnevitsky, V. et al. Repeated multi-qubit readout and feedback with a mixed-species trapped-ion register. *Nature* **563**, 527–531 (2018).
23. Sørensen, A. & Mølmer, K. Quantum computation with ions in thermal motion. *Phys. Revi. Lett.* **82**, 1971–1974 (1999).
24. Mølmer, K. & Sørensen, A. Multiparticle entanglement of hot trapped ions. *Phys. Rev. Lett.* **82**, 1835 (1999).
25. Milburn, G., Schneider, S. & James, D. Ion trap quantum computing with warm ions. *Fortschr. Phys.* **48**, 801–810 (2000).
26. Solano, E., de Matos Filho, R. L. & Zagury, N. Deterministic Bell states and measurement of the motional state of two trapped ions. *Phys. Rev. A* **59**, R2539 (1999).
27. Bautista-Salvador, A. et al. Multilayer ion trap technology for scalable quantum computing and quantum simulation. *New J. Phys.* **21**, 043011 (2019).
28. Hahn, H. et al. Multilayer ion trap with three-dimensional microwave circuitry for scalable quantum logic applications. *Appl. Phys. B* **125**, 154 (2019).
29. Wahnschaffe, M. et al. Single-ion microwave near-field quantum sensor. *Appl. Phys. Lett.* **110**, 034103 (2017).
30. Hakelberg, F., Kiefer, P., Wittemer, M., Schaetz, T. & Warring, U. Hybrid setup for stable magnetic fields enabling robust quantum control. *Sci. Rep.* **8**, 4404 (2018).
31. Langer, C. et al. Long-lived qubit memory using atomic ions. *Phys. Rev. Lett.* **95**, 060502 (2005).
32. Sørensen, A. & Mølmer, K. Entanglement and quantum computation with ions in thermal motion. *Phys. Rev. A* **62**, 022311 (2000).
33. Sackett, C. A. et al. Experimental entanglement of four particles. *Nature* **404**, 256–259 (2000).
34. Langer, C. E. *High Fidelity Quantum Information Processing with Trapped Ions*. PhD Thesis, University of Colorado (2006).
35. Hannig, S. et al. A highly stable monolithic enhancement cavity for second harmonic generation in the ultraviolet. *Rev. Sci. Instrum.* **89**, 013106 (2018).
36. Bowler, R., Warring, U., Britton, J. W., Sawyer, B. C. & Amini, J. Arbitrary waveform generator for quantum information processing with trapped ions. *Rev. Sci. Instrum.* **84**, 033108–033108–6 (2013).
37. QuTiP: quantum tool box in PYTHON. http://qutip.org/ (2016).
38. Johnson, K. G. et al. Active stabilization of ion trap radiofrequency potentials. *Rev. Sci. Instrum.* **87**, 053110 (2016).
39. Harty, T. *High-Fidelity Microwave-Driven Quantum Logic in Intermediate-Field 43Ca+*. PhD thesis, Oxford (2013).
40. Choi, T. et al. Optimal quantum control of multimode couplings between trapped ion qubits for scalable entanglement. *Phys. Rev. Lett.* **112**, 190502 (2014).
41. Milne, A. R. et al. Phase-modulated entangling gates robust against static and time-varying errors. Preprint at http://arxiv.org/abs/1808.10462 (2018).
42. Hite, D. A. et al. 100-fold reduction of electric-field noise in an ion trap cleaned with in situ argon-ion-beam bombardment. *Phys. Rev. Lett.* **109**, 103001 (2012).
43. Ballance, C. J. *High-Fidelity Quantum Logic in Ca+*. Springer Theses (Springer International Publishing, Cham, 2017). https://doi.org/10.1007/978-3-319-68216-7.
44. Hayes, D. et al. Coherent error suppression in multiqubit entangling gates. *Phys. Rev. Lett.* **109**, 020503 (2012).

Chapter 5

Amplitude modulated entangling gates

In the previous chapter, we demonstrated that the experimental setup presented is suitable to produce maximally entangled states of two ions' spin states. We also found out that all main error sources are connected to the ions' motion. In this chapter, we discuss quantum control through the implementation of Mølmer-Sørensen entangling gates with amplitude modulation. This approach allows for a more robust dynamic against motional mode fluctuations, leading to an improvement of the gate fidelity. This work has been published in the peer-reviewed article **P5** [ZHM+19] reported in Sec. 5.5 at the end of this chapter.

5.1 Phase space displacement

The entangling gate uses a transient excitation of the shared ion motion to mediate the required spin-spin coupling. It is therefore beneficial to analyze the Mølmer-Sørensen interaction in the motional phase space of the selected motional mode. Please note that, in the following discussion, we adopt a different formalism than in article **P5**. More details on the original formalism can be found in the appendix B.1.
By rewriting the Hamiltonian shown in Eq. 4.9, the Mølmer-Sørensen interac-

tion can be expressed[7] as:

$$H_{\mathrm{MS}} = i\hbar S_x \sum_{k=1}^{3N} \left(\gamma_k^j a_k^\dagger - \gamma_k^{j*} a_k\right) \quad . \tag{5.1}$$

Where $\gamma_k^j = -i\frac{\Omega_k^j}{2} e^{-i(\delta_k t+\varphi)}$, $S_x = \sum_{j=1}^{N}\left(\sigma_j^+ + \sigma_j^-\right) = \sum_{j=1}^{N}\sigma_j^x$ and Ω_k^j is the Mølmer-Sørensen Rabi rate on ion j in motional mode k. For simplicity, we restrict the discussion to a single motional mode, to $N = 2$ and define $\Omega_k^j = \Omega$, which allows us to write $\gamma(t) = -i\frac{\Omega}{2}e^{-i\delta t}$. The time evolution of the system undergoing the interaction is given by the propagator $U(t)$:

$$U(t) = e^{S_x\left(\alpha(t)a^\dagger - \alpha^*(t)a\right)} e^{iS_x^2 \mathrm{Im}(\Phi(t))} \quad , \tag{5.2}$$

with

$$\alpha(t) = \int_0^t \gamma(x)dx \tag{5.3}$$

$$\Phi(t) = \int_0^t \gamma(x)\int_0^x \gamma^*(y)dydx \quad . \tag{5.4}$$

The first exponential term of Eq. 5.2 is a state dependent displacement operator in the phase space of the harmonic oscillator with coordinates $\mathrm{Re}(\alpha)$ and $\mathrm{Im}(\alpha)$. These coordinates can be converted to the dimensionless position and momentum operators, as described in appendix B.1. The second exponential term is responsible for the entangled state generation. A geometric phase gate is achieved when $\alpha(\tau) = 0$ and $\mathrm{Im}(\Phi(\tau)) = -\pi/8$. In this case Eq. 5.2 simplifies to:

$$U(\tau) = e^{-i\frac{\pi}{8}S_x^2} \quad . \tag{5.5}$$

In case of a 'square' pulse, which is defined as Ω constant from $t = 0$ to $t = \tau$, we obtain:

$$\alpha(t) = \frac{\Omega}{2\delta}\left(e^{-i\delta t} - 1\right) \tag{5.6}$$

$$\mathrm{Im}(\Phi(t)) = \frac{\Omega^2}{4\delta^2}\left(\sin(\delta t) - \delta t\right) \quad . \tag{5.7}$$

As stated in Sec. 4.3 there are multiple values of δ and τ for which a maximally entangled state is produced. Given a fixed value of Ω, the necessary conditions

[7] When comparing to the original notation of [MS99, SM00], note that $S_\xi = 2J_\xi$.

are fulfilled when $\tau = \frac{2\pi K}{\delta}$ and $\delta = 2\Omega\sqrt{K}$ with $K \in \{1, 2, ..\}$. Figure 5.1 shows the action of the displacement operator in phase space when these conditions are respected,. It shows circular trajectories with a radius that decreases as $K^{-\frac{1}{2}}$. The integer K therefore defines the number of closed loops performed by the harmonic oscillator in phase space while keeping the enclosed area constant.

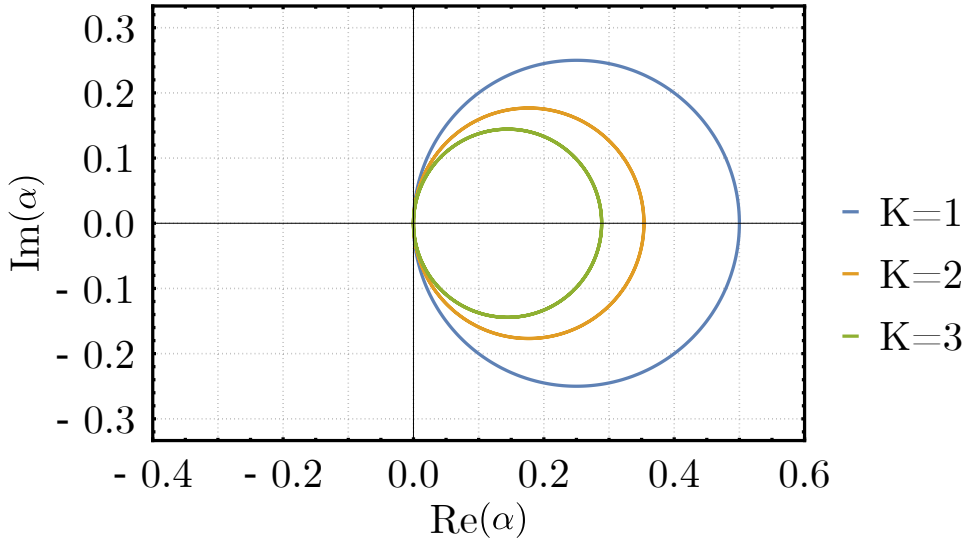

Figure 5.1: Phase space trajectory of a selected motional mode of a two-ion crystal in case a Mølmer-Sørensen interaction driven by a 'square' pulse.

5.2 Quantum control

There are numerous methods for quantum control in case of entangling gate operations. In Chapter 4 and in the previous section, we considered the simple case of the so-called 'square' pulse, i.e. constant value of Ω in the interval $t \in [0, \tau]$ and 0 otherwise. As a matter of fact, the requirements $\alpha(\tau) = 0$ and $\mathrm{Im}(\Phi) = -\frac{\pi}{8}$ can be fulfilled by different functions $\gamma(t)$. The purpose of quantum control methods is to design $\gamma(t)$ such that the entangling gate operation is optimized despite the presence of experimental error sources. The methods reported in the following address the detrimental effects connected to motional mode instabilities during the Mølmer-Sørensen interaction. Other sources of error, such as decoherence or qubit frequency shifts, require different experimental protocols, generally not connected to the phase space displacement term but to additional σ^z terms added to the interaction Hamiltonian [BSPR12, IV15, HSA+16, MRS+17, ACP+18, APSC20].

5.2.1 Walsh modulation

One approach to compensate motional errors is the so-called Walsh modulation [HCD+12]. This methods relies on inverting the direction of the phase space loops in a controlled way to minimize the distance between $\alpha(0)$ and $\alpha(\tau)$ in the presence of errors. This approach can be implemented by inverting the phase of the Mølmer-Sørensen gate drive at specific instants of time or by applying a global π pulse to invert the spin states. These instants, at which the phase or the spin states are inverted, follow the Walsh function $W(2(k-1)+1, x)$ [HCD+12]. They generally coincide with the times at which the loops in phase space are closed. Examples of pulses and times used are shown in Fig. B.1 a). A Walsh modulation of order k requires the same δ and τ as a 'square' pulse gate with 2^k loops. The function $\gamma(t)$ can be rewritten as:

$$\gamma(t) = -iW(2(k-1)+1, t/\tau)\frac{\Omega}{2}e^{-i\delta t} \quad . \tag{5.8}$$

An example of the phase space trajectory for a Walsh order $k = 1$ is shown in Fig. 5.2.

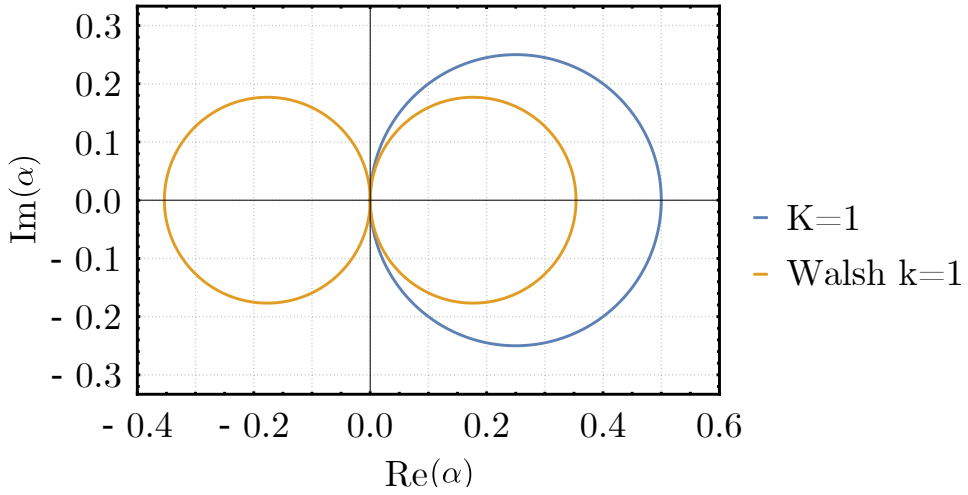

Figure 5.2: Phase space trajectory of a selected motional mode of a two-ion crystal in case a Mølmer-Sørensen interaction with Walsh modulation is applied.

5.2.2 Multi-tone gate

Another approach to reduce the effects of motional errors is the so-called multi-tone gate [HM16] which has been recently demonstrated in both laser and

microwave-driven operations [SSM+18, WWC+18]. This approach relies on the application of a multi-chromatic driving field that can be described as a sum of bichromatic fields with specific relative amplitudes. The tones, or frequencies, of each field are given by $\omega_j = \omega_0 \pm (\omega_r + j\delta)$ where $j \in \{1, .., k\}$ and k identifies the number of tones used. The function $\gamma(t)$ can be written as:

$$\gamma(t) = \sum_{j=1}^{k} -ic_j \frac{\Omega}{2} e^{-ij\delta t} \quad , \tag{5.9}$$

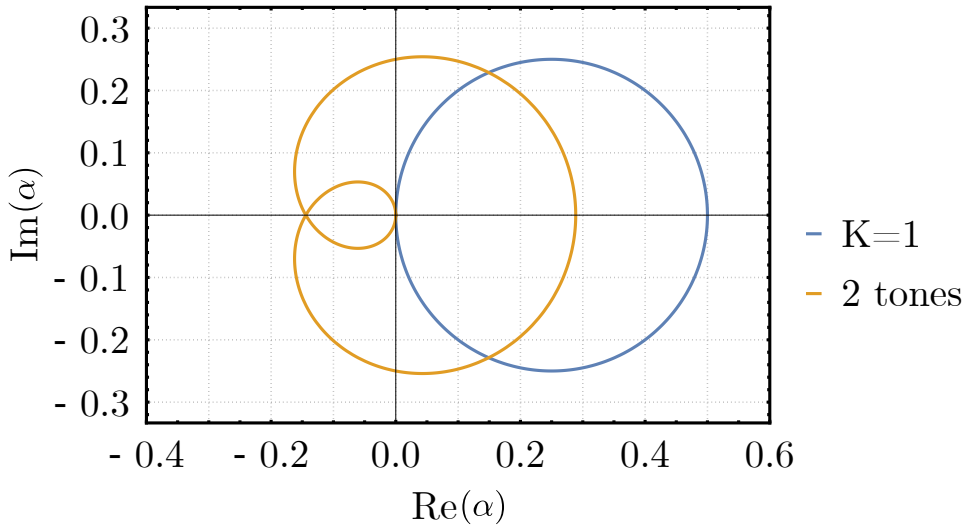

Figure 5.3: Phase space trajectory of a selected motional mode of a two-ion crystal in case a Mølmer-Sørensen interaction with two tones is applied.

where c_j identifies the relative tone amplitude. Fig. 5.3 shows an example of the phase space trajectory obtained with a two-tone gate when using the relative amplitudes listed in [HM16, WWC+18]. The gates resulting from this set, after appropriately scaling Ω, require the same δ and τ as a 'square' gate with a $K = 1$ loop. A similar approach which makes use of time-dependent variation of the detuning [8] $\delta(t)$, instead of multiple frequencies, has also been investigated [LB18, LLF+18].

5.2.3 Phase modulation

An alternative approach is the phase modulation method [MEH+20, GB15], where the phase of the gate driving field, instead of the frequency, is regulated.

[8] Such an approach would then be defined as frequency modulation.

The function $\gamma(t)$, in this case, becomes:

$$\gamma(t) = \sum_{j=1}^{k} -ir_j(t, t_j)\frac{\Omega}{2}e^{-i\delta t} \quad , \tag{5.10}$$

where $r_j(t, t_j) = \Theta(t - t_{j-1})\Theta(t_j - t)e^{-i\phi_j(t)}$ and $\Theta(t)$ is the Heaviside theta function. The function $r_j(t, t_j)$ produces a time-dependent variation of the gate phase $\phi_j(t)$ in the interval $t \in \{t_{j-1}, t_j\}$. Note that the work of [MEH+20], which uses constant phase values in each interval, requires numerical optimization to identify the best phase values $\phi_j(t)$ based on experimental conditions. Therefore, depending on the number of chosen intervals k and the phases ϕ_j many different phase space trajectories can be performed. For this reason this quantum control method does not have a typical trajectory to be shown.

5.2.4 Amplitude modulation

The amplitude modulation method is based on the concept of regulating the amplitude of the field driving the gate interaction [ZMD06, Roo08, CDM+14, SIHL14, PMGL+17] and therefore the gate Rabi rate Ω and has been previously applied to laser-driven gates [SBT+18, FOL+19]. As for the other quantum control methods, the purpose is to obtain resilience against motional mode frequency noise by engineering appropriately the traversed phase space trajectory. For this method, the function $\gamma(t)$ becomes:

$$\gamma(t) = -iP(t)\frac{\Omega}{2}e^{-i\delta t} \quad , \tag{5.11}$$

where the pulse envelope $P(t)$ is a function normalized to 1 which describes the gate drive modulation. In this thesis, we consider the case of $P(t) = \sin^n(\beta t)$, but other pulse shapes can be used. Since the gate drive needs to be turned on at the beginning and off at the end of the applied gate pulse, there is a a natural constraint in $P(0) = P(\tau) = 0$ which directly gives the condition $\beta\tau = m\pi$. The integer $m \in \{1, 2, 3, ..\}$ defines the number of oscillations, single pulses, present in the complete pulse envelope.

As in the other approaches there are multiple combination of δ and τ for which the propagator $U(\tau)$ produces the maximally entangled state $|\Psi\rangle$. For the single pulse case, i.e. $m = 1$, these conditions are achieved for $\delta_k = 2\pi(k + n/2)/\tau_k$ with k being the integer identifying the phase space trajectory order. Fig. 5.4 shows an example of phase space trajectory for $m = 1$, $n = 2$ and $k = 1$. Further trajectories can be found in the appendix in Fig. B.2. An

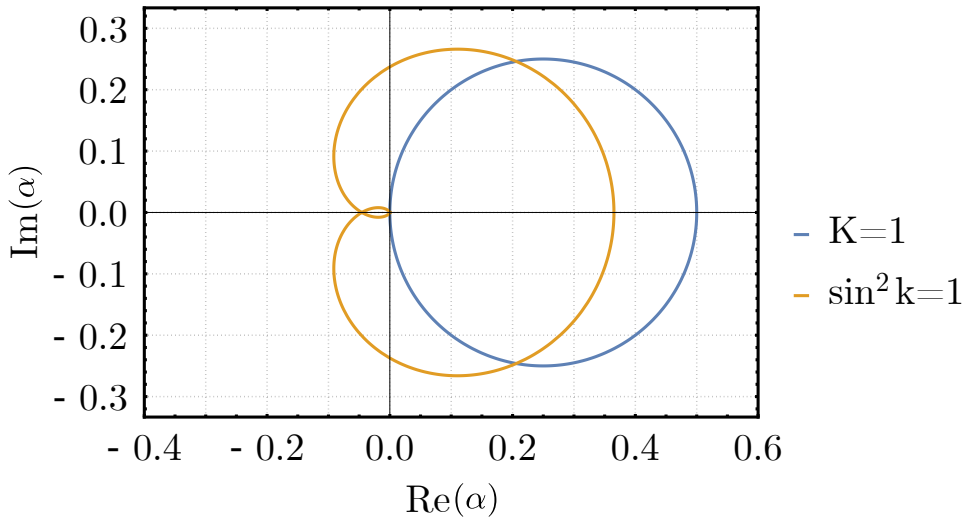

Figure 5.4: Phase space trajectory in case a Mølmer-Sørensen interaction with first order amplitude modulation with $P(t) = \sin^2(\pi t/\tau)$ is applied.

example of pulses and times used is shown in Fig. B.1 b). Higher orders have trajectories that do not move much from the phase space origin and perform multiple windings around it to enclose the same area. By limiting the distance from the origin it can be shown that even in the presence of errors the relation $|\alpha(\tau)| \approx 0$ is satisfied, providing robustness against motional errors.

5.3 Demonstration of amplitude modulation

To demonstrate the resistance of the amplitude modulated microwave gate against radial mode fluctuations, we artificially inject noise of different amplitudes in the pseudopotential as described in Subsec. 5.3.1. The robustness is demonstrated by a comparison of the resulting gate fidelities $\mathcal{F}$ between the 'square' pulse and the amplitude modulated scheme at different noise levels, as described in Subsec. 5.3.2. After passive stabilization of the radial modes, detailed in Subsec. 5.3.3, we demonstrate the highest achieved fidelity in our system. To this end, the collected fluorescence data has been evaluated to extract the required populations using different methods known in the field, as discussed in Subsec. 5.3.4.

At the hardware stage, the amplitude modulation of the involved microwave pulses is implemented via a digital PI regulator [HMF+18] which controls the

microwave amplifiers' output through a fast RF multiplier[9], placed before the amplifiers. The error signal for the PI regulator is generated by subtracting the output signal of an RF envelope detector[10] with a reference voltage provided from the experiment DAC [BWB+13, Bow15]. With this setup, amplitude modulation can be performed with a bandwidth limit of about 618 kHz. The complete microwave setup is described in detail in Sec. 4.7 of [Hah19].

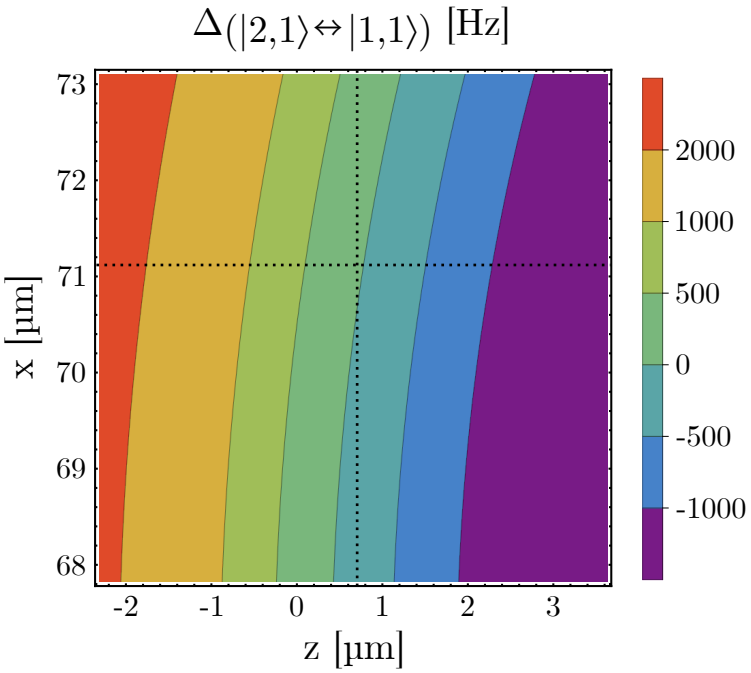

Figure 5.5: Differential AC Zeeman shift generated from the 'ConsTrap' MWM conductor when subjected to the Mølmer-Sørensen gate drive. The magnetic field pattern is the one resulting from the FEM simulation model centered at the crossing point of the dashed lines.

It should be noted that the presence of a finite residual B field in the oscillating quadrupole produces a differential AC Zeeman shift, given by the two opposite shifts from each driving sideband at frequency ω_B and ω_R, respectively. The resulting shift of the qubit frequency is proportional to the microwave power, i.e. to the square of the Mølmer-Sørensen Rabi rate. This effect is considered by adding the term:

$$H_Z = \hbar P^2(t) \frac{\Delta}{2} \sum_j \sigma_j^z \quad , \tag{5.12}$$

[9] ADL5391
[10] ADL5511

to the full system Hamiltonian in Eq. 4.9 where Δ is the qubit frequency shift measured when the gate drive is at its maximum, i.e. $P = 1$. The introduction of this term can affect the fidelity of the entangling operation. A more detailed discussion is presented in Sec. 5.4.

As described in Sec. 2.4, the AC Zeeman shift depends not only on the field amplitude but also on its polarization and frequency. The same holds true in case of differential shifts originating from two oscillating fields. Fig. 5.5 shows the estimated differential shift on the qubit transition from the gate drive fields obtained from the FEM simulations. To drive the gate, it is desirable to have the two ions in a position in the radial plane where $\Delta = 0$, see Sec. 5.4 for further details. The calculations based on the FEM simulation model indicate how such a condition is achieved not in a single point but in a one-dimensional manifold. The correct $\Delta = 0$ position can be found by performing the same Ramsey experiment described in Sec. 2.4, but where the bichromatic gate drive is used instead of a single sideband. To reach this position, where we estimate $\Delta \leq 5\,\mathrm{Hz}$, it is necessary to displace the ions radially by about $1.5\,\mu\mathrm{m}$ from the pseudopotential minimum. All amplitude modulated gates presented in the following are performed at this position. We assume that most of the shift is due to the difference between the actual minimum of the magnetic field generated by the 'ConsTrap' MWM conductor, reported in Tab. 4.1, and the pseudopotential minimum.

Considering an expected increase in the entangling gate fidelity, the single-qubit operations have been implemented using composite pulse sequences to not be limited by the state preparation and imperfect analysis pulse. Specifically, the 5 pulse sequence for the $\pi/2$ analysis pulse [TV11] and the U5a sequence for π pulses [GSHV14] have been used. The reason of this last choice is the better performance of the U5a sequence against errors in the single-pulse duration when compared to sequence U5b.

5.3.1 Noise injection setup

To increase the fluctuations of the ion motional mode, we introduce noise in the voltage which is sent to the coaxial resonator that drives the RF electrode, causing a direct modulation of the harmonic potential. The schematic of the noise injection setup is shown in Fig. 5.6. The noise is produced by an arbitrary

waveform generator[11] and regulated by a DAC (digital analog converter) signal through an RF circuit which acts as a multiplier on the noise amplitude. It is then sent to the amplitude modulation port of the RF source[12]. By controlling the DAC signal, the injected noise amplitude can be precisely adjusted. The characterization of the injected noise in the radial mode is obtained with the experimental sequence described in details in Sec. 5.3.3.1 of [Hah19], in the following the procedure is explained. For a given noise amplitude, the motional mode of interest is cooled near the ground state and subsequently excited by a weak oscillating electric field superimposed on one of the DC electrode trap voltages. The motional excitation can then be converted into a spin state change by means of a red sideband pulse, driven by Raman lasers, which can then be detected following the standard read-out procedure. The FWHM of the motional mode ω_r is obtained by varying the frequency of the exciting electric field.

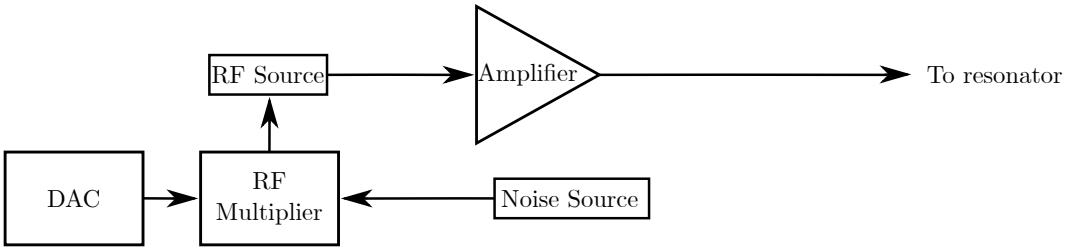

Figure 5.6: Experimental setup for noise injection in the radial modes. The generated noise amplitude is regulated by a controllable DAC signal through an RF multiplier. The noise signal is then sent to the amplitude modulation port of the RF source. The now noisy RF drive is then amplified and sent to the step-up resonator.

5.3.2 Noise injection results

In the peer-reviewed publication **P5**, Fig. 3 b) shows a theoretical comparison of the gate infidelity for different quantum control methods. An extended comparison, which includes additional protocols, is presented in Fig. 5.7. The analytical model employed[13] in the comparison estimates the Bell state fidelity using motional mode frequency distribution from the FWHM of the motional mode ω_r, the gate Rabi rate Ω, the gate detuning δ, the gate time τ and the initial motional occupancy of the motional mode $\bar{n}$ as parameters. The model

[11] Agilent 33250A

[12] HP8640B

[13] The model has been developed by Marius Schulte and will be featured in his PhD thesis.

aims only at quantifying the effect of the motional mode noise on the gate fidelity, therefore it does not account for other error sources such as anomalous motional heating or slow mode drifts. The parameters used for this comparison are the same reported in the publication, i.e. $\Omega = 1.18\,\text{kHz}$ and $n_{\text{in}} = 0.4$. The detuning δ, and gate time τ, are chosen specifically for each method to obtain $\alpha(\tau) = 0$ and $\text{Im}(\Phi(\tau)) = -\frac{\pi}{8}$ in absence of errors. The energy dissipated in the MWM conductor is assumed to be the same for all schemes. Since the energy is proportional to the square of the current flowing in the conductor, we aim to equalize the values of $E = \sum_j \int_0^\tau \Omega_j^2(t)dt$ where j identifies the number of active fields in the gate drive.

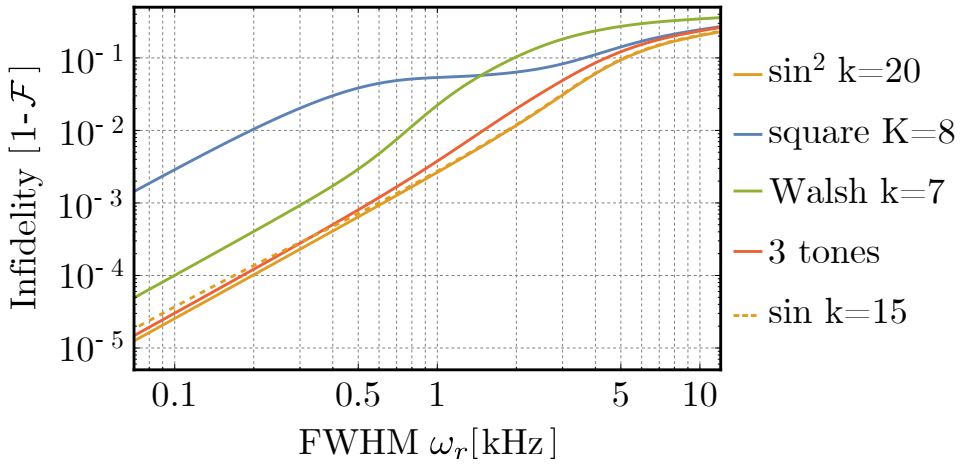

Figure 5.7: Comparison of fidelities as a function of noise present in the ions motional mode for different quantum control schemes using an analytical model. For a better comparison, all schemes are constrained to dissipate approximately the same energy.

For small noise amplitudes the performance of the $\sin^2$ $k = 20$ gate, the $k = 3$ multi-tones gate and the sin $k = 15$ gate appear comparable, with infidelities values of $< 10^{-4}$. It is essential to note, however, that the gate time τ is not the same for all three schemes. The sin $k = 15$ gate, due to the different pulse area, has the advantage of being faster, $\tau = 2361\,\mu\text{s}$, when compared to the equivalent energy $\sin^2$ $k = 20$ gate pulse, $\tau = 3178\,\mu\text{s}$. The simulation has also been performed for a $\sin^3$ $k = 24$ pulse, which requires $\tau = 3831\,\mu\text{s}$. However, the data for this method has not been included in the figure since it appears indistinguishable from the values of the $\sin^2$ pulse. The detunings δ, required to perform the three $\sin^n$ gate pulses, are all within 100 Hz at about $\delta = 6.6\,\text{kHz}$. For the $k = 3$ multi-tones gate, the Rabi rate has been increased by a factor of 4 in order to match the desired energy, resulting in a gate time

of $\tau = 424\,\mu$s, equal to the one for a $K = 1$ 'square' pulse gate. The third order Walsh modulation scheme gives higher values of infidelity compared to the previous methods but outperforms the $K = 8$ 'square' pulse gate by more than one order of magnitude. Interestingly, the condition is inverted in case of large noise amplitudes where the third order Walsh modulation performs worse than the standard 'square' pulse scheme.
The best quantum control method must be chosen in accordance with the specific experimental constraints. In our case, we chose a $\sin^2$ gate which performs well at all noise levels and has the feature, contrary to the sin gate, that the derivatives of $P(t)$ are equal to zero at $t = 0$ and $t = \tau$. This is desirable since it provides a 'soft' start [SSB+19] and avoids unwanted motional excitation from microwave electric pseudopotential kicks [WOC+13]. Furthermore we prefer amplitude modulation over the multi-tone approach because, although it is slower, in the near-field approach, multiple tones could lead to undesirable frequency mixing effects in the presence of amplifiers nonlinearities.

The experimental comparison between a $K = 7$ 'square' loop and a $\sin^2$ $k = 17$ pulse is shown in Fig. 3 a) of peer-reviewed publication **P5**. Each datapoint has been analyzed using the sum of weighted Poissonians, the description of which can be found in Sec. 4.5. The number of loops and the order of the $\sin^2$ gate have been chosen to keep the energy dissipated in the MWM conductor equal for both cases. In order to control the total energy dissipated, no warm-up pulse has been employed, differently to the procedure described in Sec. 4.7. For a chosen noise amplitude, measurements were taken in an interleaved way to ensure the same experimental conditions. Particular attention should be given to the slow drift of ω_r. An example of such an effect is shown in Fig. 5.8, where we show the measurements at a FWHM of ω_r of 272 ± 24 Hz given in Fig. 3 a) of **P5**. The effect during data acquisition for the $K = 7$ 'square' pulse gate is presented in Fig. 5.8 a). A change of more than 10% in the $P_{\uparrow\downarrow,\downarrow\uparrow}$ population at the oscillation minima was observed due to the slow drift of ω_r. Fig. 5.8 b) shows the behavior under the same conditions using the $\sin^2$ $k = 17$ pulse gate. The change in the $P_{\uparrow\downarrow,\downarrow\uparrow}$ population minimums is reduced to less than 5% due to the robustness of the amplitude modulated gate against motional mode changes.

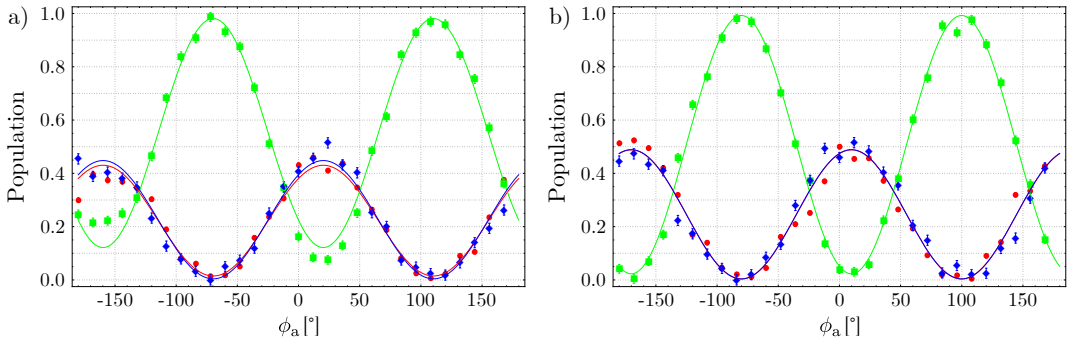

Figure 5.8: Comparison of noise injection results at a FWHM of the motional mode of 272(24) Hz. Population variation as a function of $\pi/2$ analysis pulse phase. Population in $|\downarrow\downarrow\rangle$ ($P_{\downarrow\downarrow}$; red circles), $|\uparrow\downarrow\rangle$ and $|\downarrow\uparrow\rangle$ ($P_{\uparrow\downarrow,\downarrow\uparrow}$; green squares) and $|\uparrow\uparrow\rangle$ ($P_{\uparrow\uparrow}$; blue diamonds). Solid lines represents fits to the populations. a) $K = 7$ 'square' pulse gate, $\mathcal{F} = 0.869(13)$. b) $\sin^2$ pulse with $k = 17$, $\mathcal{F} = 0.973(10)$.

5.3.3 Stabilized RF setup

To improve the gate fidelity, as detailed in Sec. 4.7, one can reduce the ions' radial modes fluctuation and drift by stabilizing the signal which generates the confining pseudopotential. The radial mode frequency ω_r depends, given a stable axial trapping potential, on the frequency and amplitude of the signal applied to the RF electrode. We have observed sufficient relative stability between the frequency of the RF source and the step-up resonator to not require frequency stabilization of either. It is instead more relevant to stabilize the amplitude of their RF output. In this work, we have chosen a passive stabilization rather than an active one like in [JWCR+16]. Active stabilization has not been considered since the high power microwave signal can couple through the RF electrode and induce errors by being falsely detected as an RF amplitude change.

The schematic of the circuit designed to perform the amplitude stabilization is shown in Fig. 5.9. It is based on the work of T. P. Harty [Har13] and described in the MSc thesis of J. Morgner thesis [Mor20]. The circuit uses a rectifier to change the sinusoidal RF signal into a stable square wave. The rectifier circuit is based on a logic converter[14] with a stable voltage reference[15] and a high stability buffer[16]. The amplitude stabilized square wave signal is

[14] LTC6957-3
[15] LTC6655
[16] LT3042

then converted back into a sinusoidal form by a home-built bandpass filter. To compensate the reduced power of the signal after the filtering stage, the RF signal is amplified with a temperature stabilized amplifier[17]. It is then sent to the step-up transformer which is a coaxial RF resonator partly integrated into, partly attached to our vacuum chamber [Hah19]. The resulting radial modes provided a better short-term stability and FWHM of ω_r compared to what has been observed in the experiments of Sec. 4.6. Long-term stability has been characterized and quantified to a variation of $< 0.1\,\%$ during the day, where most of the drift could be correlated with lab temperature change.

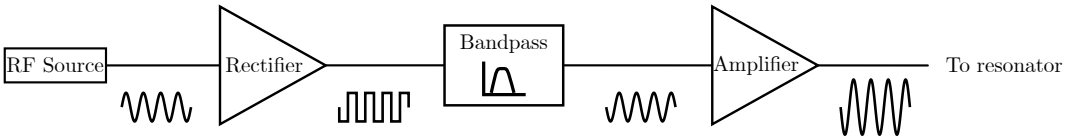

Figure 5.9: Setup implemented to reduce amplitude noise of the RF signal, designed according to [Mor20]. The rectifier converts the RF signal to an amplitude stable square wave. The bandpass filter allows only the relevant frequency to pass, thereby generating an amplitude stable sinusoidal signal.

5.3.4 High fidelity Bell state analysis

In peer-reviewed article **P5** different analysis methods for establishing the fidelity from the fluorescence histograms have been compared. The comparison shows very close agreement between all methods. We were thus able to ensure the high fidelity of our gate operation which proves to be largely independent of the type of data analysis.

The fluorescence data used for all analysis methods consists of two sets of the $\pi/2$ analysis pulse phase scan, where each phase value has been acquired 300 times per scan. The phase sampling is non-linear to maximize data acquisition of the state oscillation at the minimum and maximum of the parity Π, as shown in Fig. 4 of **P5**.
For the first analysis method the three populations, $P_{\uparrow\uparrow}$, $P_{\downarrow\downarrow}$ and $P_{\uparrow\downarrow,\downarrow\uparrow}$, are obtained from each acquired fluorescence histogram using the weighted sum of Poissonians analysis detailed in Sec. 4.5. The reference histograms have been changed from the Ramsey oscillation, Sec. 4.5, to the preparation and

[17]The amplifier was a Minicircuits LHA-13HLN+ that was later exchanged for a more stable spectrum microwave BX3110 following the work described in [Mor20].

measurement of specific states: $|\uparrow\uparrow\rangle$, $|\downarrow\downarrow\rangle$, $(|\uparrow\uparrow\rangle - i\,|\uparrow\downarrow\rangle - i\,|\downarrow\uparrow\rangle - |\downarrow\downarrow\rangle)/2$ and $(|\uparrow\uparrow\rangle + i\,|\uparrow\downarrow\rangle + i\,|\downarrow\uparrow\rangle - |\downarrow\downarrow\rangle)/2$. The state preparation has been done following the description in Sec. 6.6 of [Tan16]. The measurement has been repeated about 2×10^4 times for each state. These states have been selected to obtain reference histograms that are compatible with all the chosen analysis methods. The fidelity is estimated through resampling bootstrap: since for each phase value two measurements are acquired, we randomly divide them in two distinct datasets. From the first artificial dataset we obtain by interpolation, of the populations already gained through the weighted sum of Poissonians analysis, the $P_{\uparrow\uparrow}$ and $P_{\downarrow\downarrow}$ populations. While from the second dataset the parity amplitude $A(\Pi)$ is estimated, enabling therefore the calculation of the Bell state fidelity $\mathcal{F}$ using Eq. 4.13. The procedure is iterated 1000 times, each time producing two new artificial datasets, resulting in the distribution of fidelities shown in blue in Fig. 5.10 a). Due to the presence of constraints[18] in the fitting procedure to obtain $P_{\uparrow\uparrow}$, $P_{\downarrow\downarrow}$ and $A(\Pi)$, the distribution appears to be truncated. The removal of the constraints does not change the estimated fidelity significantly. By iterating the procedure a sufficient amount of times the mean value of $\mathcal{F}$ converges, see Fig. 5.10 b), to $\mathcal{F} = 99.5\%$ with a 68% confidence interval of $[99.3, 99.7]\%$.

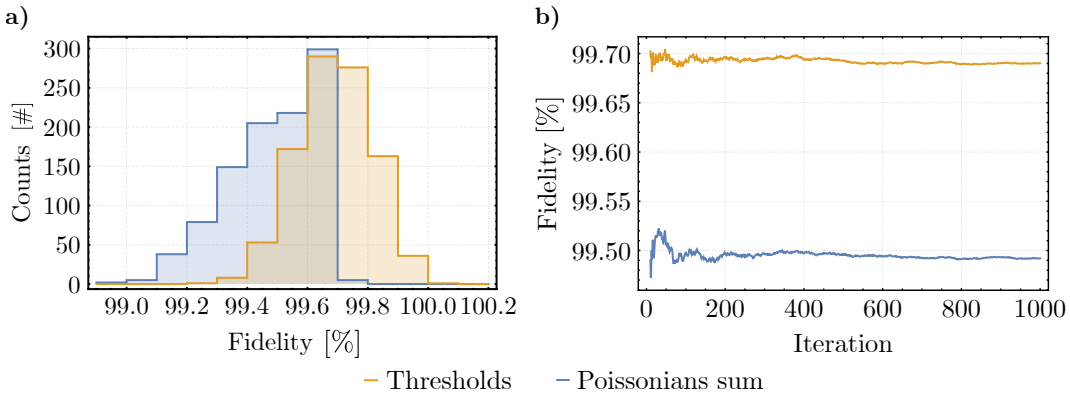

Figure 5.10: a) Distribution of fidelities obtained through resampling bootstrap for state analysis performed with the sum of Poissonians distributions and photon count thresholds methods. b) Mean fidelity for each method as a function of the number of iterations in the bootstrapping.

[18]The constraints impose that in the state oscillation, induced by the $\pi/2$ analysis pulse, all populations are in the interval $0 \leq P \leq 1$ and the parity amplitude in the interval $-1 \leq A(\Pi) \leq 1$.

The second analysis method performs the same resampling bootstrap of the populations as the first one. The difference is that the state populations are obtained by placing appropriate thresholds in the fluorescence histogram as done in [HSA+16]. In this way, the data are split in three separate bins which identify $P_{\uparrow\uparrow}$, $P_{\downarrow\downarrow}$ and $P_{\uparrow\downarrow,\downarrow\uparrow}$, respectively. From the reference histograms, we estimate a SPAM error $\epsilon_{\mathrm{SPAM}} = 1.5(1)\,\%$, using the procedure detailed in appendix C of [Bal17]. This error is added to the fidelity in order to correct for state preparation and measurement errors. In the fidelity distribution obtained through bootstrapping, this addition can lead to cases where $\mathcal{F} > 1$, if the non-corrected fidelity is already close to 1. In the specific case of 1000 bootstrapping iterations, we find a single fidelity value exceeding $\mathcal{F} = 1$ by 4×10^{-6}. In total, the second analysis method using thresholds results in a mean fidelity $\mathcal{F} = 99.7\%$ with a 68% confidence interval of $[99.6, 99.8]\%$.

For the third analysis method, we chose to use the maximum likelihood algorithm described in [KBGK18] and used in [Lin15, LGR+16, GTL+16]. The algorithm estimates the density matrix of the state subjected to the $\pi/2$ analysis pulses. The reference histograms are used to obtain the expected experimental histogram for well-defined states. This method differs from the other in the fact that it makes almost no assumptions on the fluorescence histograms, while the previous two do. The maximum likelihood analysis method resulted in $\mathcal{F} = 99.2\%$ with a 68% confidence interval of $[99.1, 99.7]\%$, using a training fraction of 20% and a bootstrap of 1000.

Considering the large errors connected to the state detection, a future implementation of randomized benchmarking protocols [KLR+08, GMT+12, EWP+19, BBG+20] could give a better determination of the error per gate operation.

It should be noted that, since these protocols rely on the implementation of long sequences of random gate operations, an auxiliary ion of a different species is required for sympathetic cooling. In this way, issues affecting the fidelity connected with the sequence being too long, like the variation of the ions' motional state due to heating, can be avoided.

5.4 Error sources

In the last section, we showed that the Bell state fidelity of the $\sin^2$ $k = 17$ amplitude modulated gate is in the 10^{-3} region for all the three considered analysis methods. As reported in the peer-reviewed article **P5**, the errors connected to the ion motion are reduced when compared to the work done in publication **P4**. The values are summarized in Tab. 5.1.

Effect	Infidelity $[1 - \mathcal{F}]$
Heating rate	2×10^{-4}
Motional occupancy	1×10^{-5}
Spectator mode	5×10^{-4}
Frequency 'chirp'	$< 1 \times 10^{-5}$

Table 5.1: Errors connected to the ion motion as detailed in **P5**.

The reported infidelities have been estimated using the same considerations as in Sec. 4.7. The anomalous heating contribution considers $\dot{\bar{n}} = 8$ phonons per second while the motional occupancy considers an average phonon number of $\bar{n} = 0.4$ phonons. For the infidelity contributions due to off-resonant coupling to spectator modes, we considered only the closest motional center-of-mass mode[19] which is detuned by about 96 kHz and has a mean phonon number of $\bar{n} = 1$ after Doppler cooling while heating up with a rate of 343 phonons per second. The infidelity contribution from the frequency 'chirp' is not a single value but is reported as a boundary since it results from multiple simulations. Independent of the assumed 'chirp' function and its amplitude, it was always possible to change the gate detuning δ to fully compensate its infidelity contribution. The most extreme tested cases include a linear or a $P^2(t)$ function with a peak frequency variation of 1 kHz. This peak value was chosen to simulate an 'extreme' case since, as in **P4**, the maximum 'chirp' peak shift is expected to be about 300 Hz. Even in these 'extreme' cases, the infidelity contribution of the 'chirp' can be made negligibly small upon correction of the detuning δ.

[19]The other motional modes are separated by more than 400 kHz and are therefore assumed not to be of the same importance.

We therefore assume that most of the remaining gate error is uncorrelated from the ions' motional state and connected to the internal states. As stated in Sec. 5.3 the differential AC Zeeman shift is crucial. Fig. 5.11 shows how the addition of the H_Z term of Eq. 5.12 can contribute to the gate infidelity.

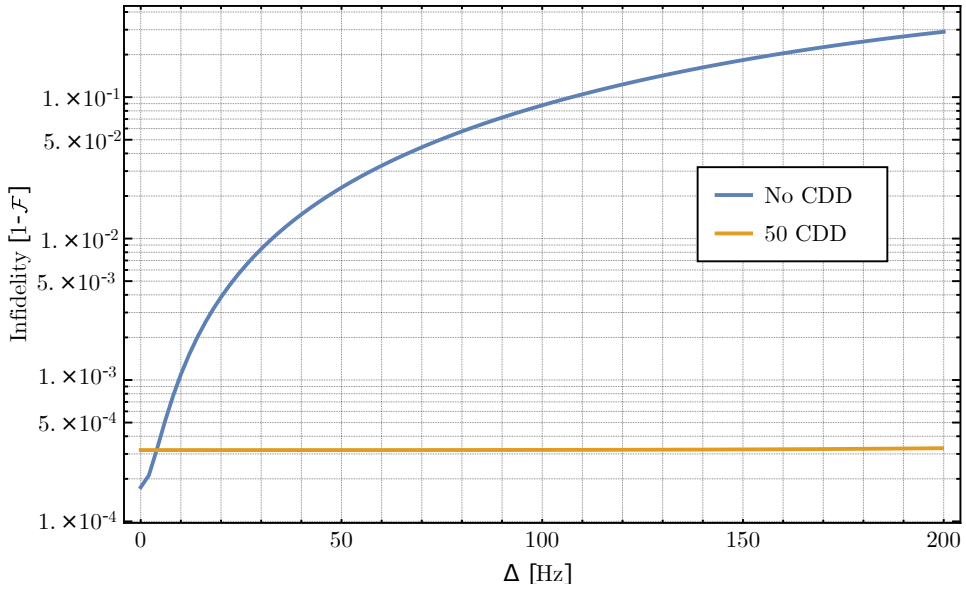

Figure 5.11: Effect of the time-dependent AC Zeeman shift on the gate infidelity and its contribution in a scheme including Continuous Dynamical Decoupling.

A value of $\Delta \neq 0$ can occur due to a change of the experimental conditions or errors in the calibration. As depicted in the figure, this can have a strong impact on the gate performance. For example, a shift of $\Delta \approx 23\,\mathrm{Hz}$, in our case, could already introduce an infidelity of 5×10^{-3}. Other effects which can affect the internal states could be: a distinct frequency shift for each ion, due to a misalignment of the ions' crystal from the axial direction, or a time-dependent shift, due to the ions micromotion. Both effects are intrinsic to the microwave near-field approach and are given by the spatial dependence of the AC Zeeman shift as explained in Sec 5.3.

The influence of all the effects that change the qubit transition frequencies can be reduced by using dynamic decoupling protocols. A protocol of this kind, already used successfully in a microwave near-field experiment, is continuous dynamic decoupling [BSPR12, HSA+16, Sep16]. In this protocol, a carrier drive continuously excites the qubit transition during the gate operation. The corresponding Hamiltonian term is:

$$H_{\mathrm{CDD}} = \frac{1}{2}\Omega_{\mathrm{CDD}} \sum_{j=1}^{2} \sigma_j^x \tag{5.13}$$

where Ω_{CDD} is the chosen carrier Rabi rate, which should be engineered such that no effective state transition can happen at the end of the gate interaction.

By performing 50 state oscillations between $|\uparrow\uparrow\rangle$ and $|\downarrow\downarrow\rangle$ in the time interval τ with a Ω_{CDD} equal to $2\pi 50/\tau$, the gate infidelity can be reduced to 3×10^{-4} and can be considered nearly independent of Δ, as shown by the orange curve in Fig. 5.11.

5.5 P5: Robust and Resource-Efficient Microwave Near-Field Entangling $^{9}Be^{+}$ Gate

Authors: **G. Zarantonello**, H. Hahn , J. Morgner , M. Schulte, A. Bautista-Salvador, R. F. Werner, K. Hammerer and C. Ospelkaus.

Journal: Physical Review Letters

DOI: 10.1103/PhysRevLett.123.260503

Author contribution: **GZ** and JM performed the measurements. **GZ** and HH analyzed the data. ABS produced the ion trap. **GZ** and MS studied the feasibility of amplitude modulation with microwaves. **GZ**, MS, RFW and KH contributed the numerical simulations. CO devised the experiment plan. All authors participated in the realization of the manuscript.

Robust and Resource-Efficient Microwave Near-Field Entangling $^{9}Be^{+}$ Gate

G. Zarantonello,[1,2] H. Hahn,[1,2] J. Morgner,[1,2] M. Schulte,[3] A. Bautista-Salvador,[1,2,4] R. F. Werner,[5] K. Hammerer,[3] and C. Ospelkaus[1,2,4,*]

[1]*Institut für Quantenoptik, Leibniz Universität Hannover, Welfengarten 1, 30167 Hannover, Germany*
[2]*Physikalisch-Technische Bundesanstalt, Bundesallee 100, 38116 Braunschweig, Germany*
[3]*Institut für Theoretische Physik und Institut für Gravitationsphysik (Albert-Einstein-Institut), Leibniz Universität Hannover, Appelstrasse 2, 30167 Hannover, Germany*
[4]*Laboratorium für Nano- und Quantenengineering, Leibniz Universität Hannover, Schneiderberg 39, 30167 Hannover, Germany*
[5]*Institut für Theoretische Physik, Leibniz Universität Hannover, Appelstrasse 2, 30167 Hannover, Germany*

(Received 15 October 2019; published 26 December 2019)

Microwave trapped-ion quantum logic gates avoid spontaneous emission as a fundamental source of decoherence. However, microwave two-qubit gates are still slower than laser-induced gates and hence more sensitive to fluctuations and noise of the motional mode frequency. We propose and implement amplitude-shaped gate drives to obtain resilience to such frequency changes without increasing the pulse energy per gate operation. We demonstrate the resilience by noise injection during a two-qubit entangling gate with $^{9}Be^{+}$ ion qubits. In the absence of injected noise, amplitude modulation gives an operation infidelity in the 10^{-3} range.

DOI: 10.1103/PhysRevLett.123.260503

Trapped ions are a leading platform for scalable quantum logic [1,2] and quantum simulations [3]. Major challenges toward larger-scale devices include the integration of tasks and components that have been so far only demonstrated individually, as well as single- and multiqubit gates with the highest possible fidelity to reduce the overhead in quantum error correction. Microwave control of trapped-ion qubits has the potential to address both challenges [4,5], as it allows the gate mechanism, potentially including control electronics, to be integrated into scalable trap arrays. Because spontaneous emission as a fundamental source of decoherence is absent and microwave fields are potentially easier to control than the laser beams that are usually employed, microwaves are a promising approach for high-fidelity quantum operations. In fact, microwave two-qubit gate fidelities seem to improve more rapidly than laser-based gates. However, observed two-qubit gate speeds of laser-based gates [6,7] are still about an order of magnitude faster than for microwave gates [8–10]. This makes gates more susceptible to uncontrolled motional mode frequency changes, as transient entanglement with the motional degrees of freedom is the key ingredient in multiqubit gates for trapped ions. As other error sources have been addressed recently, this is of growing importance. Merely increasing Rabi frequencies may not be the most resource-efficient approach, as it will increase energy dissipation in the device. A more efficient use of available resources could be obtained using pulse shaping or modulation techniques. In fact, a number of recent advances in achieving high-fidelity operations or long qubit memory times have been proposed or obtained by tailored control fields. Examples include pulsed dynamic decoupling [11], Walsh modulation [12], additional dressing fields to increase coherence times [13], phase [14], amplitude [15–20], and frequency modulation [21], as well as multitone fields [22–24]. In many cases, these techniques lead to significant advantages. For multiqubit gates, one mechanism is to optimize the trajectory of the motional mode in phase space for minimal residual spin-motional entanglement in case of experimental imperfections. This effectively reduces the distance between the origin and the point in phase space at which the gate terminates in case of errors.

Here we propose and implement amplitude modulation for near-field microwave two-qubit entangling gates to make operations more resilient to normal mode frequency fluctuations, one of the dominant error sources in present experiments [8], without increasing the electrical energy cost per gate. We consider the bichromatic gate mechanism discussed in Refs. [25–27]. In a notation similar to Ref. [28], simultaneous application of blue and red motional sidebands of the qubit transition with detuning δ yields the propagator $U(t) = e^{-iA(t)S_y^2} e^{-iG(t)S_y x} e^{-iF(t)S_y p}$, where x and p are dimensionless position and momentum operators, $S_y = 1/2(\sum_j \sigma_j^y)$, and σ_j^y is the Pauli matrix for ion j. We have

$$\begin{aligned} F(t) &= -\sqrt{2}\int_0^t \Omega(t')\cos(\delta t')dt', \\ G(t) &= -\sqrt{2}\int_0^t \Omega(t')\sin(\delta t')dt', \\ A(t) &= \sqrt{2}\int_0^t F(t')\Omega(t')\sin(\delta t')dt', \end{aligned} \tag{1}$$

where $\Omega(t)$ is the time-dependent gate Rabi frequency. For eigenstates of S_y, $U(t)$ effectively leads to trajectories in

phase space with dimensionless coordinates $G(t)$ and $F(t)$ for the harmonic oscillator of the motional mode. A closed trajectory is reached for $F(\tau) = G(\tau) = 0$, where τ is the gate time. The final value of $A(\tau)$ is the area enclosed by the trajectory and thus the accumulated phase. As can be inferred from $U(t)$, the accumulated phase depends on the joint state of both ions and thus implements a two-qubit phase gate in the S_y basis. In the S_z basis, a maximally entangled state emerges from a product state for $|A(\tau)| = \pi/2$. We introduce the dimensionless envelope $P(t)$ through $\Omega(t) = \Omega_{\mathrm{MS}} P(t)$. For $P(t)$ constant in the range $0 \le t \le \tau$ and 0 otherwise, one obtains the well-known square pulse gate.

Consider the class of functions $P(t) = \sin^n(\alpha t)$ with α and n suitable constants, which also ensure $P(t) = 0$ at the beginning and a "soft" start [29]. For near-field microwave gates, a soft start in amplitude modulation is known to suppress unwanted motional excitation from microwave electric pseudopotential kicks [30]. At the total gate time τ, a soft end is desirable, which implies $\alpha\tau = m\pi$ for an integer m identifying the number of pulses present in the envelope. At the end the phase space loop also needs to be closed, which puts a constraint on δ. Without losing generality, we restrict ourselves to the case of $n = 2$ and $m = 1$. The integrals Eq. (1) can be solved analytically, and one finds that multiple sets of τ and δ yield the required gate phase $|A(\tau)| = \pi/2$ and a closed trajectory. For $n = 2$ and $m = 1$, the detuning is

$$\delta_k = \frac{2\pi(k+1)}{\tau_k},$$

where k is the order of the shaped gate and τ_k the gate time required to generate the maximally entangled state for this order. The latter can be calculated analytically using Eq. (1) and the constraints mentioned above. Figure 1 shows the phase space trajectories of a representative spin state for the square pulse gate and for the first two orders of $\sin^2$ amplitude modulation. Increasing orders will exhibit more

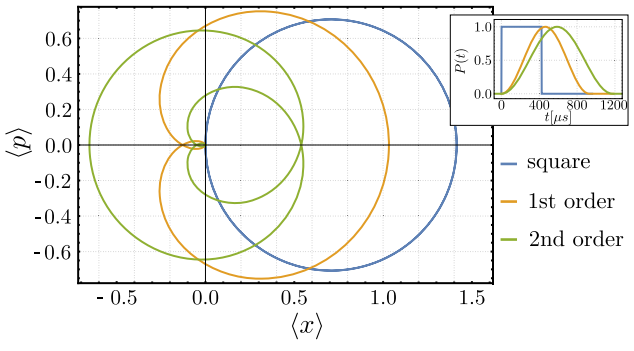

FIG. 1. Phase space trajectories for a representative spin state in the case of a square pulse gate (blue) and a first-order ($k = 1$, orange) and second-order ($k = 2$, green) amplitude modulated gate using a $\sin^2$ amplitude modulation function. The inset shows the three envelopes which produce the main plot trajectories for $\Omega_{\mathrm{MS}}/2\pi = 1.18$ kHz.

windings with a reduced radius around the origin. In general, this reduced radius will alleviate the impact of symmetric errors such as a miscalibrated secular mode frequency ω_r or detuning δ. This is because $F(\tau)$ and $G(\tau)$, in the presence of errors, end up closer to the phase space origin than for the square pulse, therefore more reliably disentangling the qubit degree of freedom from the motional state [22].

We use $^9Be^+$ ions in a surface-electrode trap with integrated microwave conductors described in Ref. [8]. Doppler cooling and detection are performed on the closed-cycle transition $^2S_{1/2}|F = 2, m_F = 2\rangle \leftrightarrow {}^2P_{3/2}|m_J = \frac{3}{2}, m_I = \frac{3}{2}\rangle$ at $\lambda = 313$ nm; the detection window is 400 μs long. We use the hyperfine transition in the electronic ground state $^2S_{1/2}$ $|F = 2, m_F = +1\rangle \equiv |\uparrow\rangle \leftrightarrow {}^2S_{1/2}|F = 1, m_F = +1\rangle \equiv |\downarrow\rangle$ as our qubit, which for a magnetic field of $|B_0| \simeq 22.3$ mT has a frequency of $\omega_0 \simeq 2\pi \times 1082.55$ MHz and is first-order field independent, allowing long coherence times [31]. F is the total angular momentum, J the total electronic angular momentum, I the nuclear spin, and m_F, m_J, and m_I their respective projections on the quantization axis. All carrier transitions in the $^2S_{1/2}$ manifold are excited by resonant microwaves from a conductor embedded in the trap. To perform high-fidelity carrier operations we use composite pulses sequences [32,33] to realize π and $\pi/2$ rotations for state preparation, shelving, and analysis.

Sideband transitions are excited using a single microwave conductor designed to produce a strong oscillating magnetic field quadrupole [34] at the desired frequency. The quadrupole is designed to provide the gradient necessary for spin-motion coupling while reducing the residual field at its minimum to avoid off-resonant carrier excitation. By applying a microwave power of ~5.5 W, we obtain a gradient of around 19 T/m. Microwave amplitude modulation is performed by an arbitrary waveform generator [35] providing the setpoint of a digital PI controller [36], which in turn controls a fast analog multiplier [37].

For the bichromatic microwave gate drive, we measure $\Omega_{\mathrm{MS}}/2\pi = 1.18$ kHz. The gate is carried out on the two-ion low frequency (LF) out-of-phase radial mode at a frequency of $\omega_r/2\pi = 6.16$ MHz. Using sideband thermometry [38], we estimate an average occupation of $\bar{n} = 0.4(1)$ and a heating rate of $\dot{\bar{n}} = 8.4(7)$ s^{-1}. Throughout this work, no "warm-up" pulse was employed to compensate the effect of an observed "chirp" in the motional mode frequency [8,9], likely caused by thermal transients from microwave currents in the trap. This avoids additional energy dissipation not strictly related to gate operation.

Amplitude modulation of the driving fields affects not only the gate Rabi rate but potentially also the qubit energy splitting through power-dependent shifts, such as the differential ac Zeeman shift. This shift arises from nonzero oscillatory fields that accompany the oscillating gradient and introduce a new time-dependent term in the Hamiltonian,

$$H_Z(t) = P^2(t)\frac{\Delta}{2}\sum_j \sigma_j^z, \tag{2}$$

where Δ is the peak differential ac Zeeman shift and σ_j^z is the Pauli matrix for ion j. Experimentally, this can be addressed in several ways, one of which is to drive the gate using sideband tones with time-dependent frequencies $\omega(t) = \omega_0 + \Delta P^2(t) \pm (\omega_r + \delta)$, where the sign identifies the blue or red sideband. Another possibility is dynamic decoupling [9]. Here we employ a microwave conductor designed to minimize the residual field at the ion position and hence make Δ as small as possible.

The ac Zeeman shift induced by a single sideband on our qubit transition is dominated by the projection of the microwave field on $\mathbf{B_0}$ (π component). For the bichromatic drive, the shifts due to the π components of the two sidebands would have opposite sign and ideally cancel each other. Any remaining shift is due to off-resonant coupling to $\Delta m_F = \pm 1$ transitions detuned by $\approx$200 MHz from the qubit and induced by the microwave's field projection orthogonal to $\mathbf{B_0}$ (σ components). The trap is engineered to have a minimum of the oscillating magnetic field as close to the pseudopotential null as possible. Because of imperfections, it is displaced from the pseudopotential null by about 1.5 μm. We operate our gate close to this position, where the observed ac Zeeman shift on the qubit transition is minimized (the σ field components effectively vanish, giving $\Delta \leq 5$ Hz). Because of the increased micromotion, the ions are driven away from the minimum periodically at a rate given by the rf drive frequency. Because of the spatial dependence of the ac Zeeman shift around the chosen position, an additional time-dependent shift may then occur.

In general, the Bell state fidelity $\mathcal{F}$ is a function of F, G, and A [23]. For the $\sin^2$ pulse, we find that all derivatives of the fidelity $[\partial^n \mathcal{F}(F, G, A)/\partial t^n]|_{t=\tau_k}$ in the motional ground state, $n = 0$, are equal to 0, demonstrating the intrinsic resilience against timing imperfections. One can observe this behavior by turning off the microwave drive at different times of the $\sin^2$ pulse. Figure 2 shows experimental data for $k = 17$ ($\tau_{17} = 2938\mu$s) together with predictions from the analytic solution of Ref. [28]. As expected from the derivatives of $F(t)$, $G(t)$, and $A(t)$, the population dynamics is stable around $t = \tau_{17}$, where the derivatives vanish.

To compare the performance of the amplitude modulated gate to a square pulse gate, a relevant quantity for microwave near fields is given by the total energy deposited in the trap structure by the bichromatic current, due to potential thermal effects. This is different from laser-based gates, where available laser power typically imposes limits to gate speeds. We therefore compare the gate fidelity to a square pulse gate with seven loops in phase space and $\tau = 1122$ μs since the pulse energies are equal. From finite element simulations [39], the microwave conductor reflects 91.1% of the amplitude; the energy dissipated per gate is about 1 mJ. To prove the resilience in a direct comparison,

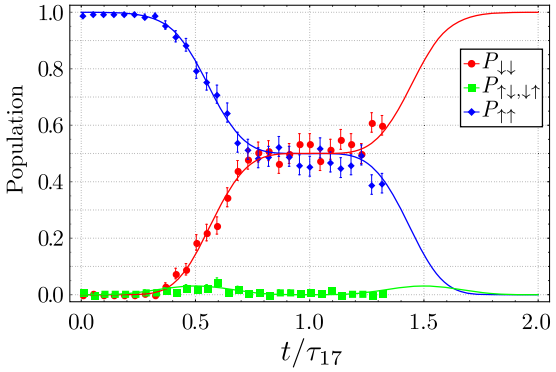

FIG. 2. Dynamics of the internal state of the ions during the time evolution of the $\sin^2$ pulse. The flat region around $t/\tau_{17} = 1$ is expected by the analytical model (solid lines) and observed in the experiment. Each data point is an average of 200 experiments.

we amplitude modulate the rf trap drive with Gaussian noise [40], thereby introducing fluctuations of the radial mode frequency. To characterize the amount of noise injected, we measure the instantaneous linewidth of ω_r for different values of the noise source's amplitude: after resolved sideband cooling to near the motional ground state, we excite the motion with a weak near-resonant electric field and apply a red sideband π pulse to flip the spin conditional on the motional excitation. The FWHM of the signal as a function of the electric field frequency is taken as a measure of the injected noise. Gates are carried out in an interleaved way between the $\sin^2$ and the square pulse gate, in order to probe the same conditions for both amplitude shapes. The fidelity of the maximally entangled state, $1/\sqrt{2}(|\uparrow\uparrow\rangle - i|\downarrow\downarrow\rangle)$, is extracted from parity oscillations and from the fluorescence signal of the $P_{\uparrow\uparrow}$ and $P_{\downarrow\downarrow}$ signal generated by scanning the phase of a $\pi/2$ analysis pulse [41]. Here we determined the state populations using a sum of weighted Poissonians as in Ref. [8].

The measured fidelities as a function of the radial mode FWHM due to the injected noise are shown in Fig. 3(a) and indicate that the amplitude modulated scheme suffers considerably less from noise than the standard square pulse scheme. In the latter case, reported fidelities are lower than theoretically expected, mainly due to slow drifts of the mode during data acquisition (about 6 min for data shown). The effect of slow variations of ω_r during the different acquisitions of the scan is different for each data point due to varying experimental conditions and therefore cannot be replicated accurately by theory. Figure 3(b) shows the expected infidelity for different schemes using an analytic model. We compare a standard 8 loop square pulse scheme which requires $\tau = 1200$ μs with a $k = 20$ $\sin^2$ modulation, $\tau_{20} = 3200$ μs. The two schemes have been chosen since they have the same pulse energy. We also compare to an improved version of the standard scheme which makes use of Walsh$[7, x]$ modulation [42] on the 8 loop gate. The

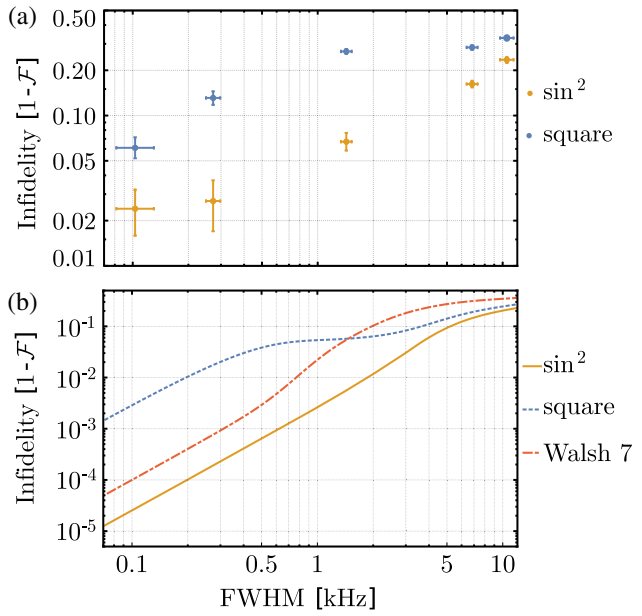

FIG. 3. Comparison between square pulse and $\sin^2$ amplitude modulated gate. (a) Experimental result. At any level of injected noise, the amplitude modulated gate with $k = 17$ results in higher fidelities than the 7 loop square pulse gate. (b) Expected infidelity from an analytic model for different schemes: $\sin^2$ with $k = 20, 8$ loop square pulse, Walsh$[7, x]$ modulation on 8 loop gate. The model accounts only for initial $\bar{n} = 0.4$; no other error sources have been included.

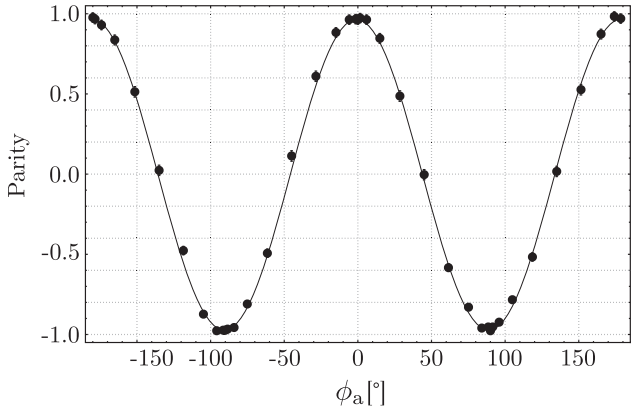

FIG. 4. Parity oscillations for $\sin^2$ shaped gate obtained by determining the state populations with thresholds in the fluorescence histogram. Each point is an average of 600 experiments.

amplitude modulated scheme at the same pulse energy presents a lower infidelity.

The best gate fidelities are obtained without the noise injection system attached, using a $\sin^2$ $k = 17$ pulse, under the same experimental conditions stated previously, and with a circuit to improve the stability of the delivered rf power (similar to Ref. [43]). The dataset is composed of two consecutive scans of the phase of the analysis $\pi/2$ pulse to extract parity oscillations. Here each phase is probed 300 times. To obtain reference histograms we detect and prepare four states, each measured 2×10^4 times. The Bell state fidelity is estimated using three methods. For the first method, state populations are determined using the sum of weighted Poissonians mentioned previously. To estimate the fidelity we perform a resampling bootstrap analysis. We generate multiple synthetic datasets by randomly assembling the data in two separate scans, where from one we extract the populations $P_{\uparrow\uparrow}$, $P_{\downarrow\downarrow}$ and from the other the parity amplitude. The operation is repeated 1000 times, resulting in a distribution of fidelities. We obtain a fidelity $\mathcal{F} = 99.5\%$ with a 68% confidence interval of [99.3, 99.7]%. For the second method, the populations are determined by dividing the fluorescence histograms using appropriate thresholds into three bins (i.e., zero, one, or two ions bright [9]). The resulting bootstrapped fidelity distribution has mean $\mathcal{F} = 99.7\%$ [state preparation and measurement error (SPAM) error corrected with $\epsilon_{\mathrm{SPAM}} = 1.5(1)\%$] with 68% confidence interval [99.6, 99.8]%. Figure 4 shows the combined parity oscillations from the original sets of data derived from the threshold analysis. Finally, the third method to extract the fidelity is the maximum-likelihood algorithm described in Ref. [44]. With a training fraction of 20% and a bootstrap of 1000, a fidelity of $\mathcal{F} = 99.2\%$ with a bootstrapped 68% confidence interval [99.1, 99.7]% is inferred. The uncertainty is larger because this algorithm produces a joint uncertainty on state analysis and tomography, whereas the two former methods estimate the fidelities after the states have already been assigned to the raw data. In the limit of vanishing SPAM error, the two former and the latter method should yield comparable uncertainties.

We now expect a major contribution to the error budget to be imperfections in the assumption $\Delta \simeq 0$. On one hand, time-varying shifts in the ion position relative to the ac Zeeman shift minimum, induced by fluctuating stray potentials, may cause variations of the ac Zeeman shift. On the other hand, as previously mentioned, micromotion can also lead to additional time-dependent ac Zeeman shifts. The strongest variation of the differential ac Zeeman shift expected from our finite element simulations is 0.6 Hz/nm. Assuming that one ion exhibits an ac Zeeman shift of 20 Hz relative to the other, which is at 0 Hz shift, simulations predict an infidelity of 1.1×10^{-3}. We expect gate infidelity contributions from motional heating of $\approx 2 \times 10^{-4}$, from imperfect ground state cooling of $\approx 1 \times 10^{-5}$ and of $< 1 \times 10^{-5}$ from the motional frequency chirp. Spectator modes contribute a simulated error of 5×10^{-4}, which can be mitigated by better engineering of trap potentials or by exploring additional modulation schemes designed to address spectral crowding [45].

In summary, we have introduced amplitude modulated two-qubit microwave near-field gates and demonstrated

their resilience to motional mode changes compared to the standard square pulse gate with the same pulse energy using noise injection, thereby addressing the major current challenge for these types of gates. The fully optimized gate reaches an infidelity in the 10^{-3} range. It might be useful to evaluate other pulse shapes such as Blackman pulses, weighted series of sines with different α, or even piecewise functions with a sufficient number of steps as already implemented with lasers [46]. Solutions to the remaining ac Zeeman shifts comprise better engineering of the magnetic field quadrupole, aimed at minimizing the differential ac Zeeman shift rather than the residual magnetic field at the minimum. The technique presented here is compatible with continuous dynamical decoupling [9] which would also allow us to reduce this source of error. An interesting perspective to further increase the gate speed would be the combination with motional squeezing [47].

We thank P. O. Schmidt and S. A. King for helpful discussions and comments on the manuscript. We are grateful for discussions and suggestions from T. P. Harty, R. Jördens, D. H. Slichter, and R. Srinivas. We acknowledge funding from the clusters of excellence "QUEST" and "QuantumFrontiers", from the EU QT flagship project "MicroQC" and from DFG through CRC 1227 DQ-*mat*, projects A01, and A06, and from PTB and LUH.

*Corresponding author.
christian.ospelkaus@iqo.uni-hannover.de

[1] K. R. Brown, J. Kim, and C. Monroe, npj Quantum Inf. **2**, 16034 (2016).
[2] A. Bermudez, X. Xu, R. Nigmatullin, J. O'Gorman, V. Negnevitsky, P. Schindler, T. Monz, U. G. Poschinger, C. Hempel, J. Home, F. Schmidt-Kaler, M. Biercuk, R. Blatt, S. Benjamin, and M. Müller, Phys. Rev. X **7**, 041061 (2017).
[3] R. Blatt and C. F. Roos, Nat. Phys. **8**, 277 (2012).
[4] F. Mintert and C. Wunderlich, Phys. Rev. Lett. **87**, 257904 (2001).
[5] C. Ospelkaus, C. E. Langer, J. M. Amini, K. R. Brown, D. Leibfried, and D. J. Wineland, Phys. Rev. Lett. **101**, 090502 (2008).
[6] C. J. Ballance, T. P. Harty, N. M. Linke, M. A. Sepiol, and D. M. Lucas, Phys. Rev. Lett. **117**, 060504 (2016).
[7] J. P. Gaebler, T. R. Tan, Y. Lin, Y. Wan, R. Bowler, A. C. Keith, S. Glancy, K. Coakley, E. Knill, D. Leibfried, and D. J. Wineland, Phys. Rev. Lett. **117**, 060505 (2016).
[8] H. Hahn, G. Zarantonello, M. Schulte, A. Bautista-Salvador, K. Hammerer, and C. Ospelkaus, npj Quantum Inf. **5**, 70 (2019).
[9] T. P. Harty, M. A. Sepiol, D. T. C. Allcock, C. J. Ballance, J. E. Tarlton, and D. M. Lucas, Phys. Rev. Lett. **117**, 140501 (2016).
[10] S. Weidt, J. Randall, S. Webster, K. Lake, A. Webb, I. Cohen, T. Navickas, B. Lekitsch, A. Retzker, and W. Hensinger, Phys. Rev. Lett. **117**, 220501 (2016).
[11] T. Manovitz, A. Rotem, R. Shaniv, I. Cohen, Y. Shapira, N. Akerman, A. Retzker, and R. Ozeri, Phys. Rev. Lett. **119**, 220505 (2017).
[12] D. Hayes, S. M. Clark, S. Debnath, D. Hucul, I. V. Inlek, K. W. Lee, Q. Quraishi, and C. Monroe, Phys. Rev. Lett. **109**, 020503 (2012).
[13] N. Timoney, I. Baumgart, M. Johanning, A. F. Varon, M. B. Plenio, A. Retzker, and C. Wunderlich, Nature (London) **476**, 185 (2011).
[14] A. R. Milne, C. L. Edmunds, C. Hempel, V. Frey, S. Mavadia, and M. J. Biercuk, arXiv:1808.10462.
[15] S.-L. Zhu, C. Monroe, and L.-M. Duan, Phys. Rev. Lett. **97**, 050505 (2006).
[16] C. F. Roos, New J. Phys. **10**, 013002 (2008).
[17] T. Choi, S. Debnath, T. A. Manning, C. Figgatt, Z.-X. Gong, L.-M. Duan, and C. Monroe, Phys. Rev. Lett. **112**, 190502 (2014).
[18] A. M. Steane, G. Imreh, J. P. Home, and D. Leibfried, New J. Phys. **16**, 053049 (2014).
[19] M. Palmero, S. Martínez-Garaot, D. Leibfried, D. J. Wineland, and J. G. Muga, Phys. Rev. A **95**, 022328 (2017).
[20] V. M. Schäfer, C. J. Ballance, K. Thirumalai, L. J. Stephenson, T. G. Ballance, A. M. Steane, and D. M. Lucas, Nature (London) **555**, 75 (2018).
[21] P. H. Leung and K. R. Brown, Phys. Rev. A **98**, 032318 (2018).
[22] F. Haddadfarshi and F. Mintert, New J. Phys. **18**, 123007 (2016).
[23] Y. Shapira, R. Shaniv, T. Manovitz, N. Akerman, and R. Ozeri, Phys. Rev. Lett. **121**, 180502 (2018).
[24] A. Webb, S. Webster, S. Collingbourne, D. Bretaud, A. Lawrence, S. Weidt, F. Mintert, and W. Hensinger, Phys. Rev. Lett. **121**, 180501 (2018).
[25] K. Mølmer and A. Sørensen, Phys. Rev. Lett. **82**, 1835 (1999).
[26] E. Solano, R. L. de Matos Filho, and N. Zagury, Phys. Rev. A **59**, R2539 (1999).
[27] G. J. Milburn, S. Schneider, and D. F. V. James, Fortschr. Phys. **48**, 801 (2000).
[28] A. Sørensen and K. Mølmer, Phys. Rev. A **62**, 022311 (2000).
[29] R. T. Sutherland, R. Srinivas, S. C. Burd, D. Leibfried, A. C. Wilson, D. J. Wineland, D. T. C. Allcock, D. H. Slichter, and S. B. Libby, New J. Phys. **21**, 033033 (2019).
[30] U. Warring, C. Ospelkaus, Y. Colombe, K. R. Brown, J. M. Amini, M. Carsjens, D. Leibfried, and D. J. Wineland, Phys. Rev. A **87**, 013437 (2013).
[31] C. Langer, R. Ozeri, J. D. Jost, J. Chiaverini, B. DeMarco, A. Ben-Kish, R. B. Blakestad, J. Britton, D. B. Hume, W. M. Itano, D. Leibfried, R. Reichle, T. Rosenband, T. Schaetz, P. O. Schmidt, and D. J. Wineland, Phys. Rev. Lett. **95**, 060502 (2005).
[32] B. T. Torosov and N. V. Vitanov, Phys. Rev. A **83**, 053420 (2011).
[33] G. T. Genov, D. Schraft, T. Halfmann, and N. V. Vitanov, Phys. Rev. Lett. **113**, 043001 (2014).
[34] M. Wahnschaffe, H. Hahn, G. Zarantonello, T. Dubielzig, S. Grondkowski, A. Bautista-Salvador, M. Kohnen, and C. Ospelkaus, Appl. Phys. Lett. **110**, 034103 (2017).
[35] R. Bowler, U. Warring, J. W. Britton, B. C. Sawyer, and J. Amini, Rev. Sci. Instrum. **84**, 033108 (2013).

[36] S. Hannig, J. Mielke, J. A. Fenske, M. Misera, N. Beev, C. Ospelkaus, and P. O. Schmidt, Rev. Sci. Instrum. **89**, 013106 (2018).
[37] H. Hahn, Two-qubit microwave quantum logic gate with 9Be+ ions in scalable surface-electrode ion traps, Ph. D. thesis, Gottfried Wilhelm Leibniz Universität, Hannover, 2019.
[38] Q. A. Turchette, D. Kielpinski, B. E. King, D. Leibfried, D. M. Meekhof, C. J. Myatt, M. A. Rowe, C. A. Sackett, C. S. Wood, W. M. Itano, C. Monroe, and D. J. Wineland, Phys. Rev. A **61**, 063418 (2000).
[39] H. Hahn, G. Zarantonello, A. Bautista-Salvador, M. Wahnschaffe, M. Kohnen, J. Schoebel, P. O. Schmidt, and C. Ospelkaus, Appl. Phys. B **125**, 154 (2019).
[40] Noise source is a Agilent 33250A waveform generator.
[41] C. A. Sackett, D. Kielpinski, B. E. King, C. Langer, V. Meyer, C. J. Myatt, M. Rowe, Q. A. Turchette, W. M. Itano, D. J. Wineland, and C. Monroe, Nature (London) **404**, 256 (2000).
[42] D. Hayes, S. M. Clark, S. Debnath, D. Hucul, Q. Quraishi, and C. Monroe, Phys. Rev. Lett. **109**, 020503 (2012).
[43] T. Harty, High-fidelity microwave-driven quantum logic in intermediate-field 43Ca+, Ph.D. thesis, Oxford, 2013.
[44] A. C. Keith, C. H. Baldwin, S. Glancy, and E. Knill, Phys. Rev. A **98**, 042318 (2018).
[45] P. H. Leung, K. A. Landsman, C. Figgatt, N. M. Linke, C. Monroe, and K. R. Brown, Phys. Rev. Lett. **120**, 020501 (2018).
[46] C. Figgatt, A. Ostrander, N. M. Linke, K. A. Landsman, D. Zhu, D. Maslov, and C. Monroe, Nature (London) **572**, 368 (2019).
[47] W. Ge, B. C. Sawyer, J. W. Britton, K. Jacobs, J. J. Bollinger, and M. Foss-Feig, Phys. Rev. Lett. **122**, 030501 (2019).

Chapter 6

Conclusions

6.1 Summary

Within this thesis, we have presented a trap design that can be used to perform oscillating magnetic field gradient driven gate operations on trapped ions with a single integrated microwave conductor. Chapter 2 explains the necessity to perform FEM simulations to predict the field pattern defined by the geometry of the conductor. Publication **P1** reports the model developed to analyze the magnetic field quadrupole and its use to characterize the specific case of the 'SpyderTrap'.
Chapter 3 describes why a multilayer trap is fundamental for the realization of the QCCD architecture. The fabrication method is reported in publication **P2** and summarized in this work. Publication **P3** discusses the simulation and characterization of the multilayer trap 'ML5G' which presents an advanced 3D microwave conductor. This work provides an extension of the study with simulations of alternative designs and a more complete investigation of the coupling between microwave conductors.
Chapter 4 introduces the theory behind oscillating microwave near-field operations and discusses the generation of a maximally entangled Bell state in the trap 'ConsTrap', as reported in publication **P4**. A fidelity of 98.2(1.2) % has been achieved. The construction of an error budget shows that the main error sources are due to the motional state of the ions.
The use of quantum control methods can reduce the gate errors connected with

the ions' motion. Publication **P5** demonstrates, through artificially increasing the motional noise, that amplitude modulation of the microwave gate drive is robust against motional errors. Furthermore, it reports on the generation of a maximally entangled Bell state with an infidelity in the 10^{-3} range. This result is confirmed by analyzing the collected data using three different methods. Chapter 5 presents an additional comparison, using an analytical model, between different coherent control methods and discusses possible remaining sources of infidelity for the experimentally generated entangled state.

6.2 Outlook

From the results presented, the entangling gate operation fidelity of publication **P5** is limited by the presence of σ^z type errors. As previously discussed in Sec. 5.4 the use of continuous dynamical decoupling [BSPR12, HSA$^+$16] can reduce the influence of this error and potentially allow to reach even higher fidelities.

The motional mode heating rate $\dot{\bar{n}}$ is an intrinsic limit to the gate fidelity. For room temperature setups, it is possible to reduce the heating rate by cleaning the trap surface from potential adsorbates or other forms of contamination [HCW$^+$12, AGH$^+$11]. Another possibility to reduce the heating rate is to operate the trap in cryogenic conditions [DOS$^+$06, LGA$^+$08]. This solution presents the additional advantage of extending the ions lifetime in the trap [SBB$^+$17] thanks to the reduced background gas collision in vacuum.
Another approach to reduce the gate errors caused by the heating rate is to perform faster gates. A simple method can be to increase the magnetic field gradient and therefore the gate Rabi rate Ω_{MS}. In the case of microwave driven operations, the magnetic field increase is fundamentally limited by the maximum currents that can be dissipated in the trap before achieving critical temperatures. Another method for faster gate operation without increasing the magnetic field gradient is to use squeezed motional modes [GSB$^+$19].

To reduce the SPAM error, in order to quantify high gate fidelities, it is essential to change the detection scheme of the current setup. One possibility is to detect each ion independently instead of measuring the global fluorescence. In this case the problem of partially overlapping Poissonians of multiple bright ions, described in Sec. 4.5, is resolved. One way to do so is to split the two

ions in separate potential wells, then transport one ion into the detection zone and the other out of it. The PMT would collect light only from the ion on which the detection laser impinges. Other possibilities are offered by different detectors: multi-channel PMT [DLF+16] or camera read-out [BSWL10]. In these cases, it would be possible to detect each ion independently through the spatial resolution of the detectors.
If single ion detection is not possible, or if the SPAM error is still too high even for individual-ion detection, it is desirable to quantify the gate error through randomized benchmarking [KLR+08, GMT+12]. This approach relies on repeating the entangling gate operation multiple times together with a randomized sequence of qubit rotations. By measuring the probability to detect the wrong qubit states for gate sequences of different length, it is possible to determine the error per gate independent of SPAM errors. As stated in Sec. 5.3.4, this protocol requires the ability to trap and manipulate a second species of ion, for the purpose of sympathetic cooling in the benchmark sequence.

In this work, we demonstrated the capability to build multilayer structures and to perform high fidelity entangling gates on a single-layer trap. In the future, it could be possible to fabricate a small prototype of a QCCD architecture including at least one RF junction [WAF+13, MSW17] and more than one MWM conductor. In such a trap it could be possible to test entangling gate crosstalk with microwave near-fields and subsequently to perform small-scale quantum algorithms.

^{9}Be$^+$

A.1 ^{9}Be$^+$ level scheme

Many details of the experimental setup are reported in [Hah19]. In Fig. A.1 is shown the level scheme of a ^{9}Be$^+$ ion under an external magnetic field of $B_0 = 22.307\,\mathrm{mT}$. The transition frequencies in the $^2S_{1/2}$ manifold are reported in Tab. A.1. The field has been selected to have a first-order field independent π-transition as qubit, transition Q. In the figure are also indicated the laser beams used and the transitions they address. BR and RR are the blue and red Raman lasers, they are used to perform sideband cooling and fast sideband operations on the qubit transition. RE is the repumper, used for state preparation and dissipation during resolved sideband cooling. BD is the resonant laser, used for detection, optical pumping and Doppler cooling.

Transition	Frequency [2πMHz]
A	854.644
Q	1082.547
B	1240.188
C	1239.921
D	1397.562
E	1525.724
F	1525.457
G	1653.618
H	1764.456

Table A.1: Transition frequencies for the $^2S_{1/2}$ manifold calculated at external magnetic field $B_0 = 22.307\,\mathrm{mT}$ where transition Q, the qubit, is first-order field independent.

In the detection interval the BD laser is turned on for $400\,\mu$s of time. The photons are detected by a PMT and the output logic signal is then counted by the experimental control. The PMT H8259-01 from Hamamtsu has been used for the works described in chapters 2, 3 and 4. For the work related to the microwave amplitude modulation of chapter 5 the PMT has been upgraded to a H10682-210, chosen due to the higher quantum efficiency of the photocathode material at our detection wavelength. This was done to further reduce SPAM errors connected to the detection, specifically the separation of the Poissonian distributions of 1 and 2 ions bright.

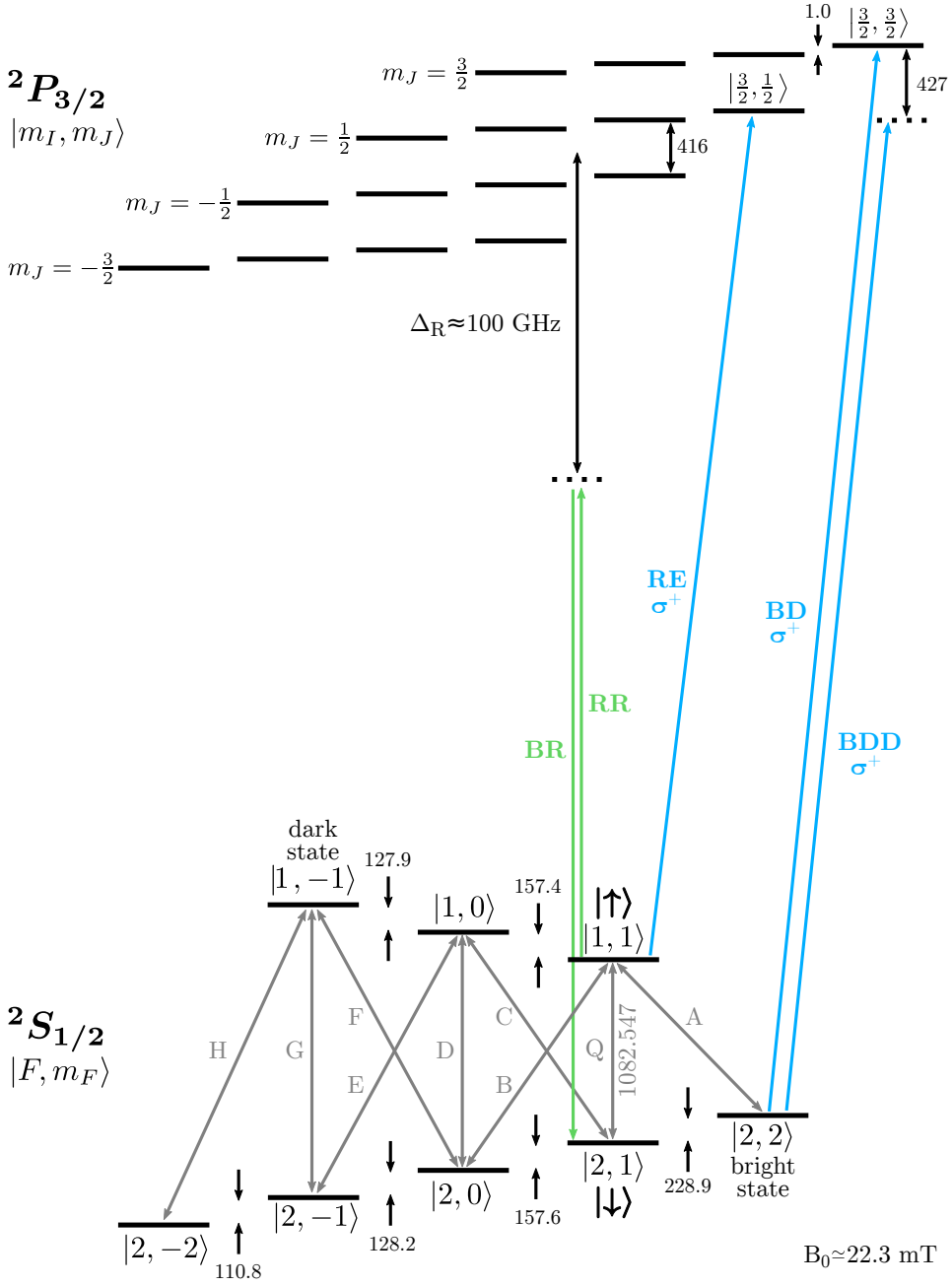

Figure A.1: Level scheme under a magnetic field of $B_0 = 22.3\,\mathrm{mT}$. Picture shows laser used in the experiment. Picture adapted from [Hah19].

Mølmer-Sørensen gate

B.1 Mølmer-Sørensen original formalism

In the original publication from Mølmer and Sørensen [MS99, SM99] a different Hamiltonian representation has been used compared to the one used in this thesis. Here we will use the operator $J_y = S_y/2$, instead of S_x, as done in Chapters 4 and 5, to avoid confusion with the position operator x. In the original article dimensionless position and momentum operators $x = (a + a^\dagger)/\sqrt{2}$, $p = i(a - a^\dagger)/\sqrt{2}$ were used. This makes us write eq. 4.9 as:

$$H_{\text{int}} = \hbar f(t) J_y x + \hbar g(t) J_y p \quad , \tag{B.1}$$

where, in the 'square' pulse case, $f(t) = -\sqrt{2}\Omega\cos(\delta t)$ and $g(t) = -\sqrt{2}\Omega\sin(\delta t)$. The exact propagator is then:

$$U(t) = e^{-iF(t)J_y x} e^{-iG(t)J_y p} e^{-iA(t)J_y^2} \quad . \tag{B.2}$$

The functions $F(t)$ and $G(t)$ are the primitives of $f(t)$ and $g(t)$ and describe the phase-space trajectory in terms of the position and momentum operator. $A(t)$ is now the area enclosed by the trajectories and defines the phase accumulation. By substitution of the notation used in chapter 5, we can find the conversion for the notation used in [ZHM+19]:

$$F(t) = 2\sqrt{2}\ \mathrm{Im}(\alpha(t)) \quad , \tag{B.3}$$

$$G(t) = 2\sqrt{2}\ \mathrm{Re}(\alpha(t) \quad , \tag{B.4}$$

$$A(t) = 4\ \mathrm{Im}(\Phi(t)) \tag{B.5}$$

This allows to say that a maximally entangled Bell state is achieved when $F(\tau) = 0$, $G(\tau) = 0$ and $A(\tau) = \pi/2$.

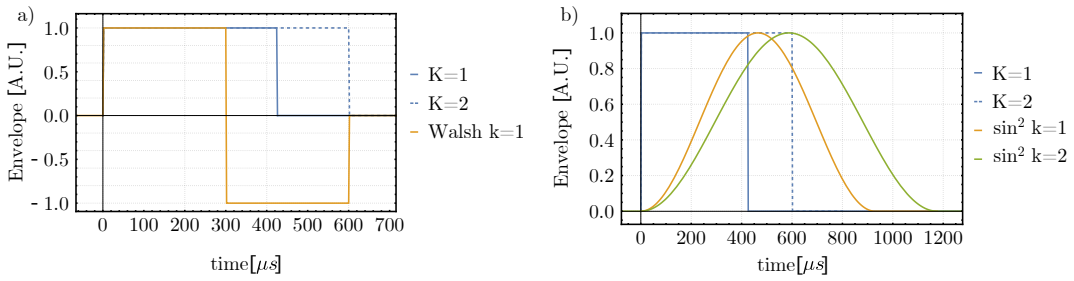

Figure B.1: a) Pulses for 'square' gate with $K = 1$ and $K = 2$ loops and for Walsh modulation of order k=1. The change of sign can be identified as phase inversion of the gate drive. b) Pulses for 'square' gate with $K = 1$ and $K = 2$ loops and $\sin^2$ gate with $k = 1$ and $k = 2$. Both plots assume a gate Rabi rate $\Omega = 1.18\,\mathrm{kHz}$.

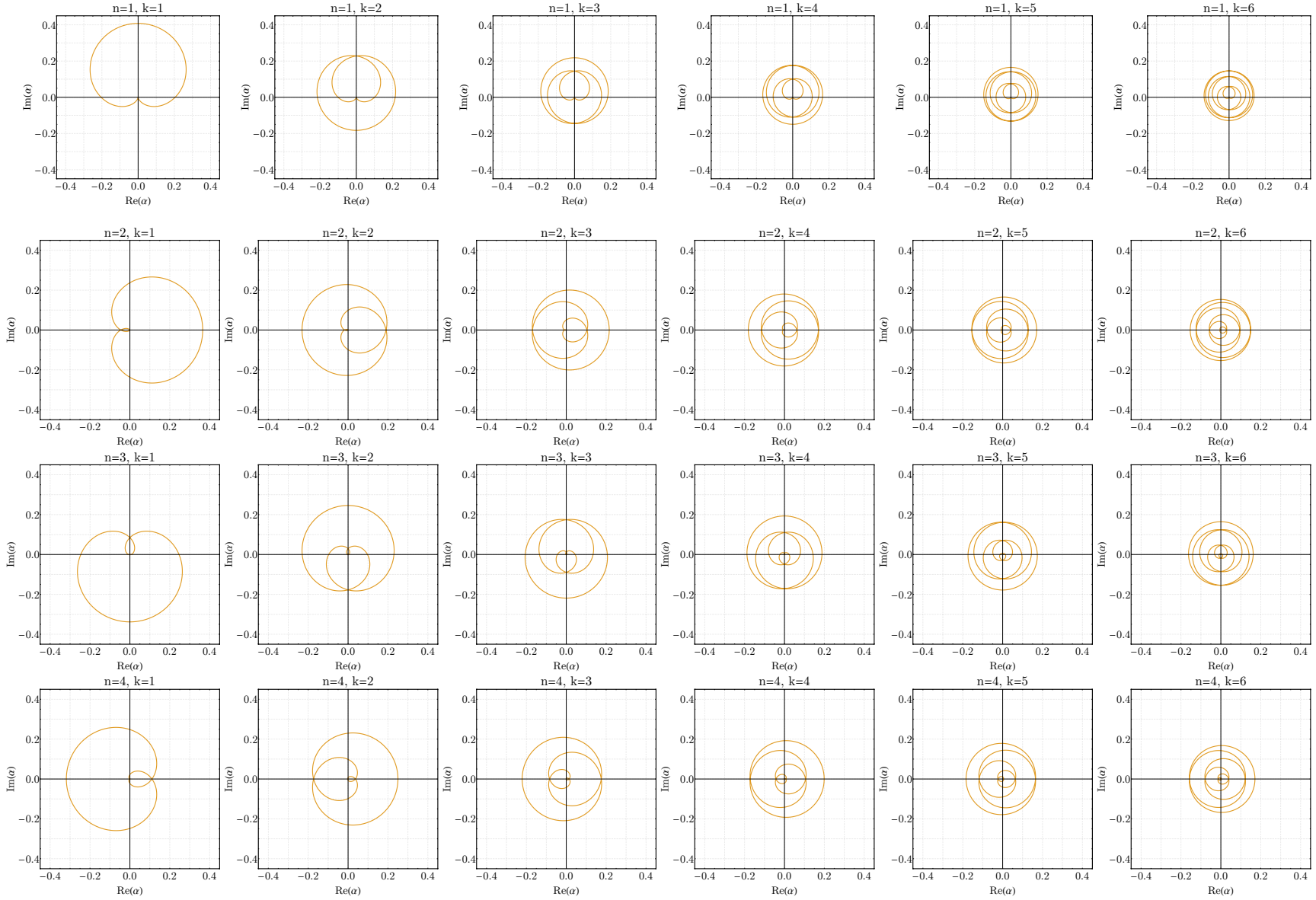

Figure B.2: Phase-space trajectories for different powers, n, and different orders, k, of sinusoidal amplitude modulation with $m = 1$.

Bibliography

[AAB+19] Frank Arute, Kunal Arya, Ryan Babbush, Dave Bacon, Joseph C. Bardin, Rami Barends, Rupak Biswas, Sergio Boixo, Fernando G. S. L. Brandao, David A. Buell, Brian Burkett, Yu Chen, Zijun Chen, Ben Chiaro, Roberto Collins, William Courtney, Andrew Dunsworth, Edward Farhi, Brooks Foxen, Austin Fowler, Craig Gidney, Marissa Giustina, Rob Graff, Keith Guerin, Steve Habegger, Matthew P. Harrigan, Michael J. Hartmann, Alan Ho, Markus Hoffmann, Trent Huang, Travis S. Humble, Sergei V. Isakov, Evan Jeffrey, Zhang Jiang, Dvir Kafri, Kostyantyn Kechedzhi, Julian Kelly, Paul V. Klimov, Sergey Knysh, Alexander Korotkov, Fedor Kostritsa, David Landhuis, Mike Lindmark, Erik Lucero, Dmitry Lyakh, Salvatore Mandrà, Jarrod R. McClean, Matthew McEwen, Anthony Megrant, Xiao Mi, Kristel Michielsen, Masoud Mohseni, Josh Mutus, Ofer Naaman, Matthew Neeley, Charles Neill, Murphy Yuezhen Niu, Eric Ostby, Andre Petukhov, John C. Platt, Chris Quintana, Eleanor G. Rieffel, Pedram Roushan, Nicholas C. Rubin, Daniel Sank, Kevin J. Satzinger, Vadim Smelyanskiy, Kevin J. Sung, Matthew D. Trevithick, Amit Vainsencher, Benjamin Villalonga, Theodore White, Z. Jamie Yao, Ping Yeh, Adam Zalcman, Hartmut Neven, and John M. Martinis. Quantum supremacy using a programmable superconducting processor. *Nature*, 574(7779):505–510, October 2019.

[ABH+05] M. Acton, K.-A. Brickman, P. C. Haljan, P. J. Lee, L. Deslauriers, and C. Monroe. Near-Perfect Simultaneous Measurement

of a Qubit Register. *arXiv:quant-ph/0511257*, November 2005. arXiv: quant-ph/0511257.

[ACP+18] I. Arrazola, J. Casanova, J. S. Pedernales, Z.-Y. Wang, E. Solano, and M. B. Plenio. Pulsed dynamical decoupling for fast and robust two-qubit gates on trapped ions. *Physical Review A*, 97(5):052312, May 2018.

[AGH+11] D T C Allcock, L Guidoni, T P Harty, C J Ballance, M G Blain, A M Steane, and D M Lucas. Reduction of heating rate in a microfabricated ion trap by pulsed-laser cleaning. *New Journal of Physics*, 13(12):123023, December 2011.

[AHB+13] D. T. C. Allcock, T. P. Harty, C. J. Ballance, B. C. Keitch, N. M. Linke, D. N. Stacey, and D. M. Lucas. A microfabricated ion trap with integrated microwave circuitry. *Applied Physics Letters*, 102(4):044103–044103–4, January 2013.

[APSC20] I. Arrazola, M.B. Plenio, E. Solano, and J. Casanova. Hybrid Microwave-Radiation Patterns for High-Fidelity Quantum Gates with Trapped Ions. *Physical Review Applied*, 13(2):024068, February 2020.

[AUW+10] J M Amini, H Uys, J H Wesenberg, S Seidelin, J Britton, J J Bollinger, D Leibfried, C Ospelkaus, A P VanDevender, and D J Wineland. Toward scalable ion traps for quantum information processing. *New Journal of Physics*, 12(3):033031, March 2010.

[Bal17] Christopher J. Ballance. *High-Fidelity Quantum Logic in Ca+*. Springer Theses. Springer International Publishing, Cham, 2017.

[Bar15] Stefanie Barz. Quantum computing with photons: introduction to the circuit model, the one-way quantum computer, and the fundamental principles of photonic experiments. *Journal of Physics B: Atomic, Molecular and Optical Physics*, 48(8):083001, March 2015.

[BBG+20] C. H. Baldwin, B. J. Bjork, J. P. Gaebler, D. Hayes, and D. Stack. Subspace benchmarking high-fidelity entangling operations with trapped ions. *Physical Review Research*, 2(1):013317, March 2020.

[BCJD99] Gavin K. Brennen, Carlton M. Caves, Poul S. Jessen, and Ivan H. Deutsch. Quantum Logic Gates in Optical Lattices. *Physical Review Letters*, 82(5):1060–1063, February 1999.

[BHIW86] J. C. Bergquist, Randall G. Hulet, Wayne M. Itano, and D. J. Wineland. Observation of Quantum Jumps in a Single Atom. *Physical Review Letters*, 57(14):1699–1702, October 1986.

[BKRB15] M. Brownnutt, M. Kumph, P. Rabl, and R. Blatt. Ion-trap measurements of electric-field noise near surfaces. *Reviews of Modern Physics*, 87(4):1419–1482, December 2015.

[BMB+98] D. J. Berkeland, J. D. Miller, J. C. Bergquist, W. M. Itano, and D. J. Wineland. Minimization of ion micromotion in a Paul trap. *Journal of Applied Physics*, 83(10):5025, 1998.

[BOC+11] K. R. Brown, C. Ospelkaus, Y. Colombe, A. C. Wilson, D. Leibfried, and D. J. Wineland. Coupled quantized mechanical oscillators. *Nature*, 471(7337):196–199, March 2011.

[BOV+09] R. B. Blakestad, C. Ospelkaus, A. P. VanDevender, J. M. Amini, J. Britton, D. Leibfried, and D. J. Wineland. High-Fidelity Transport of Trapped-Ion Qubits through an X-Junction Trap Array. *Physical Review Letters*, 102(15):153002, April 2009.

[Bow15] Ryan Bowler. *Coherent Ion Transport in a Multi-electrode Trap Array*. PhD thesis, University of Colorado, 2015.

[BPR+05] Gavin K Brennen, Guido Pupillo, Ana Maria Rey, Charles W Clark, and Carl J Williams. Scalable register initialization for quantum computing in an optical lattice. *Journal of Physics B: Atomic, Molecular and Optical Physics*, 38(11):1687–1694, June 2005.

[BSOWM19] A Bautista-Salvador, Christian Ospelkaus, Martina Wahnschaffe, and Jonathan Morgner. Verfahren zum Herstellen einer Atomfalle sowie Atomfalle, May 2019.

[BSPR12] A. Bermudez, P. O. Schmidt, M. B. Plenio, and A. Retzker. Robust trapped-ion quantum logic gates by continuous dynamical decoupling. *Physical Review A*, 85(4):040302, April 2012.

[BSWL10] A. H. Burrell, D. J. Szwer, S. C. Webster, and D. M. Lucas. Scalable simultaneous multiqubit readout with 99.99% single-shot fidelity. *Physical Review A*, 81(4):040302, April 2010.

[BSZH+19] A. Bautista-Salvador, G. Zarantonello, H. Hahn, A. Preciado-Grijalva, J. Morgner, M. Wahnschaffe, and C. Ospelkaus. Multilayer ion trap technology for scalable quantum computing and quantum simulation. *New Journal of Physics*, 21(4):043011, April 2019.

[BWB+13] R. Bowler, U. Warring, J. W. Britton, B. C. Sawyer, and J. Amini. Arbitrary waveform generator for quantum information processing with trapped ions. *Review of Scientific Instruments*, 84(3):033108–033108–6, March 2013.

[BXN+17] A. Bermudez, X. Xu, R. Nigmatullin, J. O'Gorman, V. Negnevitsky, P. Schindler, T. Monz, U. G. Poschinger, C. Hempel, J. Home, F. Schmidt-Kaler, M. Biercuk, R. Blatt, S. Benjamin, and M. Müller. Assessing the Progress of Trapped-Ion Processors Towards Fault-Tolerant Quantum Computation. *Physical Review X*, 7(4):041061, December 2017.

[CBB+05] J. Chiaverini, R.B. Blakestade, J. Britton, J.D. Jost, C. Langer, D. Leibfried, and D.J. Wineland. Surface-electrode architecture for ion-trap quantum information processing. *Quantum Information and Computation*, 5(6):419–439, 2005.

[CDM+14] T. Choi, S. Debnath, T. A. Manning, C. Figgatt, Z.-X. Gong, L.-M. Duan, and C. Monroe. Optimal quantum control of multimode couplings between trapped ion qubits for scalable entanglement. *Physical Review Letters*, 112(19):190502, January 2014.

[CGC+12] Jerry M Chow, Jay M Gambetta, A. D Corcoles, Seth T Merkel, John A Smolin, Chad Rigetti, S. Poletto, George A Keefe, Mary B Rothwell, J. R Rozen, Mark B Ketchen, and M. Steffen. Complete universal quantum gate set approaching fault-tolerant thresholds with superconducting qubits. *arXiv:1202.5344*, February 2012.

[CHLK15] Dong-Il "Dan" Cho, Seokjun Hong, Minjae Lee, and Taehyun Kim. A review of silicon microfabricated ion traps for quantum

information processing. *Micro and Nano Systems Letters*, 3:2, April 2015.

[CKDO14] M. Carsjens, M. Kohnen, T. Dubielzig, and C. Ospelkaus. Surface-electrode Paul trap with optimized near-field microwave control. *Applied Physics B*, 114(1-2):243–250, 2014.

[CVZ+98] Isaac L. Chuang, Lieven M. K. Vandersypen, Xinlan Zhou, Debbie W. Leung, and Seth Lloyd. Experimental realization of a quantum algorithm. *Nature*, 393(6681):143–146, May 1998.

[CW08] John Clarke and Frank K. Wilhelm. Superconducting quantum bits. *Nature*, 453(7198):1031–1042, June 2008.

[CZ95] J. I. Cirac and P. Zoller. Quantum Computations with Cold Trapped Ions. *Physical Review Letters*, 74(20):4091, 1995.

[CZKM97] J. I. Cirac, P. Zoller, H. J. Kimble, and H. Mabuchi. Quantum State Transfer and Entanglement Distribution among Distant Nodes in a Quantum Network. *Physical Review Letters*, 78(16):3221–3224, April 1997.

[Deu85] David Deutsch. Quantum theory, the Church–Turing principle and the universal quantum computer. *Proceedings of the Royal Society of London. A. Mathematical and Physical Sciences*, 400(1818):97–117, July 1985.

[DiV95] David P. DiVincenzo. Two-bit gates are universal for quantum computation. *Physical Review A*, 51(2):1015–1022, February 1995.

[DiV00] David P. DiVincenzo. The Physical Implementation of Quantum Computation. *Fortschritte der Physik*, 48(9-11):771–783, September 2000.

[DLF+16] S. Debnath, N. M. Linke, C. Figgatt, K. A. Landsman, K. Wright, and C. Monroe. Demonstration of a small programmable quantum computer with atomic qubits. *Nature*, 536(7614):63–66, August 2016.

[DOS+06] L. Deslauriers, S. Olmschenk, D. Stick, W. K. Hensinger, J. Sterk, and C. Monroe. Scaling and Suppression of Anomalous

Heating in Ion Traps. *Physical Review Letters*, 97(10):103007, 2006.

[DWM04] M. H. Devoret, A. Wallraff, and J. M. Martinis. Superconducting Qubits: A Short Review. *arXiv:cond-mat/0411174*, November 2004. arXiv: cond-mat/0411174.

[EWP+19] Alexander Erhard, Joel J. Wallman, Lukas Postler, Michael Meth, Roman Stricker, Esteban A. Martinez, Philipp Schindler, Thomas Monz, Joseph Emerson, and Rainer Blatt. Characterizing large-scale quantum computers via cycle benchmarking. *Nature Communications*, 10(1):1–7, November 2019.

[Fey82] Richard P. Feynman. Simulating physics with computers. *International Journal of Theoretical Physics*, 21(6-7):467–488, June 1982.

[FOL+19] C. Figgatt, A. Ostrander, N. M. Linke, K. A. Landsman, D. Zhu, D. Maslov, and C. Monroe. Parallel entangling operations on a universal ion-trap quantum computer. *Nature*, July 2019.

[GB15] Todd J. Green and Michael J. Biercuk. Phase-Modulated Decoupling and Error Suppression in Qubit-Oscillator Systems. *Physical Review Letters*, 114(12):120502, March 2015.

[GFS+15] Nicholas D. Guise, Spencer D. Fallek, Kelly E. Stevens, K. R. Brown, Curtis Volin, Alexa W. Harter, Jason M. Amini, Robert E. Higashi, Son Thai Lu, Helen M. Chanhvongsak, Thi A. Nguyen, Matthew S. Marcus, Thomas R. Ohnstein, and Daniel W. Youngner. Ball-grid array architecture for microfabricated ion traps. *Journal of Applied Physics*, 117(17):174901, May 2015.

[GMT+12] J. P. Gaebler, A. M. Meier, T. R. Tan, R. Bowler, Y. Lin, D. Hanneke, J. D. Jost, J. P. Home, E. Knill, D. Leibfried, and D. J. Wineland. Randomized Benchmarking of Multiqubit Gates. *Physical Review Letters*, 108(26):260503, June 2012.

[Gro97] Lov K. Grover. Quantum Mechanics Helps in Searching for a Needle in a Haystack. *Physical Review Letters*, 79(2):325–328, July 1997.

[GSB+19] Wenchao Ge, Brian C. Sawyer, Joseph W. Britton, Kurt Jacobs, John J. Bollinger, and Michael Foss-Feig. Trapped Ion Quantum Information Processing with Squeezed Phonons. *Physical Review Letters*, 122(3):030501, January 2019.

[GSHV14] Genko T. Genov, Daniel Schraft, Thomas Halfmann, and Nikolay V. Vitanov. Correction of Arbitrary Field Errors in Population Inversion of Quantum Systems by Universal Composite Pulses. *Physical Review Letters*, 113(4):043001, July 2014.

[GTL+16] J. P. Gaebler, T. R. Tan, Y. Lin, Y. Wan, R. Bowler, A. C. Keith, S. Glancy, K. Coakley, E. Knill, D. Leibfried, and D. J. Wineland. High-Fidelity Universal Gate Set for 9Be+ Ion Qubits. *Physical Review Letters*, 117(6):060505, August 2016.

[HAB+14] T. P. Harty, D. T. C. Allcock, C. J. Ballance, L. Guidoni, H. A. Janacek, N. M. Linke, D. N. Stacey, and D. M. Lucas. High-Fidelity Preparation, Gates, Memory, and Readout of a Trapped-Ion Quantum Bit. *Physical Review Letters*, 113(22):220501, November 2014.

[Hah19] Henning Hahn. *Two-qubit microwave quantum logic gate with 9Be+ ions in scalable surface-electrode ion traps*. PhD Thesis, Gottfried Wilhelm Leibniz Universität, Hannover, 2019.

[Har13] Thomas Harty. *High-Fidelity Microwave-Driven Quantum Logic in Intermediate-Field 43Ca+*. PhD thesis, Oxford, 2013.

[HCD+12] D. Hayes, S. M. Clark, S. Debnath, D. Hucul, I. V. Inlek, K. W. Lee, Q. Quraishi, and C. Monroe. Coherent Error Suppression in Multiqubit Entangling Gates. *Physical Review Letters*, 109(2):020503, 2012.

[HCW+12] D. A. Hite, Y. Colombe, A. C. Wilson, K. R. Brown, U. Warring, R. Jördens, J. D. Jost, K. S. McKay, D. P. Pappas, D. Leibfried, and D. J. Wineland. 100-Fold Reduction of Electric-Field Noise in an Ion Trap Cleaned with In Situ Argon-Ion-Beam Bombardment. *Physical Review Letters*, 109(10):103001, September 2012.

[HLB+11] M. Harlander, R. Lechner, M. Brownnutt, R. Blatt, and W. Hansel. Trapped-ion antennae for the transmission of quantum information. *Nature*, 471(7337):200–203, 2011.

[HLBH11] Marcus D. Hughes, Bjoern Lekitsch, Jiddu A. Broersma, and Winfried K. Hensinger. Microfabricated ion traps. *Contemporary Physics*, pages 1–25, September 2011.

[HM16] Farhang Haddadfarshi and Florian Mintert. High fidelity quantum gates of trapped ions in the presence of motional heating. *New Journal of Physics*, 18(12):123007, December 2016.

[HMF+18] S. Hannig, J. Mielke, J. A. Fenske, M. Misera, N. Beev, C. Ospelkaus, and P. O. Schmidt. A highly stable monolithic enhancement cavity for second harmonic generation in the ultraviolet. *Review of Scientific Instruments*, 89(1):013106, January 2018.

[HOS+06] W. K. Hensinger, S. Olmschenk, D. Stick, D. Hucul, M. Yeo, M. Acton, L. Deslauriers, C. Monroe, and J. Rabchuk. T-junction ion trap array for two-dimensional ion shuttling, storage, and manipulation. *Applied Physics Letters*, 88(3):034101–034101–3, January 2006.

[HS06] J. P. Home and A. M. Steane. Electrode Configurations for Fast Separation of Trapped Ions. *Quantum Information & Computation*, 6(4-5):289 – 325, 2006.

[HSA+16] T. P. Harty, M. A. Sepiol, D. T. C. Allcock, C. J. Ballance, J. E. Tarlton, and D. M. Lucas. High-Fidelity Trapped-Ion Quantum Logic Using Near-Field Microwaves. *Physical Review Letters*, 117(14):140501, September 2016.

[HZBS+19] H. Hahn, G. Zarantonello, A. Bautista-Salvador, M. Wahnschaffe, M. Kohnen, J. Schoebel, P. O. Schmidt, and C. Ospelkaus. Multilayer ion trap with three-dimensional microwave circuitry for scalable quantum logic applications. *Applied Physics B*, 125(8):154, July 2019.

[HZS+19] H. Hahn, G. Zarantonello, M. Schulte, A. Bautista-Salvador, K. Hammerer, and C. Ospelkaus. Integrated 9Be+ multi-qubit

gate device for the ion-trap quantum computer. *npj Quantum Information*, 5(1):70, August 2019.

[ICL+17] I. V. Inlek, C. Crocker, M. Lichtman, K. Sosnova, and C. Monroe. Multispecies Trapped-Ion Node for Quantum Networking. *Physical Review Letters*, 118(25):250502, June 2017.

[IV15] Svetoslav S. Ivanov and Nikolay V. Vitanov. Composite two-qubit gates. *Physical Review A*, 92(2):022333, August 2015.

[JAGH19] Shreyans Jain, Joseba Alonso, Matt Grau, and Jonathan P. Home. Scalable arrays of micro-fabricated Penning traps for quantum computing and simulation. *arXiv:1812.06755 [physics, physics:quant-ph]*, November 2019. arXiv: 1812.06755.

[Jam98] D.F.V. James. Quantum dynamics of cold trapped ions with application to quantum computation. *Applied Physics B: Lasers and Optics*, 66(2):181–190, February 1998.

[JWCR+16] K. G. Johnson, J. D. Wong-Campos, A. Restelli, K. A. Landsman, B. Neyenhuis, J. Mizrahi, and C. Monroe. Active stabilization of ion trap radiofrequency potentials. *Review of Scientific Instruments*, 87(5):053110, May 2016.

[KBGK18] Adam C. Keith, Charles H. Baldwin, Scott Glancy, and E. Knill. Joint quantum-state and measurement tomography with incomplete measurements. *Physical Review A*, 98(4):042318, October 2018.

[KLR+08] E. Knill, D. Leibfried, R. Reichle, J. Britton, R. B. Blakestad, J. D. Jost, C. Langer, R. Ozeri, S. Seidelin, and D. J. Wineland. Randomized benchmarking of quantum gates. *Physical Review A*, 77(1):012307, January 2008.

[KLS+20] V. Kaushal, B. Lekitsch, A. Stahl, J. Hilder, D. Pijn, C. Schmiegelow, A. Bermudez, M. Müller, F. Schmidt-Kaler, and U. Poschinger. Shuttling-based trapped-ion quantum information processing. *AVS Quantum Science*, 2(1):014101, February 2020.

[KMJ+11] Hanna Krauter, Christine A. Muschik, Kasper Jensen, Wojciech Wasilewski, Jonas M. Petersen, J. Ignacio Cirac, and Eugene S. Polzik. Entanglement Generated by Dissipation and Steady State Entanglement of Two Macroscopic Objects. *Physical Review Letters*, 107(8):080503, August 2011.

[KMK11] Taehyun Kim, Peter Maunz, and Jungsang Kim. Efficient collection of single photons emitted from a trapped ion into a single-mode fiber for scalable quantum-information processing. *Physical Review A*, 84(6):063423, December 2011.

[KMW02] D. Kielpinski, C. Monroe, and D. J. Wineland. Architecture for a large-scale ion-trap quantum computer. *Nature*, 417(6890):709–711, June 2002.

[Kni05] E. Knill. Quantum computing with realistically noisy devices. *Nature*, 434(7029):39–44, March 2005.

[Kni10] Emanuel Knill. Physics: Quantum computing. *Nature*, 463:441–443, January 2010.

[KRS+16] Henning Kaufmann, Thomas Ruster, Christian T. Schmiegelow, Marcelo A. Luda, Vidyut Kaushal, Jonas Schulz, David von Lindenfels, Ferdinand Schmidt-Kaler, and Ulrich G. Poschinger. Fast ion swapping for quantum information processing. July 2016.

[Lan06] Christopher E. Langer. *High Fidelity Quantum Information Processing with Trapped Ions*. PhD Thesis, University of Colorado, Boulder, Colorado, 2006.

[LB18] Pak Hong Leung and Kenneth R. Brown. Entangling an arbitrary pair of qubits in a long ion crystal. *Physical Review A*, 98(3):032318, September 2018.

[LBMW03] D. Leibfried, R. Blatt, C. Monroe, and D. Wineland. Quantum dynamics of single trapped ions. *Reviews of Modern Physics*, 75(1):281, March 2003.

[LBP13] A. Lemmer, A. Bermudez, and M. B. Plenio. Driven geometric phase gates with trapped ions. *New Journal of Physics*, 15(8):083001, August 2013.

[LD98] Daniel Loss and David P. DiVincenzo. Quantum computation with quantum dots. *Physical Review A*, 57(1):120–126, January 1998.

[LDM+03] D. Leibfried, B. DeMarco, V. Meyer, D. Lucas, M. Barrett, J. Britton, W. M. Itano, B. Jelenkovic, C. Langer, T. Rosenband, and D. J. Wineland. Experimental demonstration of a robust, high-fidelity geometric two ion-qubit phase gate. *Nature*, 422(6930):412–415, March 2003.

[LGA+08] Jaroslaw Labaziewicz, Yufei Ge, Paul Antohi, David Leibrandt, Kenneth R. Brown, and Isaac L. Chuang. Suppression of Heating Rates in Cryogenic Surface-Electrode Ion Traps. *Physical Review Letters*, 100(1):013001, January 2008.

[LGR+16] Y. Lin, J. P. Gaebler, F. Reiter, T. R. Tan, R. Bowler, Y. Wan, A. Keith, E. Knill, S. Glancy, K. Coakley, A. S. Sørensen, D. Leibfried, and D. J. Wineland. Preparation of Entangled States through Hilbert Space Engineering. *Physical Review Letters*, 117(14):140502, September 2016.

[Lin15] Yiheng Lin. *Quantum Entanglement Generation in Trapped Ions Using Coherent and Dissipative Methods*. PhD Thesis, University of Colorado, Boulder, Colorado, USA, 2015.

[LLC16] Kuan-Yu Lin, Guang Hao Low, and Isaac L. Chuang. Effects of electrode surface roughness on motional heating of trapped ions. *Physical Review A*, 94(1):013418, July 2016.

[LLF+18] Pak Hong Leung, Kevin A. Landsman, Caroline Figgatt, Norbert M. Linke, Christopher Monroe, and Kenneth R. Brown. Robust 2-Qubit Gates in a Linear Ion Crystal Using a Frequency-Modulated Driving Force. *Physical Review Letters*, 120(2):020501, January 2018.

[LOJ+05] C. Langer, R. Ozeri, J. D. Jost, J. Chiaverini, B. DeMarco, A. Ben-Kish, R. B. Blakestad, J. Britton, D. B. Hume, W. M. Itano, D. Leibfried, R. Reichle, T. Rosenband, T. Schaetz, P. O. Schmidt, and D. J. Wineland. Long-Lived Qubit Memory Using Atomic Ions. *Physical Review Letters*, 95(6):060502, 2005.

[LWF+17] Bjoern Lekitsch, Sebastian Weidt, Austin G. Fowler, Klaus Mølmer, Simon J. Devitt, Christof Wunderlich, and Winfried K. Hensinger. Blueprint for a microwave trapped ion quantum computer. *Science Advances*, 3(2):e1601540, February 2017.

[Mat16] Roland Matt. Ion-trap design for magnetic-field-driven quantum information processing. Master's thesis, ETH Zurich, 2016.

[Mau16] Peter Lukas Wilhelm Maunz. High Optical Access Trap 2.0. Technical Report SAND-2016-0796R, Sandia National Lab. (SNL-NM), Albuquerque, NM (United States), January 2016.

[MB11] John J. L. Morton and Simon C. Benjamin. Quantum computing: Snapshots of diamond spins. *Nat Phys*, 7(12):929–930, 2011.

[MBM+16] Karan K. Mehta, Colin D. Bruzewicz, Robert McConnell, Rajeev J. Ram, Jeremy M. Sage, and John Chiaverini. Integrated optical addressing of an ion qubit. *Nature Nanotechnology*, 11(12):1066–1070, 2016.

[MEH+20] Alistair R. Milne, Claire L. Edmunds, Cornelius Hempel, Federico Roy, Sandeep Mavadia, and Michael J. Biercuk. Phase-Modulated Entangling Gates Robust to Static and Time-Varying Errors. *Physical Review Applied*, 13(2):024022, February 2020.

[Mor20] Jonathan Morgner. Developments towards high-fidelity entangling gates in a surface-electrode ion trap. Master's thesis, Leibniz Universität Hannover, Hannover, April 2020.

[MRS+17] Tom Manovitz, Amit Rotem, Ravid Shaniv, Itsik Cohen, Yotam Shapira, Nitzan Akerman, Alex Retzker, and Roee Ozeri. Fast Dynamical Decoupling of the Mølmer-Sørensen Entangling Gate. *Physical Review Letters*, 119(22):220505, November 2017.

[MS99] Klaus Mølmer and Anders Sørensen. Multiparticle Entanglement of Hot Trapped Ions. *Physical Review Letters*, 82(9):1835, 1999.

[MSJ00] G.J. Milburn, S. Schneider, and D.F.V. James. Ion Trap Quantum Computing with Warm Ions. *Fortschritte der Physik*, 48(9-11):801–810, September 2000.

[MSW+08] A. H. Myerson, D. J. Szwer, S. C. Webster, D. T. C. Allcock, M. J. Curtis, G. Imreh, J. A. Sherman, D. N. Stacey, A. M. Steane, and D. M. Lucas. High-Fidelity Readout of Trapped-Ion Qubits. *Physical Review Letters*, 100(20):200502, 2008.

[MSW17] A. Mokhberi, R. Schmied, and S. Willitsch. Optimised surface-electrode ion-trap junctions for experiments with cold molecular ions. *New Journal of Physics*, 19(4):043023, 2017.

[MW01] Florian Mintert and Christof Wunderlich. Ion-Trap Quantum Logic Using Long-Wavelength Radiation. *Physical Review Letters*, 87(25):257904, November 2001.

[MZM+20] Karan K. Mehta, Chi Zhang, Maciej Malinowski, Thanh-Long Nguyen, Martin Stadler, and Jonathan P. Home. Integrated optical multi-ion quantum logic. *arXiv:2002.02258 [physics, physics:quant-ph]*, February 2020. arXiv: 2002.02258.

[noa16] QuTiP: Quantum tool box in PYTHON, 2016.

[NSD86] Warren Nagourney, Jon Sandberg, and Hans Dehmelt. Shelved optical electron amplifier: Observation of quantum jumps. *Physical Review Letters*, 56(26):2797–2799, June 1986.

[OIB+07] R. Ozeri, W. M. Itano, R. B. Blakestad, J. Britton, J. Chiaverini, J. D. Jost, C. Langer, D. Leibfried, R. Reichle, S. Seidelin, J. H. Wesenberg, and D. J. Wineland. Errors in trapped-ion quantum gates due to spontaneous photon scattering. *Physical Review A*, 75(4):042329, April 2007.

[OLA+08] C. Ospelkaus, C. E. Langer, J. M. Amini, K. R. Brown, D. Leibfried, and D. J. Wineland. Trapped-Ion Quantum Logic Gates Based on Oscillating Magnetic Fields. *Physical Review Letters*, 101(9):090502, 2008.

[OLJ+05] R. Ozeri, C. Langer, J. D. Jost, B. DeMarco, A. Ben-Kish, B. R. Blakestad, J. Britton, J. Chiaverini, W. M. Itano, D. B. Hume, D. Leibfried, T. Rosenband, P. O. Schmidt, and D. J. Wineland. Hyperfine Coherence in the Presence of Spontaneous Photon Scattering. *Physical Review Letters*, 95(3):030403, July 2005.

[OM01] Mário H Oliveira and José A Miranda. Biot-Savart-like law in electrostatics. *European Journal of Physics*, 22:31, 2001.

[Osp16] C. Ospelkaus. Microwave quantum control notes. *private communication*, 2016.

[OWC+11] C. Ospelkaus, U. Warring, Y. Colombe, K. R. Brown, J. M. Amini, D. Leibfried, and D. J. Wineland. Microwave quantum logic gates for trapped ions. *Nature*, 476(7359):181–184, 2011.

[Pau90] Wolfgang Paul. Electromagnetic traps for charged and neutral particles. *Reviews of Modern Physics*, 62(3):531–542, 1990.

[PDF+20] J. M. Pino, J. M. Dreiling, C. Figgatt, J. P. Gaebler, S. A. Moses, M. S. Allman, C. H. Baldwin, M. Foss-Feig, D. Hayes, K. Mayer, C. Ryan-Anderson, and B. Neyenhuis. Demonstration of the QCCD trapped-ion quantum computer architecture. *arXiv:2003.01293 [quant-ph]*, March 2020. arXiv: 2003.01293.

[Pen36] F. M. Penning. Die Glimmentladung bei niedrigem druck zwischen koaxialen Zylindern in einem axialen Magnetfeld. *Physica*, 3(9):873–894, November 1936.

[PMGL+17] M. Palmero, S. Martínez-Garaot, D. Leibfried, D. J. Wineland, and J. G. Muga. Fast phase gates with trapped ions. *Physical Review A*, 95(2):022328, February 2017.

[Pre98] Preskill John. Reliable quantum computers. *Proceedings of the Royal Society of London. Series A: Mathematical, Physical and Engineering Sciences*, 454(1969):385–410, January 1998.

[Pre18] John Preskill. Quantum Computing in the NISQ era and beyond. *Quantum*, 2:79, August 2018. arXiv: 1801.00862.

[RBKD+02] M. A. Rowe, A. Ben-Kish, B. DeMarco, D. Leibfried, V. Meyer, J. Beall, Joe Britton, J. Hughes, W. M. Itano, B. Jelenkovic, C. Langer, T. Rosenband, and D. J. Wineland. Transport of quantum states and separation of ions in a dual RF ion trap. *Quantum Information & Computation*, 2(4):257, 2002.

[RLR+04] C. F. Roos, G. P. T. Lancaster, M. Riebe, H. Häffner, W. Hänsel, S. Gulde, C. Becher, J. Eschner, F. Schmidt-Kaler, and R. Blatt.

Bell States of Atoms with Ultralong Lifetimes and Their Tomographic State Analysis. *Physical Review Letters*, 92(22):220402, June 2004.

[Roo08] Christian F Roos. Ion trap quantum gates with amplitude-modulated laser beams. *New Journal of Physics*, 10(1):013002, January 2008.

[SBB+17] S. Sellner, M. Besirli, M. Bohman, M. J. Borchert, J. Harrington, T. Higuchi, A. Mooser, H. Nagahama, G. Schneider, C. Smorra, T. Tanaka, K. Blaum, Y. Matsuda, C. Ospelkaus, W. Quint, J. Walz, Y. Yamazaki, and S. Ulmer. Improved limit on the directly measured antiproton lifetime. *New Journal of Physics*, 19(8):083023, August 2017.

[SBT+18] V. M. Schäfer, C. J. Ballance, K. Thirumalai, L. J. Stephenson, T. G. Ballance, A. M. Steane, and D. M. Lucas. Fast quantum logic gates with trapped-ion qubits. *Nature*, 555(7694):75–78, March 2018.

[Sch10] Roman Schmied. Electrostatics of gapped and finite surface electrodes. *New Journal of Physics*, 12(2):023038, February 2010.

[SCR+06] S. Seidelin, J. Chiaverini, R. Reichle, J. J. Bollinger, D. Leibfried, J. Britton, J. H. Wesenberg, R. B. Blakestad, R. J. Epstein, D. B. Hume, W. M. Itano, J. D. Jost, C. Langer, R. Ozeri, N. Shiga, and D. J. Wineland. Microfabricated Surface-Electrode Ion Trap for Scalable Quantum Information Processing. *Physical Review Letters*, 96(25):253003, June 2006.

[SdMFZ99] E. Solano, R. L. de Matos Filho, and N. Zagury. Deterministic Bell states and measurement of the motional state of two trapped ions. *Physical Review A*, 59(4):R2539, April 1999.

[Sep16] M. A. Sepiol. *A high-fidelity microwave driven two-qubit quantum logic gate in 43Ca+*. PhD thesis, Oxford, 2016.

[Ser10] Robert F. Service. Diamond Feats Give Quantum Computing a Solid Boost. *Science*, 329(5992):616–b–617, August 2010.

[SFH+10] D. Stick, K M Fortier, R. Haltli, C. Highstrete, D L Moehring, C. Tigges, and M G Blain. Demonstration of a microfabrciated surface electrode ion trap. *1008.0990*, August 2010.

[Sho94] P. W. Shor. Algorithms for quantum computation: Discrete logarithms and factoring. In *Proc. 35th Annual Symposium on Foundations of Computer Science*, pages 124–134, Los Alamitos, 1994. IEEE Computer Society Press.

[SIHL14] A. M. Steane, G. Imreh, J. P. Home, and D. Leibfried. Pulsed force sequences for fast phase-insensitive quantum gates in trapped ions. *New Journal of Physics*, 16(5):053049, 2014.

[SKK+00] C. A. Sackett, D. Kielpinski, B. E. King, C. Langer, V. Meyer, C. J. Myatt, M. Rowe, Q. A. Turchette, W. M. Itano, D. J. Wineland, and C. Monroe. Experimental entanglement of four particles. *Nature*, 404(6775):256–259, March 2000.

[SLL+18] Alireza Seif, Kevin A. Landsman, Norbert M. Linke, Caroline Figgatt, C. Monroe, and Mohammad Hafezi. Machine learning assisted readout of trapped-ion qubits. *Journal of Physics B: Atomic, Molecular and Optical Physics*, 51(17):174006, 2018.

[SM99] Anders Sørensen and Klaus Mølmer. Quantum Computation with Ions in Thermal Motion. *Physical Review Letters*, 82(9):1971–1974, March 1999.

[SM00] Anders Sørensen and Klaus Mølmer. Entanglement and quantum computation with ions in thermal motion. *Physical Review A*, 62(2):022311, July 2000.

[SNBT86] Th. Sauter, W. Neuhauser, R. Blatt, and P. E. Toschek. Observation of Quantum Jumps. *Physical Review Letters*, 57(14):1696–1698, October 1986.

[SNN+20] L. J. Stephenson, D. P. Nadlinger, B. C. Nichol, S. An, P. Drmota, T. G. Ballance, K. Thirumalai, J. F. Goodwin, D. M. Lucas, and C. J. Ballance. High-Rate, High-Fidelity Entanglement of Qubits Across an Elementary Quantum Network. *Physical Review Letters*, 124(11):110501, March 2020.

[SSB+19] R T Sutherland, R Srinivas, S C Burd, D Leibfried, A C Wilson, D J Wineland, D T C Allcock, D H Slichter, and S B Libby. Versatile laser-free trapped-ion entangling gates. *New Journal of Physics*, 21(3):033033, March 2019.

[SSM+18] Yotam Shapira, Ravid Shaniv, Tom Manovitz, Nitzan Akerman, and Roee Ozeri. Robust Entanglement Gates for Trapped-Ion Qubits. *Physical Review Letters*, 121(18), November 2018.

[Ste96] A. M. Steane. Error Correcting Codes in Quantum Theory. *Physical Review Letters*, 77(5):793–797, July 1996.

[Ste97] A. Steane. The ion trap quantum information processor. *Applied Physics B: Lasers and Optics*, 64(6):623–643, June 1997.

[SVL+17] D. H. Slichter, V. B. Verma, D. Leibfried, R. P. Mirin, S. W. Nam, and D. J. Wineland. UV-sensitive superconducting nanowire single photon detectors for integration in an ion trap. *Optics Express*, 25(8):8705–8720, April 2017.

[SWL09] Roman Schmied, Janus H. Wesenberg, and Dietrich Leibfried. Optimal Surface-Electrode Trap Lattices for Quantum Simulation with Trapped Ions. *Physical Review Letters*, 102(23):233002, June 2009.

[SWM10] M. Saffman, T. G. Walker, and K. Mølmer. Quantum information with Rydberg atoms. *Reviews of Modern Physics*, 82(3):2313, 2010.

[Tan16] Ting Rei Tan. *High-Fidelity Entangling Gates with Trapped-Ions*. PhD thesis, University of Colorado, 2016.

[Tar18] James Tarlton. *Probing qubit memory errors at the* 10^{-5} *level*. PhD thesis, Oxford, 2018.

[TV11] Boyan T. Torosov and Nikolay V. Vitanov. Smooth composite pulses for high-fidelity quantum information processing. *Physical Review A*, 83(5):053420, May 2011.

[Ung20] Paul Florian Ungerechts. *Ion Transport for Scalable Quantum Processors*. Bachelor's Thesis, Leibniz Universit at Hannover, Hannover, November 2020.

[VOW+17] Mehrnoosh Vahidpour, William O'Brien, Jon Tyler Whyland, Joel Angeles, Jayss Marshall, Diego Scarabelli, Genya Crossman, Kamal Yadav, Yuvraj Mohan, Catvu Bui, Vijay Rawat, Russ Renzas, Nagesh Vodrahalli, Andrew Bestwick, and Chad Rigetti. Superconducting Through-Silicon Vias for Quantum Integrated Circuits. August 2017.

[VR89] K. Vogel and H. Risken. Determination of quasiprobability distributions in terms of probability distributions for the rotated quadrature phase. *Physical Review A*, 40(5):2847–2849, September 1989.

[WAF+13] Kenneth Wright, Jason M. Amini, Daniel L. Faircloth, Curtis Volin, S. Charles Doret, Harley Hayden, C-S Pai, David W. Landgren, Douglas Denison, Tyler Killian, Richart E. Slusher, and Alexa W. Harter. Reliable transport through a microfabricated X -junction surface-electrode ion trap. *New Journal of Physics*, 15(3):033004, 2013.

[Wah16] Martina Wahnschaffe. *Engineered microwave control for trapped ions*. Dissertation, Gottfried Wilhelm Leibniz Universität, Hannover, March 2016.

[WCB+14] A. C. Wilson, Y. Colombe, K. R. Brown, E. Knill, D. Leibfried, and D. J. Wineland. Tunable spin-spin interactions and entanglement of ions in separate potential wells. *Nature*, 512(7512):57–60, August 2014.

[Wes08] J. H. Wesenberg. Electrostatics of surface-electrode ion traps. *Physical Review A*, 78(6):063410, December 2008.

[WHZ+17] M. Wahnschaffe, H. Hahn, G. Zarantonello, T. Dubielzig, S. Grondkowski, A. Bautista-Salvador, M. Kohnen, and C. Ospelkaus. Single-ion microwave near-field quantum sensor. *Applied Physics Letters*, 110(3):034103, January 2017.

[WLK+19] Gavin N. West, William Loh, Dave Kharas, Cheryl Sorace-Agaskar, Karan K. Mehta, Jeremy Sage, John Chiaverini, and Rajeev J. Ram. Low-loss integrated photonics for the blue and ultraviolet regime. *APL Photonics*, 4(2):026101, February 2019.

[WMI+98a] D.J. Wineland, C. Monroe, W.M. Itano, B.E. King, D. Leibfried, D.M. Meekhof, C. Myatt, and C. Wood. Experimental Primer on the Trapped Ion Quantum Computer. *Fortschritte der Physik*, 46(4-5):363–390, June 1998.

[WMI+98b] D.J. Wineland, C. Monroe, W.M. Itano, D. Leibfried, B.E. King, and D.M. Meekhof. Experimental issues in coherent quantum-state manipulation of trapped atomic ions. *Journal of Research of the National Institute of Standards and Technology*, 103(3):259, May 1998.

[WOC+13] U. Warring, C. Ospelkaus, Y. Colombe, K. R. Brown, J. M. Amini, M. Carsjens, D. Leibfried, and D. J. Wineland. Techniques for microwave near-field quantum control of trapped ions. *Physical Review A*, 87(1):013437, January 2013.

[WS12] Thad G Walker and Mark Saffman. Entanglement of Two Atoms using Rydberg Blockade. *arXiv:1202.5328*, February 2012.

[WWC+18] A. E. Webb, S. C. Webster, S. Collingbourne, D. Bretaud, A. M. Lawrence, S. Weidt, F. Mintert, and W. K. Hensinger. Resilient Entangling Gates for Trapped Ions. *Physical Review Letters*, 121(18), November 2018.

[ZMD06] Shi-Liang Zhu, C. Monroe, and L.-M. Duan. Trapped Ion Quantum Computation with Transverse Phonon Modes. *Physical Review Letters*, 97(5):050505, August 2006.

Acknowledgements

There are many people that I need to thank. First of all my supervisor Prof. Dr. Christian Ospelkaus, thank you for taking a random guy from Italy and molding him into what I am today. I would like to thank Prof. Dr. Piet Schmidt for all the helpful discussions on the experiment and for being a co-supervisor which actually cared that things were running smoothly. I need to sincerely thank Prof. Dr. Klemens Hammerer for giving me the suggestion which in the end prompted the idea of using amplitude modulation on the microwave gate drive.

I want to give all my thanks to the crowd from QUEST institute of the PTB and my group colleagues from Hannover. Thanks to you all life here has been enjoyable even in the darkest moments.

A special thanks goes to Dr. Henning Hahn. Words cannot express my gratitude to you for all the time we spent together, working on the experiment, discussing theory and commenting my poor writing skills. We went through good and bad times and you are the best mate I could ever ask through all of them. Another thanks goes to Dr. Amado Bautista-Salvador, thanks for doing the impossible with trap fab times whenever we asked a new trap for the day before yesterday. Thank you for all the discussions on crazy ideas we had together for new mad traps. An important person to thank is Dr. Martina Wahnschaffe. Half of the chapters in this thesis are your fault, thank you for all the patience you had in teaching me the business of microwave simulations. I lost count of the beers I owe you a long time ago. I definitely need to thank Dr. Matthias Kohnen, although the time we spent together was short you taught me the fundamentals on how to trap ions and operate the lab. For this I will always be grateful to you. I further wish to thank Jonathan Morgner, thanks for all the help you have given me in the lab. I wish you all

the best in your future Penning trap endeavors. I would also like to thank Nicolas Pulido, one day all of this is going to be yours and you will push it to new heights. Another special thanks goes to Marius Schulte, thanks for all the help you have given me over the years. Thanks for putting up with me even when after two beers I still wanted to check some simulations for pulse shapes. Last, but not least, I need to thank Dr. Anna-Greta Conrad for all the help she has given me. I still owe you a coffee and a chair. A special thanks goes to Dr. Steven king, not the author, and to Dr. Fabian Wolf, for all the interesting discussions we ever had about experiments.
Thanks to all my friends who supported me nagging about my work over the years, especially Anna, Giulia, Silvia and Ugo. I would like to thank my parents and my brother for all the support they have ever given me that has let me pursue the study of physics. Grazie di cuore.
And finally, I need to thank my wife, Elisa. Thank you for your support over the years, for being there when I needed you. Thank you for being the most productive editor of this thesis.

List of publications

- G. Zarantonello, H. Hahn, J. Morgner, M. Schulte, A. Bautista-Salvador, R. F. Werner, K. Hammerer, and C. Ospelkaus. Robust and resource-efficient microwave near-field entangling $^{9}Be^{+}$ gate. *Physical Review Letters*, 123(26):260503, December 2019.

- H. Hahn, G. Zarantonello, M. Schulte, A. Bautista-Salvador, K. Hammerer, and C. Ospelkaus. Integrated $^{9}Be^{+}$ multi-qubit gate device for the ion-trap quantum computer. *Nature Physics Journal Quantum Information*, 5(1):70, August 2019.

- H. Hahn*, G. Zarantonello*, A. Bautista-Salvador, M. Wahnschaffe, M. Kohnen, J. Schoebel, P. O. Schmidt, and C. Ospelkaus. Multilayer ion trap with 3-dimensional microwave circuitry for scalable quantum logic applications. *Applied Physics B*, 125(8):154, July 2019.
  * these authors contributed equally

- A.-G. Paschke, G. Zarantonello, H. Hahn, T. Lang, M. Marangoni, C. Manzoni, G. Cerullo, and C. Ospelkaus. Versatile control of $^{9}Be^{+}$ ions using a spectrally tailored UV frequency comb. *Physical Review Letters*, 122(12):123606, March 2019.

- A. Bautista-Salvador, G. Zarantonello, H. Hahn, A. Preciado-Grijalva, J. Morgner, M. Wahnschaffe, and C. Ospelkaus. Multilayer ion trap technology for scalable quantum computing and quantum simulation. *New Journal of Physics*, 21(4):043011, April 2019.

- M. Wahnschaffe, H. Hahn, G. Zarantonello, T. Dubielzig, S. Grondkowski, A. Bautista-Salvador, M. Kohnen, and C. Ospelkaus. Single-ion microwave near-field quantum sensor. *Applied Physics Letters*, 110(3):034103, January 2017.

Giorgio Zarantonello

Schlägerstr. 6
30171 Hannover
Born April 6th, 1989

Research

07/2015 - 07/2020	**Doctoral Studies** Physikalisch-Technische Bundesanstalt & Leibniz Universität Hannover *PhD thesis in the group of Prof. Dr. C. Ospelkaus*

University

10/2012 - 12/2014	**Master of Science (Physics)** Università degli studi di Padova *Master thesis in the group of Prof. P. Villoresi*
10/2008 - 10/2012	**Bachelor of Science (Physics)** Università degli studi di Padova *Bachelor thesis with Prof. F. Ancilotto*